An exploration of methods for performing resting state fMRI in the human fetus

Ferrazzi, Giulio

Awarding institution:
King's College London

King's College London

Doctoral Thesis

An exploration of methods for performing resting state fMRI in the human fetus

Author:

Giulio Ferrazzi

Supervisor:

Prof. Joseph V. Hajnal

Centre for the Developing Brain

Department of Imaging Sciences & Biomedical Engineering

2016

Declaration of Authorship

I, Giulio Ferrazzi, declare that this thesis titled 'An exploration of methods for performing resting state fMRI in the human fetus' and the work presented in it are my own work, expect when clearly stated.

Signed:

Date:

KING'S COLLEGE LONDON

Abstract

School of Medicine

Department of Imaging Sciences & Biomedical Engineering

Doctor of Philosophy

An exploration of methods for performing resting state fMRI in the human fetus

by Giulio Ferrazzi

Functional Magnetic Resonance Imaging, or fMRI, is today a well established tool used to assess both resting state connectivity and task activation in neuroscience. It has also been used for the study of brain development in neonates and there are a small number of pilot studies that seek to use fMRI *in utero*. However, there are formidable challenges in this application as the fetus lies within the mother and is moved by her respiration as well as performing its own sporadic and unpredictable motion. Thus motion is a core issue for any fetal fMRI study.

The first chapter of the thesis discusses a pipeline that was developed to analyse fetal fMRI data acquired with standard sequences. The approach addresses motion correction as a primary requirement, both to stabilise anatomical content for each voxel in a fMRI time series, but also to correct the data from other sources of image artefacts that can be modulated by movement, such as bias field, spin history and distortions. From the results of this study, it emerges that functional MRI is feasible in the developing fetus.

The magnetic properties of fetal and infant brain tissue are very different from adults, leading to a longer T_2^* relaxation time. This would suggest the use of longer echo times to optimise the BOLD effect, with the downside of decreasing imaging speed. Therefore, the second chapter explores the use of an echo shifted EPI (es-EPI) sequence that achieves an improved signal sensitivity while maintaining efficient sampling. The sequence has been extensively tested on phantom experiments and an improved signal detection is demonstrated on a series of fMRI experiments run on preterm and term-equivalent babies.

The long T_2^* and the lack of air-tissue boundaries between the fetal head and the womb encourages the use of EVI as favourable tool for fetal fMRI. A main benefit of an EVI sequence could indeed be imaging speed and robustness to motion. In a third chapter, EVI fetal imaging is explored and the methods developed allowed the fetal brain to be imaged in full 3D. Despite the challenges of making this work robustly, we speculate that further refinements of the sequence could constitute the ground work with which to perform fetal fMRI in the near future.

Acknowledgements

I owe a special thanks to my supervisor, Prof. Joseph V. Hajnal.
The enthusiasm that Jo has for his research is contagious, and this has helped me a lot. I am very grateful and thankful for the time he has dedicated to me and for setting an excellent example, both as a physicist and as a person.

I would like to thank all people from the Centre for the Developing Brain, King's College London. Among those, a special thanks goes to Dr. Rita Nunes, Dr. Maria Murgasova, Dr. Tomoki Arichi and Dr. Anthony Price; I am sincerely grateful for having had the opportunity to work with you. Thanks to my second and third supervisors: Dr. Shaihan Malik and Dr. Paul Aljabar. Another thanks to all my friends in the Department: Lucilio, Fran, Dafnis, Jana, Maryam, Andreia, Giuseppa, Rui, Pratchi, Arian and Anita.

A third special thanks goes to Cris, who followed my adventures in London and has always supported me.

Another thanks to Michael, Giovanni, Michela, Scrocca, Zilio, Pietro and Eloy.

I would finally like to thank my father, mother and sister, who are simply brilliant.

Contents

List of Figures

List of Tables

Chapter 1

Introduction

1.1 Overall aim

The developing brain undergoes tremendous changes in functional and structural connectivity during the pregnancy and the exact timings with which this happens is one of the major interests among many research groups. Early brain development encompasses the rapid growth and maturation of the cerebral cortex with neurons migrating towards the outer parts of the brain [Prayer et al., 2006]. It is therefore essential to any individual to experience normal brain development. This observation becomes even more critical when we note that, in the UK, 7-8% of the babies are born prematurely, and these individuals have an increased chance of developing pathological conditions over luckier ones that could experience a normal gestation [Goldenberg et al., 2008].

A second important observation is that the recent breakthroughs in medicine have been always accompanied by equivalent breakthroughs in technology. Therefore, today, we have a disposal a vast choice of imaging modalities with which we can monitor the development of fetuses. Among these imaging techniques, Magnetic Resonance Imaging (MRI) shines, since it has become increasingly feasible

providing images with great levels of contrast and outstanding resolutions. Furthermore, the flexibility offered by MRI renders possible the acquisition of images whose contrast have a clinical meaning, and its usage is therefore very valuable.

Functional MRI, or fMRI, is an MR imaging modality where the acquired signal is an indirect measure of neuronal activity [Ogawa et al., 1990]. During the last two decades, fMRI has been used worldwide to map neuronal activity in an enormous variety of species and populations. Other work has also proven the existence of functional maturation processes happening in the developing human brain during the third trimester of gestation [Doria et al., 2010, Smyser et al., 2010].

It is therefore of extreme interest to map neuronal activity directly *in utero* and initial studies are starting to suggest that this is feasible [Fulford et al., 2003, Hykin et al., 1999, Jakab et al., 2014, Jardri et al., 2008, Moore et al., 2001, Schöpf et al., 2012, Thomason et al., 2013]. However, the maternal tissue is a non-conventional environment to perform MR acquisitions since the magnetic properties of the womb are very much different from standard brain imaging. Furthermore, the impossibility of dealing with a compliant patient, the fetus, has so far limited the usage of fMRI to the minimum.

This thesis is a pilot that attempts to model and to process fetal fMRI data. It is a technical thesis and, as such, treats and deals with technical problems. Any extrapolation of the results to a larger scale needs therefore careful verification. Nevertheless, the thesis successfully addresses different physical aspects and problems encountered when dealing with fetal fMRI data.

1.2 Thesis outline

- **Chapter** 1: In this chapter, a brief introduction to the physics of MRI is given. Its scope is however restricted to those elements that are relevant to

the thesis, and therefore many aspects are left out. There are however numerous existing textbooks providing such information, particularly Buxton [2009], Haacke et al. [1999], Jezzard et al. [2001], which have been partly used to write this.

The chapter begins by describing the process of signal formation and gradient encoding. Subsequently, the interest shifts towards functional MRI and a detailed description of such images is given. The primary source of functional contrast, the blood oxygenated level dependent (BOLD) signal is explained. The attention then moves towards the field of fetal MRI, on the challenges that it poses and on the state of the art techniques that allow the acquisition of such great images. Fetal motion, which is a major cause of artefacts that can lead to data misinterpretation, is also discussed.

- **Chapter 2**: This chapter discusses the development of a coherent framework to perform resting state fMRI studies in the fetus. The test data for this study comes from 8 healthy fetuses that were scanned on a 1.5T Philips Achieva scanner. The aim was to diminish the presence of various artefacts such as motion, bias field and spin history effects. The study continues with the processing of a larger dataset acquired on a 3T Achieva scanner. It introduces another step in the processing pipeline that deals with geometric distortions of fetal fMRI data. We finally show how resting state connectivity remains similar across the two populations.

- **Chapter 3**: This chapter describes an echo shifted Echo Planar Imaging (es-EPI) sequence applied to neonatal fMRI. es-EPI is a modification of a standard 2D single shot EPI sequence (1.4.1) that allows greater sensitivity to the BOLD effect in neonates and fetuses. This is done without sacrificing imaging speed. The sequence has been extensively validated on phantoms and adult subjects and a greater BOLD to noise contrast measured on a series of task-based fMRI experiments that were run on premature and term born infants.

- **Chapter 4**: This chapter represents the first attempt to perform an Echo Volumar Imaging (EVI) experiment in the fetus. EVI is a extension of a standard EPI sequence that allows the encoding of 3D volumes following single radio frequency (RF) excitations. The sequence can achieve a very high sampling frequency and therefore a sensible reduction of any motion-related artefact. The drawbacks are the extreme hardware demand imposed on the gradients, the technical difficulties encountered to accomplish the experiment, and the very loud acoustic noise. Here, an EVI sequence that mitigates these difficulties has been developed and initial tests show that it can be used to sample the fetal brain at a very high speed.

- **Chapter 5**: Conclusions and future work.

Note:

The work presented in chapters 3 and 4 has been carried out in partnership to Dr. Rita Nunes. Rita took the lead in matters related to the implementation of sequence modifications in the Pulse Programming Environment, particularly in the early phases of the work, and I took the lead in experimental design and in data analysis.

1.3 MRI

The field of Magnetic Resonance Imaging began during the late forties, where scientists discovered that hydrogen nuclei start to rotate at a precise frequency when immersed in an external magnetic field. Since then, the technological advances of the field have grown exponentially; MRI is today an indispensable tool for diagnosing diseases in the human body, and yet not as invasive as other imaging techniques such as X-rays, Computer Tomography (CT) and Positron Emission Tomography (PET). MRI can reveal anatomical details down to the scale of millimeters, and its versatility allows the acquisitions of images whose contrast depends exclusively upon the way the scanner is driven.

1.3.1 The NMR signal

Consider a sample of water immersed in an external magnetic field, with a coil of wires (such as a solenoid) placed so that its axis is perpendicular to the imposed magnetic field. We will refer to this external magnetic field as $\mathbf{B}_0$ [1].

The Nuclear Magnetic Resonance (NMR) experiment is formed by a *transmitting* and a *receiving* phase. In the above scenario, the coil acts as the transmitter as well as the receiver, and the acquired signal comes entirely from the sample of water. During the transmitting phase, a small oscillating perturbation is achieved by playing a small oscillating current in the coil [2]. During the receiving phase, the coil acts as a receiver by sensing small magnetic variations in the water sample as a response to the applied perturbation. We can consider every MRI experiment as an extension of this basic experiment. The way the signal is localized to create an image will be discussed in the next sections.

[1] In standard clinical MRI scanners, $\mathbf{B}_0$ usually ranges from 1.5 to 3 Tesla (T), but research systems now extend to 7T or higher.

[2] In MRI, the frequency of such perturbation is in the radiofrequency range and its duration is of a few milliseconds. This is usually regarded as a *pulse*.

The radio frequency pulse is a magnetic perturbation whose frequency is set to a specific value which is a property of water. At 1.5 Tesla, this is 64 MHz and it is called the *Larmor* frequency. The application of a current not well tuned to this value would result in an experiment with no measurable signal. With such excitation, however, after the pulse is finished, there will be a small and transient detectable current in the coil. This current represents the measured NMR signal [3] and a qualitative representation is given in Figure 1.1; the NMR signal (black line) occurs at the Larmor frequency, and its transient behaviour manifests as an exponential decay (gray-dashed envelope).

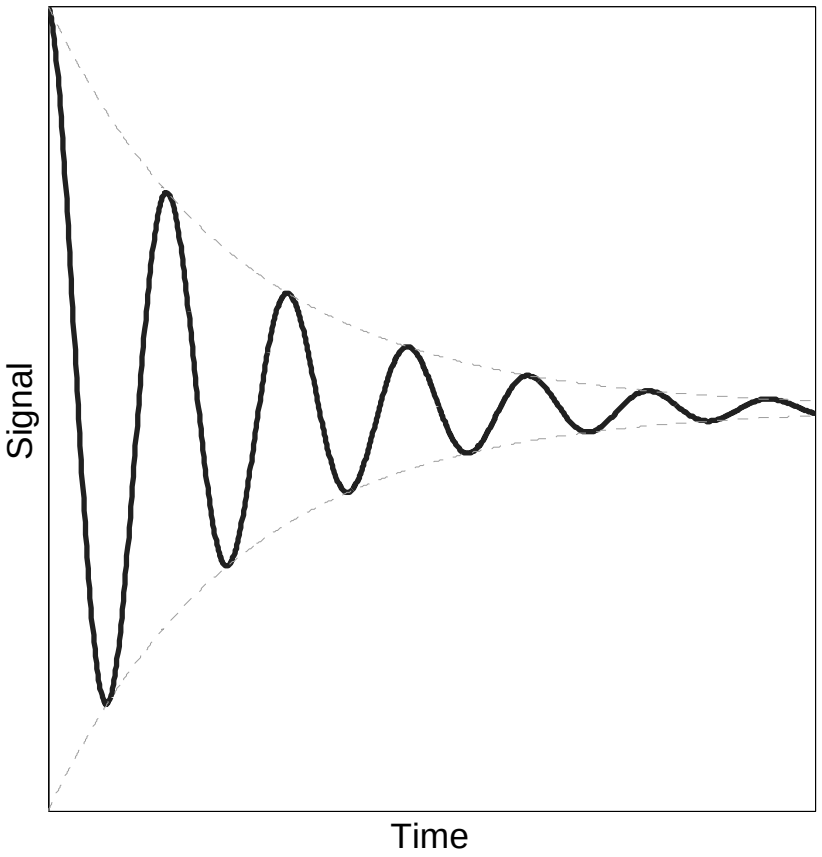

FIGURE 1.1: NMR signal, qualitative representation.

[3]The NMR signal can also be referred to as *free induction decay* (FID).

This peculiar behaviour is due to the magnetic properties of the hydrogen-nuclei: at the Larmor frequency, the hydrogen nuclei is able to absorb energy during the transmitting phase and to release it during the receiving phase as electromagnetic energy. The phenomenon is transient, and tends to return to the original configuration which is at the lowest energy state.

There is straightforward relationship between the precession frequency and the strength of the main magnetic field which is:

$$\omega = \gamma B_0 \tag{1.1}$$

where ω is the angular velocity of the spins and γ a constant quantity referred to as gyromagnetic ratio. The gyromagnetic ratio for hydrogen is 267.54 $\frac{rad}{s \cdot uT}$ (or equivalently 42.58 $\frac{MHz}{T}$ if ω is expressed in MHz). Note also that $B_0 = |\mathbf{B}_0|$.

According to this relation, the precession frequency is directly proportional to the strength of the field in which the spins are immersed. As previously described, this value is of 64 MHz for water at 1.5T, and will be 128 and 268.66 MHz at 3 and 7T.

The receiving coil registers the overall contribution of all spins coming from the sample of water. However, there are two distinct spin populations; the first aligns along the direction of the magnetic field $\mathbf{B}_0$, and the second which is opposite to it. At equilibrium, the ratio between these two populations is very close to one, with a slightly larger fraction of spins aligned along $\mathbf{B}_0$. This results in a weak magnetization (defined as $\mathbf{M}_0$) at equilibrium, aligned along the direction of $\mathbf{B}_0$ which is the source of the NMR signal. The phenomenon has been qualitatively explained; however, the ratio between the populations in the two states follows the Boltzmann distribution. In general, we can increase the polarization of the the spin system by increasing the field strength.

Interaction between the RF pulse and the main magnetic field

The behaviour of the magnetization vector as a function of the excitation pulse is completely predetermined by a set of linear differential equations which are called the Bloch equations [Bloch, 1946, Haacke et al., 1999]. However, in this thesis, the process of excitation is presented in a more intuitive way.

The signal formation relies on the interactions which are established between the magnetization and an RF pulse. During the transmitting phase of the NMR experiment, the radiofrequency pulse is producing a magnetic field, $\mathbf{B}_1$, perpendicular to $\mathbf{B}_0$. As mentioned, when the radiofrequency pulse is not tuned to the Larmor frequency, not very much happens. However, when the constraint is met, the phenomenon of *resonance* occurs.

Consider an ensemble of spins that occupy a small volume in which conditions can be considered to be uniform so that there is an identifiable single Larmor precession frequency. When such conditions are met, the interactions with the $\mathbf{B}_1$ field are as follows; the $\mathbf{B}_1$ imposes a torque on the spin system causing the magnetisation to rotate away from alignment with $\mathbf{B}_0$. If $\mathbf{B}_1$ is applied for a suitable amount time, $\mathbf{M}_0$ effectively tips away from $\mathbf{B}_0$ tracing out a spiral trajectory. Figure 1.2 sketches this process.

The angle formed between the magnetization vector and the direction of $\mathbf{B}_0$ is called the *flip angle* α and it depends on the strength and on the time for which $\mathbf{B}_1$ is applied. The flip angle is an important acquisition parameter in all MRI experiments, because it has a direct impact on the strength of the signal and to its ratio over the noise (or Signal to Noise Ratio, SNR).

Relaxation

When the RF pulse is turned off, the magnetization tends to return to the initial configuration which is at its lowest energy state. The processes involved are

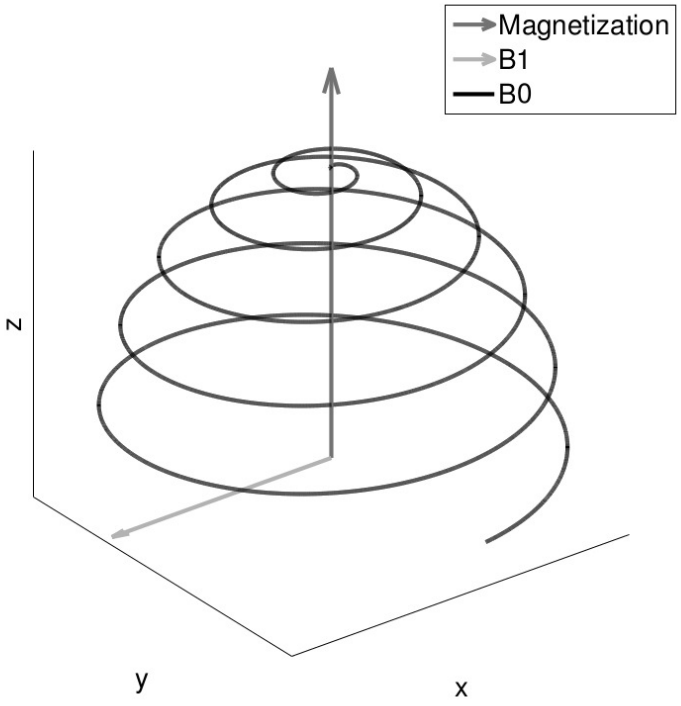

FIGURE 1.2: The magnetisation vector spirals down into the transverse plane during the application of an RF pulse whose magnetic field is $\mathbf{B}_1$.

referred to as relaxation effects.

There are two main sources of signal relaxation; the first one, called transverse relaxation, which is the signal decaying in the transverse plane. The other one, called longitudinal magnetization, is the realignment of the magnetization along the direction of $\mathbf{B}_0$.

The transverse relaxation happens because not all spins precess exactly at the Larmor frequency. This is caused by dipolar spin-spin interactions that destroy the coherence of the NMR response and cause the signal to decay. The transverse magnetization (projection of the magnetization vector onto the transverse plane whose value at time 0 is equal to: $M_{xy}(0) = M_0 \cdot sin(\alpha)$, where $M_0 = |\mathbf{M}_0|$) will therefore start to decay right after the pulse is turned off. The phenomenon completely destroys all transverse magnetisation and its dynamic behaviour is an exponential decay:

$$M_{xy}(t) = M_{xy}(0) \cdot e^{-\frac{t}{T_2}} \tag{1.2}$$

In this equation, T_2 is the transverse relaxation time. In liquid water with few impurities, the value for T_2 is approximately 3000-4000 ms, whereas, in human adult brain tissue, theses values are approximately 70 ms for white matter and 100 ms for gray matter at 3T [Stanisz et al., 2005]. Different relaxation values in different tissues are a primary source of contrast in MRI images.

The other type of relaxation in MRI is the longitudinal relaxation time and it represents the process by which the magnetization vector realigns along the z axis. This process also displays an exponential behaviour, and more precisely:

$$M_z(t) = M_0 - [M_0 - M_z(0)] \cdot e^{-\frac{t}{T_1}} \tag{1.3}$$

where $M_z(0) = M_0 \cdot cos(\alpha)$ is the longitudinal magnetization right after the RF pulse is applied. T_1 a new constant, which is the longitudinal relaxation time. Different tissue types will have different values for T_1. At 3T, for example, T_1 is approximately 1100 ms and 1800 ms in the adult white and gray matter [Stanisz et al., 2005].

Finally, images sensitive to either T_1 or T_2 are referred to as T_1 or T_2 *weighted*.

Even when the acquisition is insensitive to both T_1 and T_2, there is some contrast between different tissues. Such images are said to be *proton density weighted* and they form because of different 'concentrations' of the magnetization $\mathbf{M}_0$ across the body. Such images are however not treated in this thesis and therefore only mentioned here.

1.3.2 Image formation

One remarkable feature of MRI is that it is able to map the state of the transverse magnetization to the scale of millimeters. In the previous sections, however, we have only presented the behaviour of the magnetization vector as a whole, and stated that the receiving coil measures the contribution of the entire sample of water at once. As with the simple water sample case, when a patient is placed into an MRI scanner, the coil, which for brain imaging is typically designed to be close fitting around the patient's head, will measure the overall contribution coming from all spins excited by the RF pulse. The question which follows naturally is therefore: how is MRI able to localize the signal and to create images with such great level of details?

The solution is the exploitation of equation 1.1. The spatial dependency of the signal is in fact achieved via the application of *magnetic field gradients*. In any MRI scanner, there are indeed three additional coils capable of generating fields which increase or decrease linearly as a function of position. When these gradient fields are applied, ensembles of spins at different spatial locations in the direction of the gradient precess at different frequencies creating a localisation signature.

The gradients can act separately and at a relatively very fast rate. We will call them G_x, G_y and G_z, depending on whether they are applied along the x, y and z directions. A remarkable feature of these gradients is that they generate fields which are tiny in comparison to $\mathbf{B}_0$.

In slice based MRI, the signal localization is done in three ways. For ease of explanation, we adopt a conventional coordinate system with z axis parallel with the $\mathbf{B}_0$ field, and consider a pure transverse slice that contains the x and y axes. In such condition, there is a *slice selection* gradient (applied along z), a *phase encoding* gradient (along y) and a *frequency encoding* gradient (along x). These three processes are described in the next two sections.

Slice selection

The first step is to limit the excitation to a slice of width $\triangle z$. This is achieved by turning on a slice selection gradient G_z together with the RF pulse. The RF pulse has a narrow frequency bandwidth so that only spins with Larmor frequency within a precise range will experience resonance. As spins at different z locations are precessing at different frequencies, only spins within the interval $\triangle z$ will tip over and generate MRI signal. The parameters with which the operator can tailor the excited region (or resolution in the slice direction) are the strength of G_z and the bandwidth of the excitation pulse.

Each excited slice immediately starts to experience relaxation processes, and the way the signal is encoded in the xy plane will be discussed in the next session. Once the encoding is completed, a different slice can be acquired by simply tuning the center frequency of the excitation pulse to another value.

Frequency and phase encoding

When a certain slice is excited, the G_x and G_y are turned on. The function of these gradients is remarkably similar and that's the reason why they are treated together here.

Let's assume that the relaxation process is not affecting the excited slice, (i.e $T_1 = T_2 \rightarrow \infty$). As such, the longitudinal magnetization when converted into transverse (let's also assume that the flip angle α is 90°), will precess indefinitely around the xy plane at the Larmor frequency. Since all spins are precessing at the same frequency, there is no phase accumulation across spins at different locations. A brief gradient pulse G_x (or G_y) is now applied along the x axis (or y axis). Because of the Larmor equation, the spins will start to precess at different frequencies along that direction. Furthermore, when the same gradient is switched off, all spins will return to precess at the same Larmor frequency regardless of position. However, there will be different phase for spins at different

positions, because they were precessing at different frequencies when the gradient was on. This can be described mathematically and, for a spin at position x when a time dependent gradient is applied, the phase is equal to:

$$\phi(x,t) = -2\pi\gamma \int_0^t G_x(t')dt' \cdot x \tag{1.4}$$

This equation represents the phase accumulation of a spin at position x relative to a spin at position $x = 0$, which of course is precessing at a constant Larmor frequency and, at time t, has a phase of $\phi_0 = -2\pi\gamma B_0 t$. Here, the minus sign follows the convention adopted in [Haacke et al., 1999] and γ transforms from magnetic field units to frequencies.

Equation 1.4 is fundamental to understand MRI. The application of gradients along a prescribed direction determines a phase which depends on the time and strength for which the gradients are applied. We discuss this phenomenon in the next subsection, by relating the acquired data (or *k-space* data) to the Fourier transform of the image.

k-space representation

Let's analyse the series of events that comprise a standard MR experiment. A representation of this is given in Figure 1.3, that represents a gradient echo sequence (top Figure). In this Figure, time is increasing along the horizontal axis. Furthermore, slice, phase and read directions correspond to the second, third and fourth lines. The pulse and the acquisition module (black patch) are represented in the first and fifth lines.

Before running the sequence, the imaging target is placed inside the scanner and a small magnetization $\mathbf{M}_0$ is created at any location in the body. Following this, an RF pulse together with a slice excitation gradient G_z are applied. The effect is

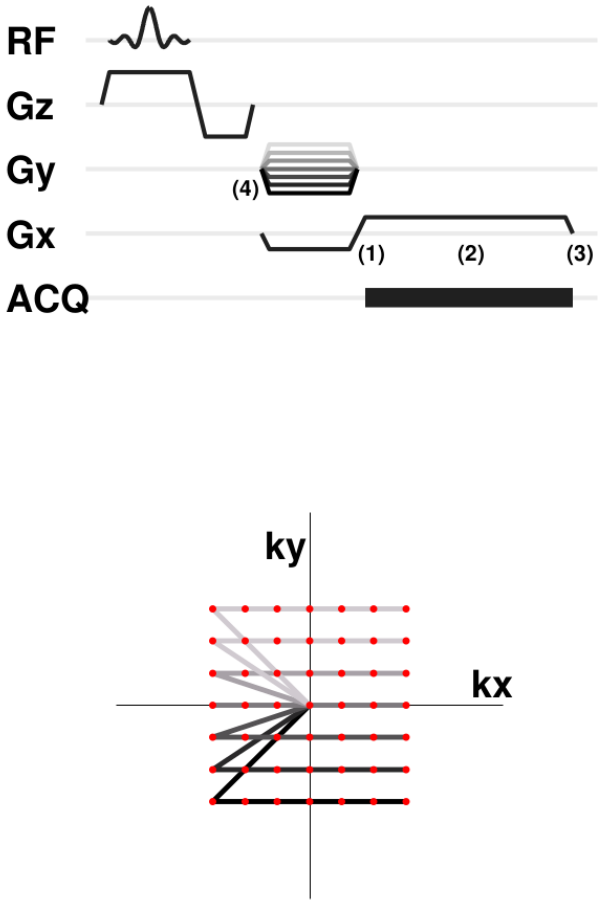

FIGURE 1.3: Top: Gradient echo sequence. The first line is the radio frequency (RF) pulse. Second, third and fourth lines are the slice, phase and read selection gradients. The acquisition module is represented in the fifth line (black patch). Bottom: Corresponding k-space acquisition trajectory.

to excite a single slab of tissue of thickness $\triangle z$. After excitation, the longitudinal and transverse magnetizations start the process of relaxation.

The more interesting part is what happens when the x and y gradients are switched on. Let's firstly only concentrate on the read gradient G_x which, in Figure 1.3, is, at first, negative. At the end of its application (Figure 1.3, position 1), the phase along that direction will increase linearly with position and

the signal in the coil will be 'weak'. Following this, the polarity of G_x is reversed and the effect is that the phase will start to be compensated for. At a particular moment, which in MRI is called *echo time* (Figure 1.3, position 2), all spins will recover the phase and the observed signal (or *echo*) in the coil is maximum. In MRI, the time in between the RF and the echo formation is called T_E. After the echo, the spins will dephase again as the result of the application of the remaining G_x gradient (Figure 1.3, position 3).

Let's now consider the y axis; if no y gradients are applied, the acquired signal is the projection of all spins along the y axis onto the x axis. This is because there is no accrued phase along y, and therefore all spins contribute constructively. y gradients blips are however applied each time the first G_x gradient is turned on (Figure 1.3, position 4). This confers on the signal a 'stamped' phase that depends on the y position as well. The sequence is repeated multiple times with different strengths for the y blips so that multiple distinct lines of data are acquired while the G_x gradient is on. By doing this, it is possible to fill a 2D matrix, where each point corresponds to a different 'combination of phases' along the x and y directions. Figure 1.3 (bottom) depicts this process.

It turns out that this 2D matrix is the 2D Fourier transform of the image. In MRI, the Fourier space is called *k-space* and the terminology was firstly introduced in Likes [1981]. The representation is a straightforward way of picturing the MRI imaging process and it gives a very intuitive and useful tool that can be used in much more complex experiments.

By collecting data the way described above, the acquired signal s acquired at absolute time t is given by [Haacke et al., 1999]:

$$s(t) = \iint \mathbf{I}(x,y) e^{i(\phi(x,t)+\phi(y,t))} dxdy \tag{1.5}$$

where **I** is the image to be determined. According to this equation, each sampled data point is an integral over the full slice of the object and it is weighted by a spatially and temporally dependent phase.

If we define with [Haacke et al., 1999]:

$$\begin{cases} k_x(t) = \gamma \int_0^t G_x(t')dt' \\ k_y(t) = \gamma \int_0^t G_y(t')dt' \end{cases} \tag{1.6}$$

we can simply rewrite equation 1.5 as:

$$s(t) = \iint \mathbf{I}(x,y)e^{-2\pi i(k_x(t)x+k_y(t)y)}dxdy \tag{1.7}$$

Finally, by rearranging the signal s into a two dimensional matrix **S** (in MR regarded as a *k-space* data matrix), and by dropping the explicit dependency of k_x and k_y on the time coordinate t (i.e. $k_x(t) = k_x$ and $k_y(t) = k_y$)), we get:

$$\mathbf{S}(k_x,k_y) = \iint \mathbf{I}(x,y)e^{-2\pi i(k_x x+k_y y)}dxdy \tag{1.8}$$

which is the 2D Fourier transform of the image **I**. Furthermore, the quantities k_x and k_y represent and assume the dimensions of spatial frequencies.

In MRI, there is the need to sample the entire spectral content of the k-space in order to get an image. Signal at low spatial frequencies corresponds to large structures in the data and, conversely, high spatial frequencies correspond to fine details and border edges. Furthermore, and in accordance with the Fourier theory, the image in plane resolution $\triangle x$ and $\triangle y$ is set by the extent of the k-space (or field of view in the k-space domain), and, conversely, the field of view in the image domain depends on how dense contiguous k-space samples are (or resolution in the k-space domain).

The vast majority of MRI sequences utilize Cartesian sampling. However, by combining vectorially $G_x(t)$ and $G_y(t)$ into a vector $\mathbf{G}(t) = [G_x(t), G_y(t)]$, we can rewrite equation 1.6 as [4]:

$$\mathbf{k}(t) = \gamma \int_0^t \mathbf{G}(t')dt' \tag{1.9}$$

where $\mathbf{k}(t)$ corresponds to $[k_x(t), k_y(t)]$. This parametric representation is important because it shows that it is actually possible to define arbitrary acquisition trajectories [Haacke et al., 1999].

1.3.3 Image contrast

To understand what the image $\mathbf{I}$ represents, let's allow the magnetization to relax after the application of the RF pulse. As mentioned in the previous sections, an image will be either T_1 or T_2 weighted, or a combination of these and also possibly other weighting factors.

In addition to spatial encoding gradients, extra RF pulses can be used to manipulate the magnetisation and, in particular, the use of refocusing pulses after excitation pulses creates the so called *spin echo* effect [Hahn, 1950]. The behaviour of spin echoes and their impact on spatial encoding is not required for this work, so it won't be treated. However, spin echoes can produce T_2 contrast.

In determining the level of T_1 contrast in an MR image, there is parameter which is called the *repetition time* (T_R) that (usually) represents the time that intervenes between RF excitation pulses that operate on the same region of space. Besides having a clear role in determining the sampling rate in any MRI experiment and therefore the speed with which an image is acquired, T_R has very important repercussions on the signal itself. As a rule of thumb, images acquired with long

[4] Note that we are still constraining the problem to be 2-dimensional. However, a natural extension is 3D sampling.

T_R and T_E, particularly if a spin echo acquisition is used, will be T_2 weighted, whereas a short T_E and T_R will produce a T_1 weighted image. More specifically, a long T_E allows the transverse magnetization to dephase and T_2 contrast forms because of different tissue types relaxing at different rates. Also, a long T_R allows the longitudinal magnetization to recover more completely before the application of the subsequent pulse and therefore the transverse magnetization produced by the next pulse is not affected by modulation due to T_1 effects. Opposite considerations can be applied when using a short T_E and T_R. Finally, an image is proton density weighted if it is acquired with a long T_R and a short T_E.

There are other ways to achieve and promote these contrasts, for example via the application of preparation pulses prior to the process of spatial encoding. The most common way to do this is by using *inversion recovery* sequences. However, their description goes beyond the scope of this introduction and we refer the reader to other sources [Hajnal et al., 1992].

1.3.4 T_2^* contrast

Another important source of contrast has been deliberately left out from this introduction. This is called T_2^* contrast and it turns out to be a most important source of information in fMRI.

If a gradient echo readout is specified with a long echo time, we would expect the signal to be heavily T_2 weighted. However, if we do this, we would observe that the signal decays faster. The reason for this lies in the field inhomogeneities of the MRI system; in other words, the imperfections of the MRI scanner give rise to a new and different type of image. However, T_2^* is also tissue dependent.

Because the field is not homogeneous, ensembles of spins will precess at different frequencies. If we now consider the signal contribution coming from a voxel, it will tend to decay away after the application of the RF. In practice, there

is an additional dephasing of the magnetization introduced by magnetic field inhomogeneities, which is a separate decay $T_2^{'}$.

The relationship between T_2^*, T_2 and $T_2^{'}$ is given by:

$$\frac{1}{T_2^*} = \frac{1}{T_2} + \frac{1}{T_2^{'}} \tag{1.10}$$

and the transverse magnetization evolves according to:

$$M_{xy}(t) = M_{xy}(0) \cdot e^{-\frac{t}{T_2^*}} \tag{1.11}$$

1.4 Acquisition in fMRI

Before the advent of fMRI, the only available methods to measure functional activation across the brain were: electroencephalography (EEG), positron emission tomography and magneto-encephalograms (MEG). While EEG and MEG are non-invasive but characterized, in general, by high temporal resolution and low spatial resolution, PET is limited by the administration of radioactive substances to the patient. fMRI, on the other hand, is non invasive and characterized by a good spatial resolution and an intermediate temporal resolution, and therefore suitable for these type of studies [Van Den Heuvel and Pol, 2010].

1.4.1 EPI

Echo Planar Imaging (EPI) was first described by Mansfield [1984]. EPI is today very well established in the world of fMRI because of its sensitivity to the blood-oxygenated-level-dependent (BOLD) signal.

While the construction of an image in conventional MRI is built up from a series of k-space lines, EPI acquires all k-space in a 'single shot'. This is particularly

advantageous in fMRI, where people are interested in sampling a dynamic process. Figure 1.4 represents the simplest EPI pulse sequence (2D gradient echo EPI). Here, multiple lines of k-space are acquired, each with a different phase encode. After the radio frequency pulse, prephaser gradients along the phase and read directions are played, and the effect is to shift towards the edges of k-space. A read-sequence of alternating polarity gradient lobes interspersed by gradient blips are used to produce a zigzag path that allows the acquisition of an entire k-space plane following the shot. After Fourier transforming, the result is a T_2^* weighted image.

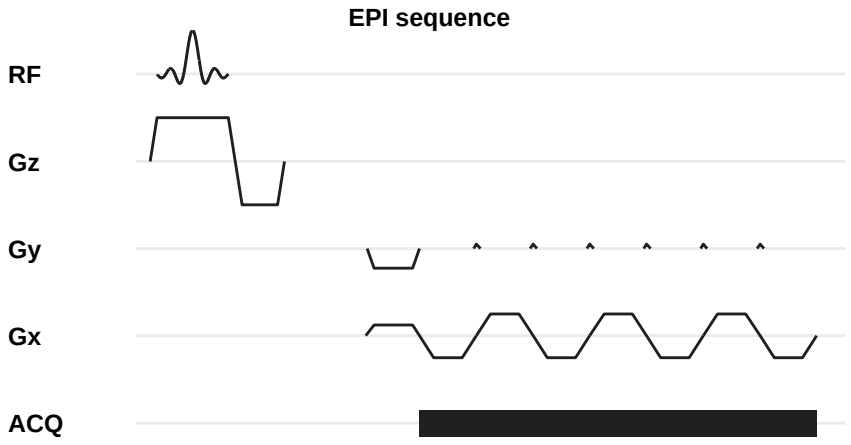

FIGURE 1.4: A gradient echo EPI sequence.

In fMRI, the echo time T_E represents the time in between the application of the RF and the collection of data encoded to the centre of k-space. This is a parameter that is decided prior to scanning and that determines the contrast in the final image, its SNR and also the sensitivity to the BOLD signal [5]. The echo time in standard fMRI experiments ranges from 20 to 60 ms and its value is usually chosen as a compromise between efficient temporal sampling and sensitivity to the BOLD effect.

[5]The BOLD signal is the primary source of information in functional magnetic resonance imaging and will be defined in the next sections.

Another very important parameter in fMRI experiments is T_R. In a very standard setup, depending on the resolution in the z direction and other factors such as age and sex of the patient being studied, a set of slices N_{slices} is required and these can take up to 50 to 100 ms each. Also, as in fMRI the functional behaviour of the brain is mapped over time, several volumes are acquired. The sampling rate is set by T_R which represents the time it takes for acquiring a single volume. The minimum achievable repetition time depends from many other parameters - and among the most important there are: echo time T_E, in plane resolution and the number of acquired slices N_{slices}. In a standard fMRI experiment, T_R ranges in between 1500 to 3000 ms. In general, shortening the T_R is a very active area of research and several approaches have been proposed [Larkman et al., 2001, Pruessmann et al., 1999].

In plane and through plane resolutions are other very important parameters that determine the minimum detectable structure size and the precision with which functional information can be mapped. The resolution is also very much related to the SNR. Usually, the bigger the voxel size, the higher the SNR will be.

In a standard fMRI experiment, these parameters range from 2 to 3 mm for in plane resolution, and from 3.5 to 5 mm for the through plane direction.

Figure 1.5 shows transverse, sagittal and coronal views of fMRI data from a healthy adult. The image has been acquired on a 3T Achieva scanner using a 32 channel head coil. The echo and repetition times T_E and T_R were 50 and 2550 ms, with the image acquired at a resolution of $2.5 \cdot 2.5 \cdot 3.5$ mm^3.

This data provides some clues about the nature of fMRI images; the contrast that can be achieved with fMRI is usually not as enhanced as in other types of MR imaging modalities. White and gray matter are less distinguishable than in T_1 and T_2 weighted images. However, some contrast remains and there are structures clearly visible - for example, in Figure 1.5, the ventricles appear as bright. This is because the long T_2^* in these regions.

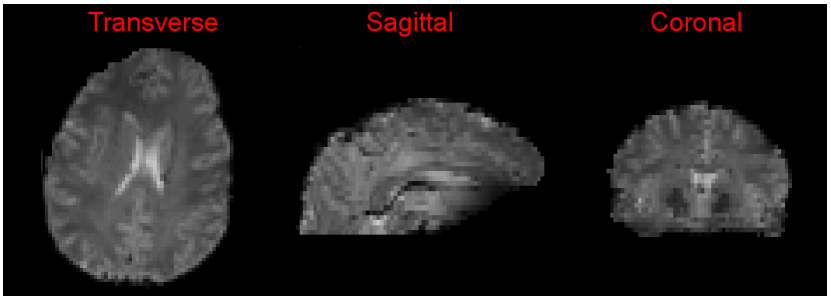

FIGURE 1.5: Transverse, sagittal and coronal views of a standard fMRI dataset acquired on a healthy adult volunteer. The echo and repetition times T_E and T_R are 50 and 2550 ms. Resolution is $2.5 \cdot 2.5 \cdot 3.5\ mm^3$.

1.4.2 Artefacts in EPI

SNR is not the main issue in fMRI studies. EPI, in fact, has the full magnetization available before sampling.

There are however numerous sources of artefact in MR, and the most common will be described in the following sections. Furthermore, these artefacts are particularly severe in EPI, where the bandwidth along the second phase encoding direction is low.

1.4.2.1 Partial Volume Effects

Partial Volume Effects (PVE) occur when the acquired voxel contains more than one tissue type and the signal strength will depend upon the proportion of its elements. Partial volume effects are therefore strongly present at the boundaries between different tissues and they can lower the contrast.

1.4.2.2 Chemical Shift between water and fat

This artefact appears because water and fat resonate at different frequencies (3.5 ppm, parts per million apart) when immersed in a magnetic field [Mao et al.,

1993]. Because of the shift in resonance frequency ($\gamma\Delta B_0^{fat}$), we can rearrange equation 1.7 in [Haacke et al., 1999]:

$$s^{fat}(k_x(t), k_y(t), t) = \iint \mathbf{M}_{xy}^{fat}(x, y) e^{-2\pi i(k_x(t)x + k_y(t)y)} e^{-2\pi i\gamma\Delta B_0^{fat} t} dxdy \quad (1.12)$$

Here, the term $\mathbf{I}$ has been substituted with the transverse magnetization $\mathbf{M}_{xy}^{fat}$ generated by the fat. Therefore, s^{fat} represents the fat signal only. Note also that, in this equation, we maintain the explicit dependency of the spatial frequencies k_x and k_y on the time coordinate t. Equation 1.12 has embedded the extra phase $e^{-2\pi i\gamma\Delta B_0^{fat} t}$. This term does not dependent on the integration variables dx and dy, so it can be brought outside the integral leading to:

$$s^{fat}(k_x(t), k_y(t), t) = e^{-2\pi i\gamma\Delta B_0^{fat} t} \cdot \iint \mathbf{M}_{xy}^{fat}(x, y) e^{-2\pi i(k_x(t)x + k_y(t)y)} dxdy = e^{-2\pi i\gamma\Delta B_0^{fat} t} \cdot \mathbf{S}^{fat}(k_x(t), k_y(t)) \quad (1.13)$$

This new equation says that the fat signal is the Fourier transform of the transverse magnetization generated by fat ($\mathbf{S}^{fat}$) multiplied by a phase ramp which applies a different and complex weighting to each k-space data point ($e^{-2\pi i\gamma\Delta B_0^{fat} t}$).

To understand how the fat artefact appears in EPI data, we note that the time step between successive samples acquired in the frequency encode direction is typically a few microseconds, whereas adjacent samples in the phase encoding direction have a much higher time separation that is typically 0.5 to 1 ms on average. Thus the phase modulation caused by the frequency shift of the fat signal is about 100 times larger in the phase encoding direction and so we can neglect the effect in the frequency encoding direction. Furthermore, in the theory of Fourier transforms, the presence of a phase ramp in Fourier space corresponds

to a *shift* in image space. Therefore, as a consequence of the extended time taken to complete the EPI readout along the phase encoding direction, the fat signal will be shifted by a certain amount and it will appear displaced from water.

Figure 1.6 shows an example of this: a preterm baby of 33 weeks was scanned on a 3T Achieva scanner using single shot EPI at an isotropic resolution of 2 mm using an echo time T_E of 25 ms. The Figure shows a transverse slice from that data and a rim of fat is misplaced, appearing almost in the centre of the field of view (red arrow). The phase encoding direction is, in this case, the anterior-posterior direction.

Fat artefacts can be reduced via the usage of fat saturation pulses. These are RF pulses well tuned on the fat resonance frequency aiming at its saturation prior to the readout. An example is Spectral Presaturation with Inversion Recovery (SPIR) [Halligan et al., 1998]. Here, an inversion pulse is designed to invert the magnetization coming from the fat signal. After excitation, the fat signal evolves back to equilibrium following T_1. As the magnetization passes through the null point, a conventional MRI sequence is run.

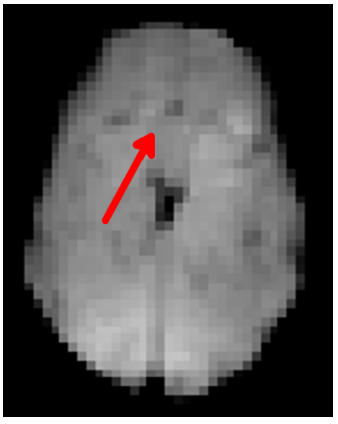

FIGURE 1.6: Fat artefact in the neonatal brain.

1.4.2.3 Ghosting

This is probably the most common artifact in EPI. It is due to the presence of eddy currents, generated on all the conductive surfaces of the scanner after the rapid switching of the time dependent gradients. These eddy currents, in turn, distort the local magnetic field inside the machine, leading to a wrong encoding of the data.

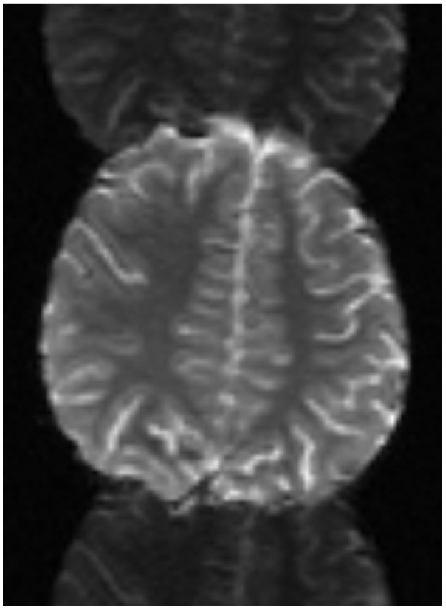

FIGURE 1.7: Classical ghost in EPI data appearing along the phase encoding direction (vertical).

The ghosting artefact (Figure 1.7) is due to the combination of eddy currents with the back and forth EPI acquisition trajectory. This can result in systematic differences in phase between adjacent lines of the raw data. Following Fourier transformation, part of the signal can appear shifted by half a field of view along the phase encoding direction. The intensity of this so called Nyquist ghost depends on the magnitude and phase differences between the adjacent lines.

Ghosting artefacts can be mitigated by using calibration data. This data is always acquired prior to acquiring the actual EPI image data and consists of k-space

samples with no phase encoding so that they can be used to identify and quantify systematic inconsistencies.

1.4.2.4 Bias Field inhomogeneities

This artefact affects all MR images in general and not only EPI. However, strong bias field inhomogeneities can substantially impact the analysis of fMRI data and that's the reason why a brief introduction is given.

Inhomogeneity of the receiver radio-frequency field ($\mathbf{B}_1^-$) effects the voxel intensities of the acquired MR data as a multiplicative shading artefact [Juntu et al., 2005]. This intensity non-uniformity varies smoothly across space. However, the modulation of the signal can be as high as 10 to 20 %.

Figure 2.10 (A) shows part of data that will be presented in chapter 2. However, it illustrates the phenomenon well. The Figure shows a slice in the transverse plane from a fetus of 34 weeks acquired with a standard fMRI protocol (described in details in the next chapter). Very high signal is visible in the proximity of the left temporal lobe (red arrow).

1.4.2.5 Saturation effects

Let's consider an fMRI experiment in which the applied flip angle is 90°. As such, the longitudinal magnetization is entirely converted into transverse when the first RF is applied. If T_R is longer than T_1 ($T_R > 5T_1$), the longitudinal magnetization has the necessary time to recover before the application of the subsequent RF pulse. However, a long T_R results in a slow sampling rate and this is undesirable in fMRI. Furthermore, T_1 increases at higher fields [Stanisz et al., 2005], and therefore it is a pretty common situation to have a repeat time T_R much shorter than T_1. When this happens, there is a strong modulation of the signal due to the lower available magnetization.

The solution to this problem may seem counter-intuitive at first sight but it involves the reduction of the flip angle α [Haacke et al., 1999]. By doing so, the longitudinal magnetization will recover 'sufficiently' prior to the application of the next pulses. For a fixed a T_R and T_1, the optimal flip angle has a precise name and it is called the *Ernst angle*. The Ernst angle has a closed formula and more precisely:

$$\alpha_e = \arccos(e^{-\frac{T_R}{T_1}}) \tag{1.14}$$

1.4.2.6 Steady State Magnetization and Spin History artefacts

Even when the Ernst angle is chosen, the magnetization will have a time varying behaviour in correspondence of the first volumes being acquired, and it will reach its *steady state value* only after a few repeat times. Common practise is therefore to discard the first few timepoints of any fMRI dataset.

To model this, let's imagine that only one slice is acquired so that the inter-slice time coincides with the inter-volume time and that the object is fully confined within the slice itself. Let's also assume that the slice excitation profile is a flat-top function with no dependency on the effective achieved flip angle along the through-slice direction. Let's denote with $M^j_{L,+}$ and $M^j_{T,+}$ the longitudinal and transverse magnetization components just *after* this single slice has been excited by the j^{th} pulse. Similarly, we denote with $M^j_{L,-}$ and $M^j_{T,-}$ the magnetization right *before* the same RF pulse is applied (T_2 and T_2^* decays are assumed to remove any significant coherence effects between successive excitations). Using this terminology we can write:

$$\begin{cases} M^j_{L,+} = M^j_{L,-} \cdot \cos(\alpha) \\ M^j_{T,+} = M^j_{L,-} \cdot \sin(\alpha) \end{cases} \tag{1.15}$$

where α is the nominal flip angle.

Between two consecutive excitations, say $(j-1)^{th}$ and j^{th}, the longitudinal magnetization $M_{L,+}^{j-1}$ recovers towards the magnetization at equilibrium ($\mathbf{M}_0$) with T_1 relaxation rate. Like in equation 1.3, the magnetization available right before the j^{th} pulse is [Haacke et al., 1999]:

$$M_{L,-}^{j} = [M_0 - (M_0 - M_{L,+}^{j-1}) \cdot e^{-\frac{T_R}{T_1}}] \tag{1.16}$$

If we combine 1.16 with 1.15 we obtain:

$$\begin{cases} M_{L,+}^{j} = [M_0 - (M_0 - M_{L,+}^{j-1}) \cdot e^{-\frac{T_R}{T_1}}] \cdot \cos(\alpha) \\ M_{T,+}^{j} = [M_0 - (M_0 - M_{L,+}^{j-1}) \cdot e^{-\frac{T_R}{T_1}}] \cdot \sin(\alpha) \end{cases} \tag{1.17}$$

which relates the magnetization after the application of the $(j-1)^{th}$ and the j^{th} pulses respectively.

For the sake of clarity, let's from now only consider the magnetization components after the application of each RF pulse (we therefore drop the $+/-$ notation for the magnetization and $\mathbf{M}_{+}^{j} = \mathbf{M}^{j}$). As mentioned before, if no motion happens during acquisition, the magnetization reaches the steady state condition. After a suitable amount of time, we therefore have that $\mathbf{M}^{j} = \mathbf{M}_{eq}\ \forall\ j$, where $\mathbf{M}_{eq}$ is the magnetization vector at equilibrium:

$$\begin{cases} M_{L}^{eq} = [M_0 - (M_0 - M_{L}^{eq}) \cdot e^{-\frac{T_R}{T_1}}] \cdot \cos(\alpha) \\ M_{T}^{eq} = [M_0 - (M_0 - M_{L}^{eq}) \cdot e^{-\frac{T_R}{T_1}}] \cdot \sin(\alpha) \end{cases} \tag{1.18}$$

By expressing the longitudinal magnetization M_L^{eq} as a function of transverse magnetization M_T^{eq} (*i.e.* $M_L^{eq} = M_T^{eq} \cdot \frac{cos(\alpha)}{sin(\alpha)}$), we obtain that the transverse magnetization at equilibrium is:

$$M_T^{eq} = M_0 \cdot \frac{1 - e^{-\frac{T_R}{T_1}}}{1 - \cos(\alpha) \cdot e^{-\frac{T_R}{T_1}}} \cdot \sin(\alpha) \tag{1.19}$$

An illustration of this for different excitations is shown in Figure 1.8, where we have plotted the transverse magnetization using equation 1.17 (black line) against time in seconds. In this simple example, we have set T_1 to 1500 ms, $T_R = 80$ ms, $M_0 = 1$ and the flip angle α to 10 degrees, keeping deliberately the ratio $\frac{T_R}{T_1}$ low to emphasize the effect. The transverse magnetization starts from the value of $M_0 \cdot \sin(10°) = 0.1736$, and stabilizes after 6 seconds to its asymptotic value of 0.1359 (calculated using equation 1.19, and represented in dashed gray in the Figure).

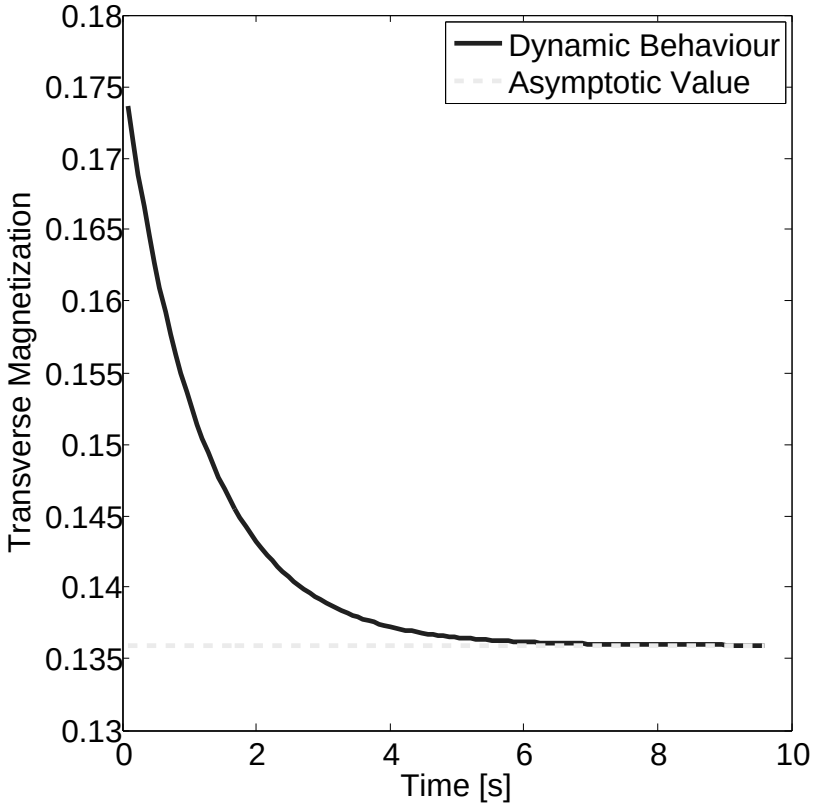

FIGURE 1.8: Transverse magnetization obtained by using equation 1.17 and its asymptotic value as described by equation 1.19.

It is also interesting to note that the Ernst Angle defined in equation 1.14 is the one that maximises M_T^{eq} [Haacke et al., 1999].

For stacks of slices repeated every T_R, the magnetization reaches the same equilibrium conditions, with precise signals dependent on local tissue properties. However, signal changes can occur if the subject moves so that the time between successive excitation of a given location in the brain is transiently different from T_R. Such signal changes are referred to as spin history effects and when they occur, the disrupted magnetization propagates to the next few acquired volumes until a new steady-state is reached.

1.4.2.7 Distortions

A major problem with EPI data is geometrical distortions that occur due to magnetic field inhomogeneities. This can hinder the registration between functional data and the anatomical images. The presence of a patient introduces inhomogeneities in the main magnetic field $\mathbf{B}_0$. We indicate this with $\Delta\mathbf{B}_0$.

Magnetic field inhomogeneities can result from imperfections in the magnet manufacturing process and susceptibility effects. The human body distorts the magnetic field due to its geometric distribution of magnetic susceptibilities (χ). More specifically, the inhomogeneities of the main magnetic field at tissue boundaries with different susceptibilities χ_1 and χ_2 is given by:

$$\Delta\mathbf{B}_0 = (\chi_2 - \chi_1) \cdot \mathbf{B}_0 \tag{1.20}$$

One example of this is air-tissue boundaries, where, for air, we have $\chi_1 = 0.3\ ppm$ and, in tissue, $\chi_2 = -9.2\ ppm$ [Wilson et al., 2002]. In addition, the susceptibility distribution varies across human subjects [Wilson et al., 2002].

Similarly to what was presented in section 1.4.2.2, the signal equation in the presence of a $\Delta B_0(x, y) = |\Delta\mathbf{B}_0(x, y)|$, is:

$$s(k_x(t), k_y(t), t) = \iint \mathbf{M}_{xy}(x, y) e^{-2\pi i(k_x(t)x + k_y(t)y)} e^{-2\pi i \gamma \Delta B_0(x,y)t} dxdy \qquad (1.21)$$

where s represents now the total signal. The main difference from equation 1.12 is that the phase term $e^{-2\pi i \gamma \Delta B_0(x,y)t}$ depends explicitly on the spatial coordinates x and y, so it cannot be brought outside the integral as in equation 1.13. Therefore, when the field varies as function of space as in this case, the shifts experienced by the signal in image space become a localised effect. In EPI this can lead to large local shifts, which manifest as image distortions.

Distortions are more severe at the boundaries between brain tissue and air in the skull. These regions, such as temporal lobes, sinuses and anterior frontal areas suffer larger magnetic field inhomogeneities. This results in greater signal distortions and, especially at longer echo times, localized signal loss due to phase accumulation effects.

Figure 1.9 shows two examples of typical distortions patterns that are observed in fetal fMRI data. This data comes as part of a protocol that is described in detail in section 2.3.1.1. However, we show here some snapshots to get the reader familiar with its typical distortion patterns. The Figure reports transverse, sagittal and coronal views of two different fetuses (first and third rows) acquired at 3T. The second and fourth rows show the undistorted anatomical single shot fast spin echo (ssFSE) images. In the fMRI data, the fetal brain appears as a bright (almost) spherical object in the middle of the field of view. Although data has been cropped, some of the maternal structures surrounding the fetal head are visible: the uterus and the maternal bladder appear as bright sacks because of the long T_2^*, and the maternal gut is characterized by low signal that occupies the rest of the image.

In the first subject, distortion manifests only as a localized phenomenon that alters the shape of the brain locally (red arrow). In the third row, distortion

affects the acquired image globally, with a strong shearing effect along the through slice direction (second red arrow).

The problem of signal drop is much less pronounced in fetuses than in ex-utero subjects. This is due to the absence of air-tissue boundaries between the fetal head and the uterus. In general, we don't observe signal loss. This is good news because it means that the original signal is completely recoverable.

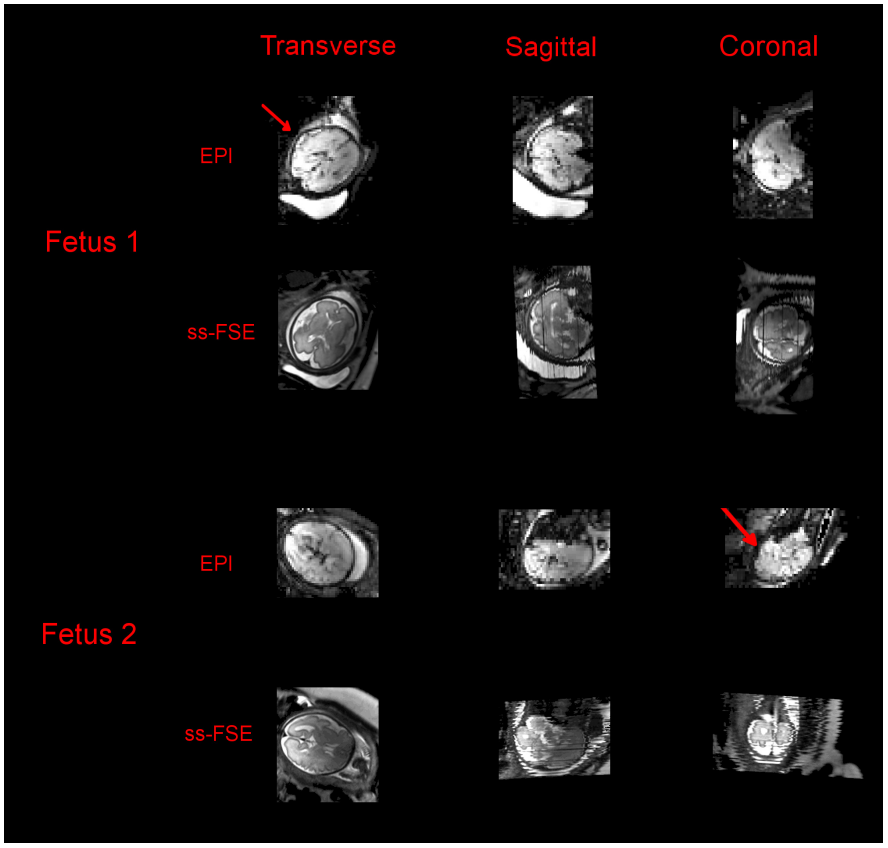

FIGURE 1.9: Example of different distortion patterns in two different fetal fMRI datasets acquired at 3T (first and third rows). Red arrows show the areas where there is larger distortion. The second and fourth rows show the corresponding anatomical ssFSE images.

1.4.2.8 Distortion Correction

Distortion Correction with Field Maps

The simplest way to correct for distortions is to make use of a field map. A field map is a measure of the underlying inhomogeneities $\Delta\mathbf{B}_0$. It can be acquired with two consecutive gradient echo images at two echo times T_{E_1} and T_{E_2}. Once this is done, an estimate (in Hz) of the field can be obtained by computing $\frac{\angle I_2 - \angle I_1}{\gamma \Delta T_E}$ [Jezzard and Balaban, 1995], where I_1 and I_2 are the two images, $\Delta T_E = T_{E_2} - T_{E_1}$ and $\angle$ the phase operator. It turns out that by combining field maps with acquired data, we can correct for distortions. According to Jezzard and Balaban [1995], an estimate of the distortion field can be obtained by computing:

$$\Delta ps_{pe} = \frac{\gamma \Delta B_0}{BW} \cdot \Delta r_{pe} \tag{1.22}$$

Here, Δr_{pe} is the resolution along the phase encoding direction and BW the sequence bandwidth (in Hz), reciprocal of the readout time. Once Δps_{pe} is calculated, the displacement field has to be applied along the phase encoding direction.

Prospective Shimming

To reduce the inhomogeneities, the scanner has at disposal extra coils that, if used, can generate fields that are superimposed on the underlying $\mathbf{B}_0$ to provide a much more homogeneous field. The practice of making the $\mathbf{B}_0$ field more homogeneous is called *shimming*. There are many different ways of performing $\mathbf{B}_0$ shimming, and it is actually a very active research area.

It is conventional for MRI systems to be equipped with shim coils that produce added fields with simple polynomial dependences on the spatial coordinates. Lower field strength scanners (1.5T and below) generally only offer first order field

variation as distortions are not as severe as at higher fields. 3T systems can have second order shim coils. In total, there are therefore eight possible extra degrees of freedom. A representation of these coils as in Koch et al. [2009] is given in Figure 1.10.

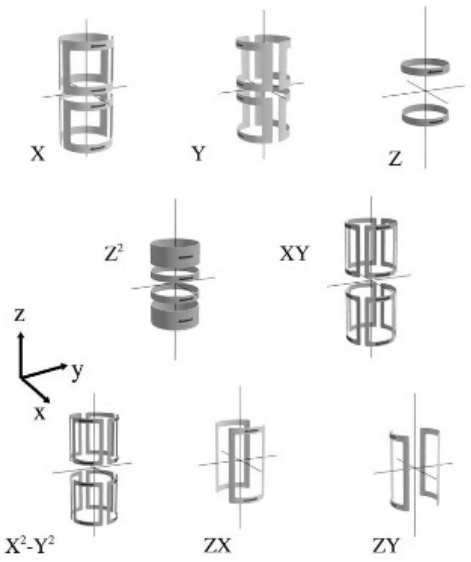

FIGURE 1.10: First and second order shim coils as described in Koch et al. [2009].

The extra terms produced by each coil are:

$$\begin{cases} \phi_1 = g_1 \cdot x & \phi_5 = g_5 \cdot zx \\ \phi_2 = g_2 \cdot y & \phi_6 = g_6 \cdot zy \\ \phi_3 = g_3 \cdot z & \phi_7 = g_7 \cdot (x^2 - y^2) \\ \phi_4 = g_4 \cdot (z^2 - 0.5x^2 - 0.5y^2) & \phi_8 = g_8 \cdot 2xy \end{cases} \tag{1.23}$$

Here, each ϕ_i represents a shim gradient and the g_i the relative *shim term*. Shim terms represent the strength with which shim gradients are applied. They are measured in $\frac{mT}{m}$ for $i = 1, 2, 3$, and in $\frac{mT}{m^2}$ for $i = 4, 5, 6, 7, 8$. After having calculated the g_i, the final field B_0^f is:

$$B_0^f = B_0 + \sum_{i=1}^{8} \phi_i \tag{1.24}$$

A good shim is therefore an estimation of the g_i that minimizes ΔB_0^f. The 3T Philips Achieva scanner that has been (mainly) used to gather data in this thesis, has at disposal two different techniques to calculate shim terms, and these methods can be selected by the radiographer prior to scanning. Specifically, if *linear shimming* is used, the scanner calculates the best values for g_i with $i = 1, 2, 3$ and the other 5 terms are automatically set to 0. If *PB-volume* (FASTMAP in the literature [Gruetter, 1993, Gruetter and Boesch, 1992]) is selected, the scanner estimates the entire set of g_i ($1 \leq i \leq 8$) in order to make the field as homogeneous as possible.

Distortion Correction with Image Based Shimming techniques

Image based shimming is a robust method that ensures great homogeneity for the $\mathbf{B}_0$ field. As the same suggests, it consists of calculating shim terms directly from acquired field maps; the latter is directly fitted using shim polynomials of equation 1.23 and the coefficients of the fit are used to set the operating point for the shim coils. More specifically, the coefficients g_i of equation 1.23 are estimated by solving:

$$\mathbf{g} = \underset{\mathbf{g}}{argmin} ||\Delta \mathbf{B}_0 - \mathbf{\Phi g}||_2^2 \tag{1.25}$$

where the vector $\mathbf{g}$ contains the shim values and the matrix $\mathbf{\Phi}$ encodes the spatial dependency of the fields.

One clear advantage of such an approach is the possibility of defining arbitrary regions of interest (ROI). The fit is performed just over those regions and, in

general, this allows a higher level of homogeneity to be achieved. The cost is paid elsewhere, where the field behaves in an uncontrolled way [Siero et al., 2009].

1.4.3 Scanner and Patient system of reference

It turned out that, in order to correct fetal fMRI data for distortions, it was fundamental to understand the relationships between different coordinates systems as defined by the manufacturer. A brief introduction is therefore given. The Philips environment defines many different coordinate systems, each of which serves a different purpose. These systems can be divided into two main groups and more specifically there are:

- **Image based coordinate systems:** which are bound to the acquired image and therefore depend on the angulation, image orientation, etc.
- **Fixed coordinate systems:** which are either bound to the patient (Patient coordinate system) or to the scanner (Scanner coordinate system).

For the purposes of distortion correction, we only need to concentrate on this second group and, more specifically, on the relationship between Patient and Scanner coordinate systems.

As the name suggests, the Scanner coordinate system defines positions in the scanner, and it coincides with the directions of the main gradients x, y and z. We will refer to this coordinate system as the $'xyz'$ system. The patient coordinate system is, on the other hand, always bound to the patient, and the main axes are aligned from their Right to Left (RL), from their Anterior to Posterior (AP) and from their Foot to Head (FH) directions. We will refer to this coordinate system as the RL-AP-FH system.

The relationship between Scanner and Patient coordinate systems is not fixed and it depends on the patient position; more specifically, if a patient changes their

pose with respect to the scanner bore, the transformation changes. A patient can in fact be imaged in the prone or supine positions, with their head entering the scanner first (head first), or, conversely, with their feet (feet first). The Patient coordinate system is useful when comparing same anatomies acquired during different scans as they will appear in the same relative space. The Scanner coordinate system is, instead, independent from all these variables and its origins coincide always with the scanner isocenter. Both coordinate systems are right handed.

There is also another very important subtle variable that influences the mismatch between these two coordinate systems; which is the motion of the table. At the beginning of every scan, a laser beam is used to set up the patient coordinate system so that its origin coincides with the isocenter, i.e. the patient and scanner coordinates have the same origin. By sliding the table across, the beam is aligned roughly to the organ to be scanned and, when moved in, the table sets that position to be at isocenter so that the imaging target is very close to it. During the scan, the table might slide in and/or outwards as the imaging targets could have changed and/or moved; this happens because the scanner is always trying to maximize the proximity of the target to isocenter, where the magnetic field has better properties. The xyz reference system is insensitive to table movements and its origin is always at isocenter. The RL-AP-FH system, however, is bound to the patient, and therefore the displacement of the table needs to be embedded into the image representation. In other words, the origin of this coordinate system will always remain fixed to the anatomy, and a table movement after the initial set up would introduce an offset that must be accounted for in any subsequent calculations.

1.5 The BOLD signal and functional MRI

fMRI has led the field of functional neuroimaging since the discovery of the BOLD phenomenon [Ogawa et al., 1990] and today it represents one the the most powerful ways to look at the functional behaviour of the human brain. The complete understanding of how neural activity couples with the BOLD signal is therefore very important.

MRI quantifies neuronal activity indirectly, by measuring changes in blood flow as a response to brain activity. To date, however, the exact physiological mechanisms underlying these interactions remain unclear and several hypotheses have been made [Magistretti and Pellerin, 1996, Sibson et al., 1998].

The starting observation is that neural activity is always accompanied by an increase of energy utilization with a consequent increase of local metabolism and glucose uptake [Duncan et al., 1987]. However, there seems not to be a linear relationship between metabolic changes in the brain and blood flow and different studies have ended with conflicting results. More evidence is therefore needed to underpin this complex phenomenon and the debate upon it is still an exciting research topic. Nevertheless, changes of local metabolism determine changes in the way blood is delivered.

The second observation is that oxygenated and deoxygenated blood have different magnetic properties [Pauling and Coryell, 1936]. However, the first study that explores the possible application to MRI was published by Ogawa [Ogawa et al., 1990]. Here, T_2^* weighed gradient echo images of a rat brain under hypo and normoxia conditions were acquired. What was observed was an increase and a decrease of the MR signal in each condition. The same Ogawa et al. [1990] suggested that this was caused by the magnetic properties of hemoglobin, the molecule responsible for carrying oxygen in the human body. When hemoglobin is bound to oxygen, it becomes diamagnetic, and therefore it decreases the local magnetic flux. Conversely, when hemoglobin releases its oxygen, local iron

increases and the molecule becomes paramagnetic [Pauling and Coryell, 1936]. Therefore, changes of oxygenation levels in vessels lead to changes in $\mathbf{B}_0$. In the case of deoxygenated blood, the increase of the flux leads to local and tiny gradients that in turn make the signal to decay faster. When the blood is oxygenated, local flux decreases and therefore the signal is more stable. The phenomenon can also be described macroscopically as a increase/decrease of T_2^* values when blood is oxygenated/deoxygenated. Besides having discovered the phenomenon, Ogawa suggested that it could have been used to map neuronal activity in the brain.

There are however deeper mechanisms that need to be described - for example: what does change the way blood is delivered when a zone of the brain becomes active and/or inactive? What are the exact mechanisms underlying this neuronal/vascular coupling? As mentioned, we still don't understand this completely. However the following considerations can be made.

The brain accounts roughly for 25 % of the entire oxygen consumption in the human body. A constant supply of oxygenated blood and glucose is therefore needed and it is maintained as such by the cerebro blood flow (CBF), which delivers blood through a complex web of vessels in the brain. Neurons increase oxygen and glucose consumptions and regulate the local CBF when they become active. However, while the fraction of cerebral blood flow and glucose consumption is very close to one, oxygen uptake is much less then CBF. The result is that an increase of oxygen is formed and, since oxygenated blood increases the local T_2^*, the net effect is an increase of the BOLD signal with activation [Allievi et al., 2013]. Another feature is that the BOLD signal is confined within the venous microvasculature structure of the cortex. This is because the oxygenation in the arteries can be approximated as constant.

The first BOLD fMRI experiments can be attributed to three different groups. Kwong et al. [1992] investigated activation in the human visual and motor cortex at 1.5T using a visual and a squeezing stimulus. A few months later, the same Ogawa published similar results [Ogawa et al., 1992]. Bandettini et al. [1992] is the first

to perform a finger tapping experiment. In this study, local signal increases were found to account for 4.3 ± 0.3% of the total signal.

In the following 20 years, the field of BOLD fMRI has grown exponentially and the progress toward mapping neuronal activity in the brain is remarkable. fMRI has nowadays reached a very high standard and the design of different experiments involves a tight collaboration between different professional figures.

1.5.1 The Hemodynamic Response Function

The response of the vascular system to a brief neuronal firing can be measured and it is called *Hemodynamic Response Function* (HRF). A qualitative representation of the HRF is given in Figure 1.11. The HRF represents the rate of change of the BOLD signal in response to a brief stimulus. Even if we won't explore in detail the exact mechanism underlying its behaviour, we can firstly notice an initial rise at a relatively slow rate. While different authors disagree on the presence or absence of an initial dip, the BOLD signal usually lags 1-2 seconds before ramping up. The maximum of the curve is reached after 4 to 8 seconds and then the signal falls back to baseline level. There might be also an under-shoot period between peak and baseline.

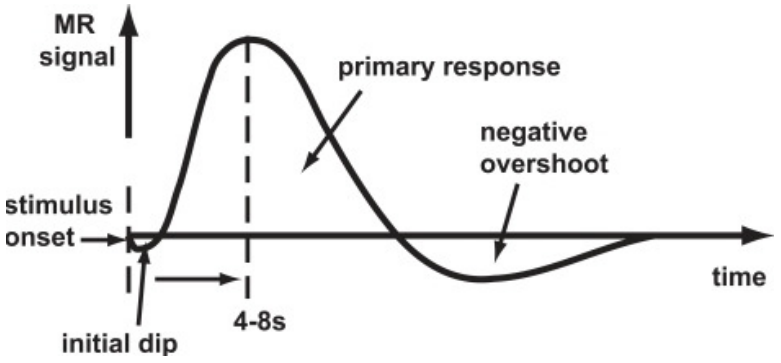

FIGURE 1.11: Standard HRF (picture from web. Ref: https://github.com/psu-psychology/psych-260/blob/master/lectures/2015-08-31/260-2015-08-31-methods.Rmd).

As the magnitude of the response is very tiny, the localization of active regions is a challenging problem because this compares to noise levels. Furthermore, the localization of the BOLD effect depends on the spatial properties of the response itself; the hemodynamic response function is indeed not spatially well specific, and tends to be large in comparison to the actual neuronal activity from which it was generated.

The main qualitative features of the HRF appear to be common to both humans and animals. However, there are many quantitative differences between species and populations and these can be actually measured. For example, Arichi et al. [2012] compares and discusses different HRFs as measured in adult and neonatal brains (Figure 1.12). In this study, fMRI data was gathered by using an event paradigm and the somatosensory cortex was stimulated via the usage of a controlled hand interface. This consisted of an inflatable balloon attached to the babies' wrist. The analysis of the data was carried out with standard software. However, a clear developmental trend for the HRF was identified; the preterm response is characterised by a delayed and broader peak compared to adults, but this delay is already substantially reduced by term equivalent age. Another feature is that the % signal change of the BOLD signal in babies is smaller. This may have been due to the combination of a tinier physiological response with an acquisition protocol that had not been optimized for the longer relaxation properties of the infant brain [Rivkin et al., 2004].

1.5.2 BOLD to noise contrast

In order to design a sequence sensitive to the BOLD effect, one has to evaluate the so called BOLD to noise contrast (BNC). This is defined as the ratio between the variation of the BOLD signal ΔS divided by the noise standard deviation of the time series (σ).

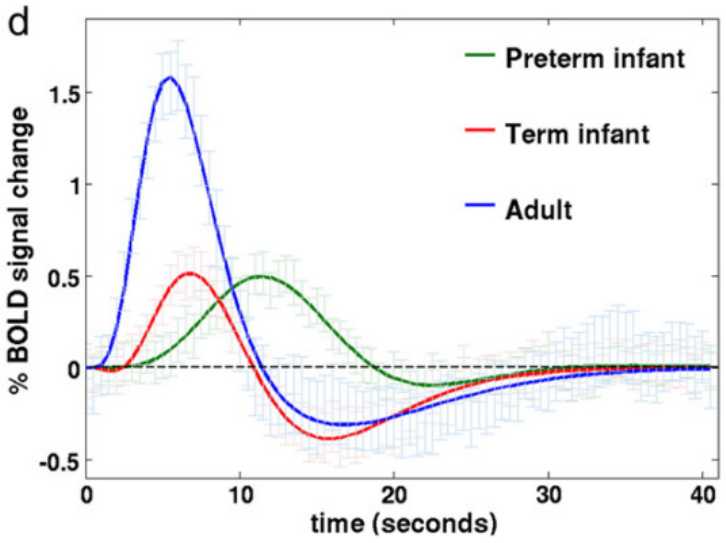

FIGURE 1.12: HRF response as measured in Arichi et al. [2012] for preterm infants (green), term babies (red) and adults (blue).

The BNC can be rewritten in an useful and operative way by multiplying the term $\frac{\Delta S}{\sigma}$ by $\frac{S}{S}$, with S representing the signal strength at the time of the echo. By bearing in mind the definition of temporal SNR ($tSNR = \frac{S}{\sigma}$), we can rewrite the BOLD to noise contrast as $tSNR \cdot \frac{\Delta S}{S}$. Let's now expand the term ΔS by modelling the BOLD phenomenon as a small increase in T_2^* values between passive and active states (say from $T_2^{*,p}$ to $T_2^{*,a}$). With this notation, $\Delta S = S_0 \cdot (e^{-\frac{T_E}{T_2^{*,a}}} - e^{-\frac{T_E}{T_2^{*,p}}})$, where S_0 is the signal available right after the RF pulse. By dividing ΔS with S, we get that $\frac{\Delta S}{S} = e^{T_E \cdot \Delta R_2^*} - 1$, where $R_2^* = \frac{1}{T_2^*}$ and $S = S_0 \cdot e^{-\frac{T_E}{T_2^{*,p}}}$. If we finally assume that activation is characterized by small changes in T_2^* ($\Delta R_2^* << 1$), we can truncate the last exponential so that $e^{T_E \cdot \Delta R_2^*} - 1 \approx T_E \cdot \Delta R_2^*$, and the BOLD to noise contrast can be written as:

$$BNC = tSNR \cdot T_E \cdot \Delta R_2^* \tag{1.26}$$

The BNC is maximized by the careful selection of the echo time T_E. More specifically, Bandettini et al. [1994] suggests that it should match the average T_2^* across

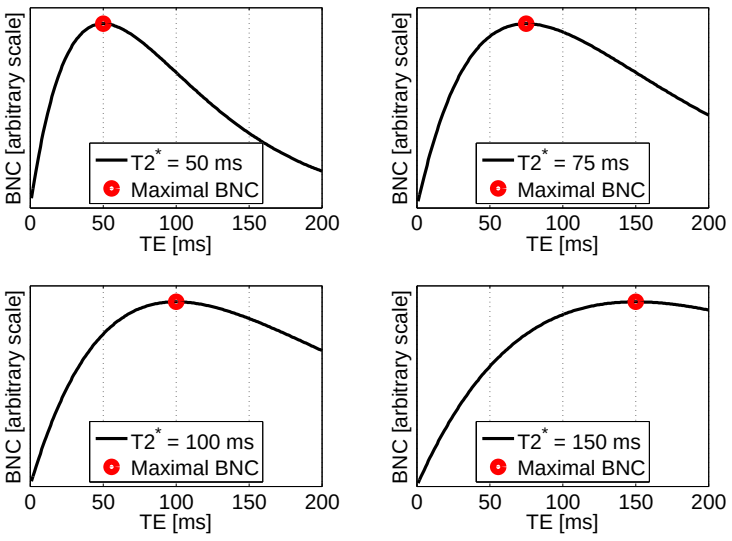

FIGURE 1.13: BOLD to noise contrast at different echo times parametrized for different T_2^* values.

the tissue under investigation. This can be easily derived by computing the zeros of the derivative of equation 1.26 with respect to T_E.

$$\frac{d}{dT_E}(tSNR \cdot T_E \cdot \Delta R_2^*) = \frac{S_0 \Delta R_2^*}{\sigma} \frac{d}{dT_E}(T_E \cdot e^{-\frac{T_E}{T_2^*}}) = \frac{S_0 \Delta R_2^*}{\sigma} \cdot e^{-\frac{T_E}{T_2^*}} \cdot (1 - \frac{T_E}{T_2^*}) = 0$$

which cancels when $T_E = T_2^*$.

Figure 1.13 shows the BOLD to noise contrast at different echo times for four different values of T_2^* (50 ms, 75 ms, 100 ms and 150 ms). These plots were obtained by computing equation 1.26 and by setting $\frac{S_0 \Delta R_2^*}{\sigma}$ to 1. The maximal BNC is also indicated by the red points, which always satisfy the condition $T_E = T_2^*$.

When T_E is chosen so that it matches the relaxation properties of the brain, the BOLD to noise contrast becomes equal to $tSNR \cdot \frac{\Delta R_2^*}{R_2^*}$. Therefore, with these settings, the only parameter from which BNC can benefit is purely tissue

dependent. The ratio $\frac{\Delta R_2^*}{R_2^*}$ is still field dependent, but it does not directly depend upon the parameters of the sequence from which it was generated.

1.5.3 Task and Resting State fMRI

There are two main ways an fMRI experiment can be done; a study can indeed be designed in the form of a task, or one can decide to acquire resting state data. The differences between these two modalities and some literature will be given in the next two paragraphs.

Task based fMRI

In this imaging modality, subjects are instructed to perform a certain task while laying in the scanner. The scope of the experiment is to infer the zones of the brain which become active in response to that stimulus.

Task fMRI data has been often considered as output of a *Linear Time Invariant* (LTI) model. This has led to the development of the so called *General Linear Model* (GLM), in which the time courses are fitted to a function that comes directly from the knowledge of the HRF, of the input, under the assumption of a linear behaviour. Although simple, this model has led to significant results when the stimulus duration was longer than 6 seconds [Glover, 1999, Robson et al., 1998]. The construction of the GLM is relatively simple: the GLM aims at describing an independent variable (the data) in terms of linear combination of various predictors. The experimental design usually determines what is the expected response of the fMRI signal; this is typically obtained by convolving the hemodynamic response function with a box-car function representing the input. As the expected response is small in comparison to the bulk signal, standard fMRI experiments usually alternate the presence of the same task repeated multiple times to as many rest periods. One can also perform multiple tasks at the same time and use multiple regressors to fit the time courses. In fMRI, all regressors

are (usually) grouped together into the so called *design matrix*. After the fitting is done, a set of coefficients is obtained at every spatial location. Activation maps are constructed by looking at the statistics of these coefficients over the residuals of the fit.

Perhaps, the most popular paradigm in task fMRI is the finger tapping experiment [Witt et al., 2008], in which subjects are instructed to tap on one of their fingers when a certain event occurs. These events can be an auditory, visual, etc. The task can also be characterized by the presence of lack of a pacing stimulus. Pacing stimuli ensure that the subject uniformly distribute their movements over predetermined periods. Finger tapping tasks and, more generally, hand movements, can also be imparted passively. For example, in the work of Allievi et al. [2013], a MR compatible device was designed to control the movement of the babies' wrist. Somatosensory BOLD activation in response to the stimulus was demonstrated.

The flexibility offered by task based fMRI has led the development of various and complicated experiments that psychologists and doctors can use to assess neurological outcomes in different populations. However, a detailed review of this material goes beyond the scope of this introduction.

Resting state fMRI and Resting state networks

Brain imaging research has proven the existence of a specific set of brain regions engaged altogether when individuals simply think to themselves undisturbed [Buckner et al., 2008].

Evidence of this phenomenon started to appear since the discovery of the BOLD phenomenon, where scientists started to acquire fMRI human data without commissioning any specific task. The purpose of these acquisitions was to gather control data for which testing different activation hypotheses using equivalent task-based experiments. However, it was soon realized that resting state data

(this was the original name attributed to these datasets) were exhibiting themselves signs of highly interconnected regions that were temporally correlated.

The first evidence of resting activity was published by the physiologist James Ingvar [Ingvar, 1975, 1979, 1984], that used an inhalable gas to map CBF in the human brain. What was observed was activation in the prefrontal regions during rest. This extraordinary results gave birth to a new area of research by revealing that the operation of the brain has a hidden and persistent complexity. The brain is actually carrying out 'tasks' when resting, and therefore activation persists even without the input of a specific stimulus.

However, the interest of the research community in this research area really exploded with the advent of PET imaging that provided a very reliable way to map neuronal activity. By the middle 90s, dozens of studies had compared rest to task activation and a lot of research was ongoing for the definition of better contrast agents. However, the advent of fMRI was in itself another milestone.

Resting State Networks (RSNs) are nowadays consistently mapped in different human populations with fMRI and are the topic of extensive Neuroscience research [Van Den Heuvel and Hulshoff Pol, 2010]. RSNs in adults suggest that involved areas are functionally relevant, and include regions involved in motor, visual, auditory, executive and memory functioning [Damoiseaux et al., 2006]. Figure 1.14 shows, for example, the results reported in the work of Damoiseaux et al. [2006], where resting state networks where mapped in adults using *Independent Component Analysis* (ICA) [Beckmann and Smith, 2004] (section 1.7). These fluctuations were always found to account for $2-3\%$ of the total variation in the data. These networks are thought to fluctuate within the range of 0.01-0.1 Hz, and their spatial distribution is often very similar to the networks obtained during a task.

One of the networks that has received a lot of attention from scientists is the

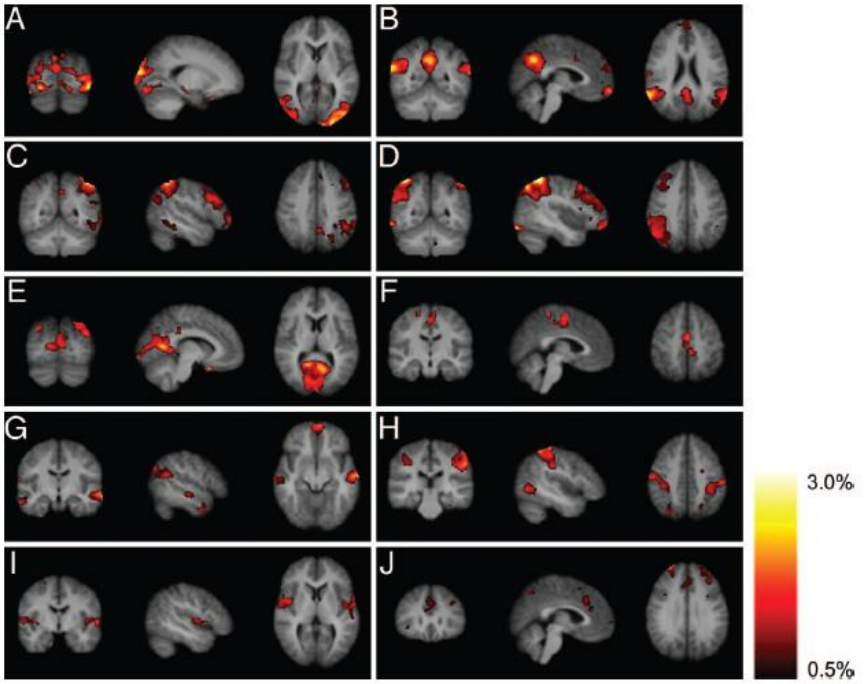

FIGURE 1.14: Multi subject resting state patterns in adults: coronal, sagittal, and axial views. Percentage of the BOLD signal changes is color coded, ranging from 0.5 % to 3 % [Damoiseaux et al., 2006].

Default Mode network (DMN) (Figure 1.14 B). The DMN has been hypothesized to be active during rest periods and to become 'quiescent' when individuals are engaged in a task. This network is thought to be confined between medial prefrontal cortex, medial termporal lobes and posterior cingulate cortex and, actually, all these regions have been found to be highly interconnected by white matter tracks [Greicius et al., 2009]. The Default Mode network starts to have clinical relevance as well; for example, Greicius et al. [2004] has proven a decreased resting state activity of this network when comparing individuals with Alzheimer and healthy aging controls.

1.6 fMRI in the newborn and in the fetus

To assess the existence of specific brain functions in fetuses, people have tried to stimulate their activation using specific visual and acoustic inputs. A visual stimulus was used in the work of Fulford et al. [2003] and the activation of the visual cortex assessed at 0.5T. Five out of nine fetuses showed significant correlation with the input stimuli in frontal regions. This was achieved by using a red LED transmitted via a 30 cm light guide. The LED was placed roughly in front of the fetal face. To minimize motion artefacts, the imaging was done after verifying that the fetal head was engaged within the maternal pelvis. Other work from the same group have established the use of an auditory and a vibroacoustic stimuli to study the fetal brain [Hykin et al., 1999, Moore et al., 2001]. In this second study, for example, an average of about 50% of the fetuses showed activation in frontal regions. In this case, the acoustic stimulus was achieved by placing an MRI compatible headphones strapped to the maternal abdomen. In Jardri et al. [2008], the hypothesis of the auditory system being active was tested for pregnancies between the 28th and 34th week. 3 out 6 fetuses, at the gestational age of 33 weeks, showed significant activation of left temporal lobe, with BOLD signal changes greater than 3.5 %.

Fransson et al. [2007], Doria et al. [2010] and Smyser et al. [2010] were the firsts to consider to use resting state fMRI in the infant and pre-terms brains. In Fransson et al. [2007], single and group ICA were used to map five unique patterns in infant babies during their sleep. Activation was found in the visual, auditory, lateral, parietal, medial and dorsolater cortex as well as in the bilateral sensorimotor areas (Figure 1.15). The time courses of these spatial maps were always within the range of 0.01-0.05 Hz, with significant correlation between right and left hemispheres. The paper makes also a comparison with the networks found by Damoiseaux et al. [2006], in which group ICA was performed in adults.

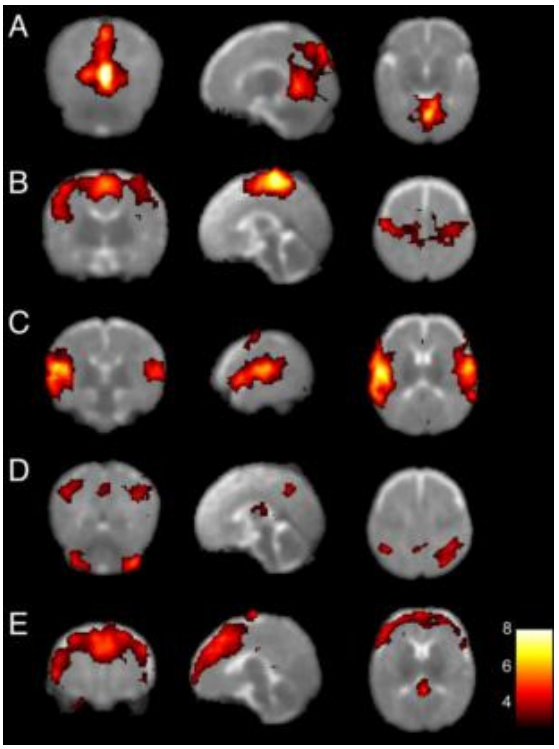

FIGURE 1.15: Group RNSs in infants as found by Fransson et al. [2007] (coronal, sagittal and axial views).

In Doria et al. [2010], the developmental trend for RSNs of 70 pre-term infants were mapped between the 29th and 43rd gestational week, and the average growth pathways were estimated (Figure 1.16). RNSs were found in the auditory, somatosensory, motor, frontoparetal and executive controls areas using ICA. To assess and quantify the convergence of RSNs towards patterns normally present in adulthood, partial correlation analysis was also used. This discovery has been considered a breakthrough in this field, since it confirms that functional maturation is already taking place in babies born prematurely, and it suggests that similar processes may happen already in *utero* (Figure 1.17).

Similar conclusions were drawn by Smyser et al. [2010], that found equivalent maturational trends for babies during the third trimester of gestation. These processes consisted of a progression from lateralized networks to bilateral patterns at full term equivalent post-menstrual age (PMA).

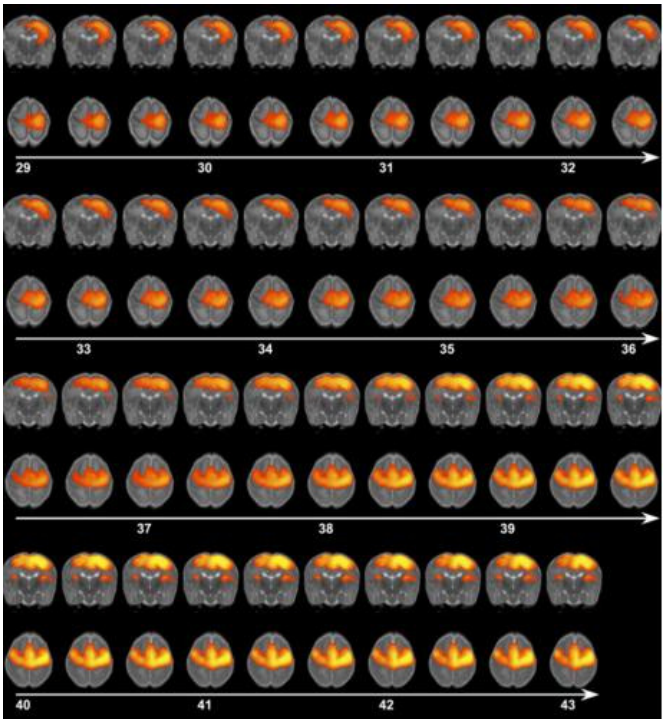

FIGURE 1.16: Motor network development in neonates over gestational age [Doria et al., 2010].

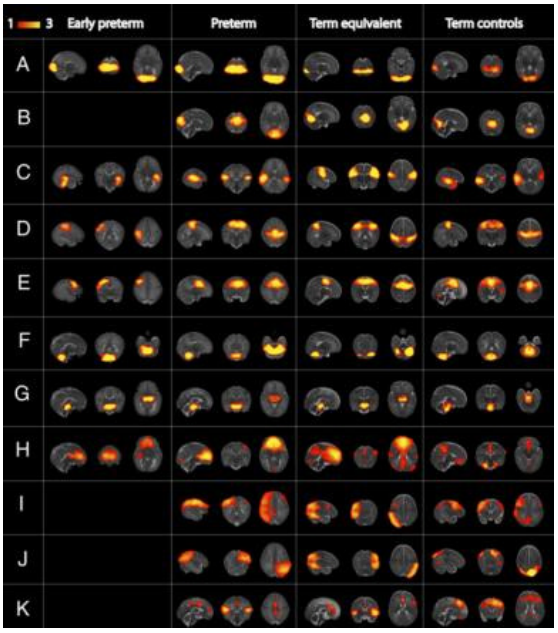

FIGURE 1.17: RSNs as mapped by Doria et al. [2010] in early preterm, preterm and term equivalent babies. The Figure reports the control group on the right hand side.

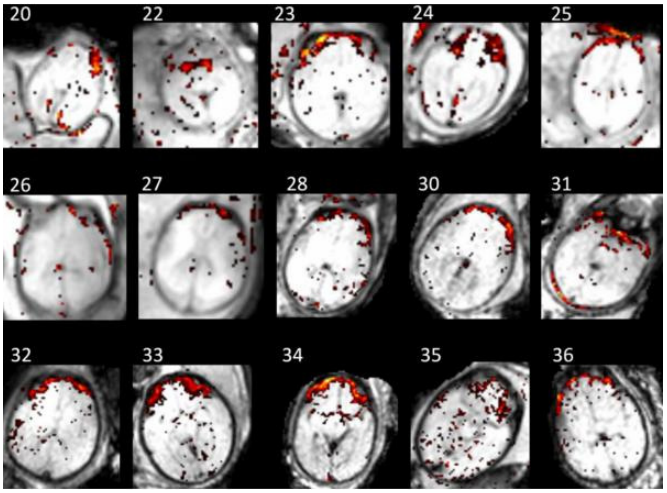

FIGURE 1.18: RSNs as found by Schöpf et al. [2012] in fetuses.

Some preliminary studies have explored fetal RSNs using conventional processing pipelines. Schöpf et al. [2012] acquired fMRI data from 87 healthy fetuses and used single subject Probabilistic ICA [Beckmann and Smith, 2004] to identify RSNs. However, because of large motion levels, 71 datasets could not be processed. Thomason et al. [2013] analysed a set of 25 healthy subjects in the second and third trimester of gestation using Group ICA [Calhoun et al., 2009] and correlation analysis. In this study, individual time frames were rejected, with single volumes removed from the time series when there was judged to be excessive motion. The reported rejection rate was 41.28%.

Figure 1.18 shows examples of RSNs as mapped by Schöpf et al. [2012]; time courses were all in the range 0.01-0.06 Hz and activity took place mainly in the frontal and in the occipital areas.

Thomason et al. [2013] confirmed the presence of strong bilateral functional connections in fetuses, as well as regional connections within same hemispheres. The authors also quantified the connection strengths between different brain regions against gestational age, and these metrics were found to increase linearly as fetuses approached full term (Figure 1.19).

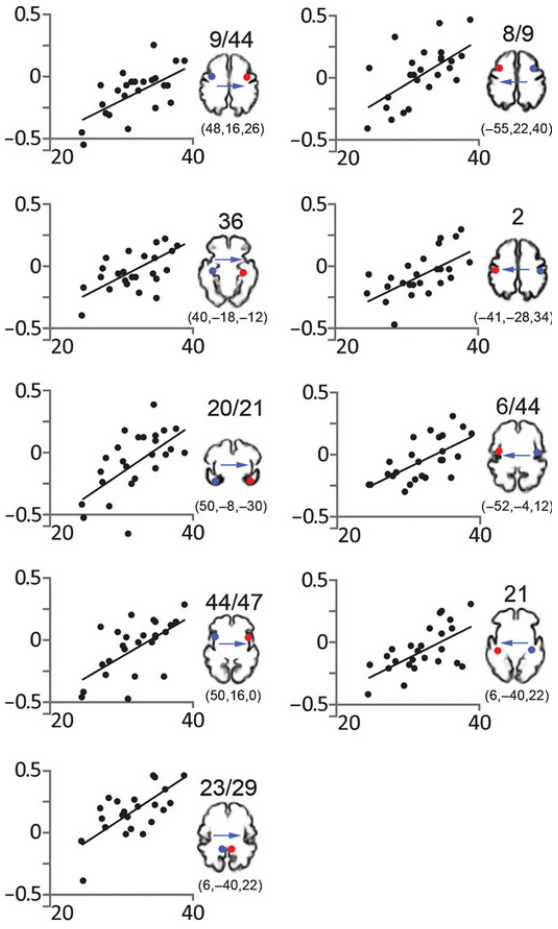

FIGURE 1.19: Correlation trends between different seed regions as found in Thomason et al. [2013]

There is another recent paper in the field of fetal fMRI [Jakab et al., 2014]. In this work, standard processing pipelines and toolboxes were adapted for fetal datasets. In total, 84% of the datasets were discarded due to motion and other artefacts. Within the datasets that were retained, a similar approach to the work of Thomason et al. [2013] (in the paper referred to as *'scrubbing'*) was adopted, where frames showing consistent damage due to high motion were discarded. After standard fMRI preprocessing steps, spatial alignment of each fetal fMRI dataset to an age-specific T_2 fetal template was achieved. Functional graphs [Bullmore and Sporns, 2009] were then constructed by looking at the correlation between anatomical landmarks. Connectivity analyses performed on each subject separately, showed sigmoid expansion of functional connectivity in the

fetal brain. This in contrast with the work of Thomason et al. [2013], where a linear behaviour had been suggested.

1.7 Independent Component Analysis

Independent Component Analysis is the gold standard method for network extraction in resting state fMRI data. Therefore, a brief introduction is given.

The most classical way to introduce Independent Component Analysis is the *cocktail party problem*. Here, a certain number of people are talking simultaneously inside a room. Multiple microphones (whose number is equal or greater to the number of speakers themselves) are placed in different parts of the room and are recording simultaneously what the various people are saying. The aim of the problem is to separate the speech track of each single person without knowing anything about the properties of the signal itself.

Several approaches have been proposed to solve this problem and, amongst the most popular ones, there are *Principal Component Analysis* (PCA) [Jolliffe, 2002] and *Independent Component Analysis* (ICA) [Hyvärinen et al., 2004]. More specifically, ICA has had a lot success in recent years as the primary tool for analysing resting state fMRI data.

An intuitive graphical representation of Independent Component Analysis is given in Figure 1.20. Here, a local implementation of ICA was run on a set of 3 images taken from the Internet and these are reported in the first row. In analogy to the cocktail party problem, these images are the 3 independent speakers talking inside the room. Furthermore, as different microphones record different combinations of voice segments, the second row reports 3 linear combinations of the input images. This is the input of the ICA model. In the third row, the result obtained after the application of the ICA algorithm is shown. It can be appreciated as the original

(A) Component 1

(B) Component 2

(C) Component 3

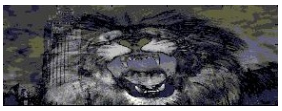

(D) Mix 1

(E) Mix 2

(F) Mix 3

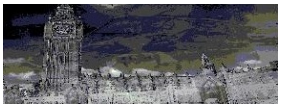

(G) Recovered component 1

(H) Recovered component 2

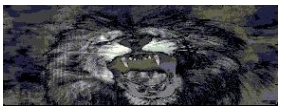

(I) Recovered component 3

FIGURE 1.20: A typical application of the ICA algorithm. Three different images (first row) - each representing a different scene - are mixed together (second row); the ICA algorithm is capable of recovering the original data (third row) without any assumption on the input images.

input images are recovered. This is achieved without any information about the original signal.

In the ICA algorithm, the images in the first row of Figure 1.20 are referred to as *components*. What ICA receives is a linear combination of those. The algorithm is then able to recover an estimate of the signal by assuming that the components are *statistically independent*.

1.7.1 The forward model

ICA definition is given in a similar fashion to what can be found in Hyvarinen [1999].

Let's consider with $\mathbf{x} = (x_1, x_2, ..., x_m)^T$ a m dimensional random variable. The input data has to be considered as the realization of $\mathbf{x}$. Let's also denote with $\mathbf{s} = (s_1, s_2, ..., s_p)^T$ a p dimensional random variable representing the components. ICA assumes a linear relationship between these two quantities so that:

$$\mathbf{s} = \mathbf{W}\mathbf{x} \tag{1.27}$$

In this formulation, $\mathbf{s}$ is a random vector formed by a finite set of *non Gaussian independent random variables*, and $\mathbf{W}$ a p by m matrix of fixed coefficients called *unmixing matrix*. The matrix $\mathbf{W}^{-1}$ is referred to as *mixing matrix*. It is important to note that the dependence between the elements of $\mathbf{x}$ is only due to the mixing matrix $\mathbf{W}^{-1}$, and it does not derive from the properties of $\mathbf{s}$. This is because each random variable s_i in $\mathbf{s}$ is assumed to be statistically independent from all others. A set of random variables s_i are statistically independent if

$$f(s_1, s_2, ..., s_P) = f(s_1) \cdot f(s_2) \cdot ... \cdot f(s_P) \tag{1.28}$$

where f is a function representing the probability density function.

If we knew the values of $\mathbf{W}$, finding the components would be straightforward by simply applying 1.27. Unfortunately, $\mathbf{W}$ is an unknown, and it needs to be estimated from the available data by the maximization of certain criteria.

A (sometimes) more useful representation of the model can be obtained by considering the inverse relationship between $\mathbf{x}$ and $\mathbf{s}$, which is:

$$\mathbf{x} = \mathbf{W}^{-1}\mathbf{s} \tag{1.29}$$

A brief overview of the most popular method for performing ICA, the fastICA algorithm [Hyvarinen, 1999] is given in the following paragraph.

1.7.2 The fastICA algorithm

There are several ways to estimate $\mathbf{W}$ [Cardoso, 1997, Hyvarinen, 1999], each via the maximization or minimization of an appropriate contrast function. However,

the fastICA algorithm [Hyvarinen, 1999] is usually regarded as the most efficient and it is implemented in many fMRI software packages. The scope of the contrast function is to measure the statistical independence (or dependence) between the elements of $\mathbf{s}$. In the case of the fastICA algorithm, the contrast function usually depends on quantity that, in information theory, is called entropy.

For a random vector $\mathbf{y} = (y_1, y_2, ..., y_p)^T$ with density function f, its entropy is defined as:

$$H(\mathbf{y}) = -\int f(\mathbf{y}) \cdot \log f(\mathbf{y})\, d\mathbf{y} \tag{1.30}$$

Entropy is a measure of uncertainty of $\mathbf{y}$, and it quantifies the average information that is necessary to describe it. The contrast function used by the fastICA algorithm is negentropy, which is defined as:

$$J(\mathbf{y}) = H(\mathbf{y}_{gauss}) - H(\mathbf{y}) \tag{1.31}$$

where $\mathbf{y}_{gauss}$ is a Gaussian random variable with the same covariance matrix as $\mathbf{y}$. It turns out that maximizing negentropy is equivalent to find the directions for which independency between components is maximized. This is also equivalent of finding the unmixing matrix $\mathbf{W}$. Maximizing 1.31 is, however, not straightforward and in Hyvarinen [1999] an approximation is given:

$$J(y_n) = [E\{G(y_n)\} - E\{G(v)\}]^2 \tag{1.32}$$

where G is an (appropriate) non quadratic function, v a Gaussian variable with zero mean and unit variance and E the expectation operator.

If we now perform the substitution $y_n = s_n$ and use equation 1.27, the function to maximize negentropy becomes:

$$J(\mathbf{w}) = [E\{G(\mathbf{w}^T\mathbf{x})\} - E\{G(v)\}]^2 \tag{1.33}$$

where $\mathbf{w}$ represents a row of $\mathbf{W}$. The fastICA algorithm is an efficient way to solve equation 1.33 that makes use of a fixed point iteration scheme. The algorithm is constrained to work when the number of components equals the number of dependent variables (i.e. $p = m$). However, details about the algorithm go beyond the purposes of this introduction, and we refer the reader to the actual paper [Hyvarinen, 1999].

1.7.3 Probabilistic Independent Component Analysis

An extension of the fastICA algorithm has been proposed in Beckmann and Smith [2004]. Here, a new model for the analysis resting state fMRI data has been developed. This model is implemented in the FSL sofware package and more specific in the 'Melodic' program. The model, whose name is *Probabilistic Independent Component Analysis* (PICA), is an extension of what presented in section 1.7.1 that allows the presence of noisy measurements in the fMRI time series. In the simple ICA model of equation 1.29, the random variable $\mathbf{x}$ is completely predetermined by the knowledge of the independent components and mixing matrix. This means that statistical tests are not possible. Obviously, by modelling noise, this becomes feasible.

The model reads the following equation:

$$\mathbf{X} = \mathbf{W}^{-1}\mathbf{S} + \boldsymbol{\eta} \tag{1.34}$$

Here, the matrix $\mathbf{X}$ represents the input data and it is created by reorganizing the 4-dimensional fMRI dataset into a 2 dimensional vector. The vertical direction of the matrix $\mathbf{X}$ coincides to the number of time points m of the fMRI data and

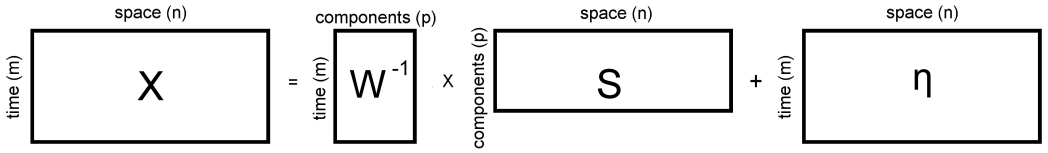

FIGURE 1.21: ICA matrix decomposition as in formula 1.34.

the horizontal dimension n is the number of voxels (i.e. a vectorised list of the signal values in every voxel in one complete dataset). The matrix $\mathbf{X}$ can therefore be thought of as a set of n realizations of the random variable $\mathbf{x}$ of section 1.7.1 that, in turn, lives in an m dimensional space. $\mathbf{S}$ is a p by n matrix representing the components and $\mathbf{W}^{-1}$ the mixing matrix. A graphical representation of this decomposition is given in Figure 1.21.

The first step is to subtract the mean from $\mathbf{X}$. The mean is added back again once the algorithm has converged. Data is then whitened [6] and let's denote this new dataset as $\hat{\mathbf{X}}$. The effect of whitening is that the term $\boldsymbol{\eta}$ of equation 1.34 describing orthogonal Gaussian noise of unknown variances ($\boldsymbol{\eta} \sim \mathcal{N}(0, \sigma_i^2)$) becomes isotropic at every location (i.e. $\sigma_i = \sigma \ \forall \ i$ - with i listing voxels).

One of advantages of the PICA algorithm is that it allows fewer components than the number of time points (i.e. $p < m$). Let's assume that p is known. In these conditions, the paper provides a maximum likelihood estimation for the mixing matrix $\mathbf{W}^{-1}$:

$$\bar{\mathbf{W}}^{-1} = \mathbf{U}_p(\boldsymbol{\Lambda}_p - \sigma^2\mathbf{I}_p)^{\frac{1}{2}}\mathbf{Q}^T \tag{1.35}$$

where $\mathbf{U}_p$ and $\boldsymbol{\Lambda}_p$ contains *the first* p eigenvectors and eigenvalues obtained by using the singular value decomposition [Golub and Reinsch, 1970] of $\hat{\mathbf{X}}$. Here, $\mathbf{Q}$ is a simple (but unknown) rotational matrix.

[6] Whitening is a mathematical procedure for which the eigenvalues associated to the eigenvectors of the covariance matrix ($\mathbf{R}_X = \mathbf{X}\mathbf{X}^T$) are normalized to 1.

An important observation is therefore the following: since $\mathbf{U}_q$ and $\mathbf{\Lambda}_p$ are fixed for some given data, the estimation of the mixing matrix $\mathbf{W}$ is equivalent to the estimation of the rotational matrix $\mathbf{Q}$. Beckmann and Smith [2004] also gives the maximum likelihood estimation for σ, which is:

$$\bar{\sigma} = \frac{1}{m-p} \sum_{l=q+1}^{p} \lambda_l \tag{1.36}$$

where λ_l are the remaining $m - p$ eigenvalues.

While the mathematical details of this go beyond the scope of the introduction, the right interpretation of these equations is important. Once the right number of components p is established, data can in all effects be considered as sharply divided between useful information and isotropic noise. The $m - p$ lowest eigenvalues of the covariance matrix are used to estimate its standard deviation. This is then subtracted off the first p eigenvalues (term $-\sigma^2\mathbf{I}_q$ of equation 1.35) along the directions of the corresponding eigenvectors. Once this subspace is defined, the direction of statistical independence is a rigid rotation of this subspace (term $\mathbf{Q}$).

The estimation of the matrix $\mathbf{Q}$ is achieved by using the fastICA algorithm of section 1.7.2. This can be done because of the existence of the following relation:

$$\mathbf{s} = \mathbf{W}^{-1}\mathbf{x} = \mathbf{Q}^{-1}\hat{\mathbf{x}} \tag{1.37}$$

Once $\bar{\mathbf{Q}}^{-1}$ is obtained, an estimate of $\bar{\mathbf{S}}$ is calculated with a least squares fit:

$$\bar{\mathbf{S}} = (\bar{\mathbf{Q}}^{-T}\bar{\mathbf{Q}}^{-1})^{-1}\bar{\mathbf{Q}}^{-T}\hat{\mathbf{X}} \tag{1.38}$$

In this introduction, we will not discuss the detection of the p dimensional subspace. This is however done automatically by Melodic with a completely data driven approach.

In general, the effect of Probabilistic Independent Component analysis on fMRI data is the separation of the signal into a set of '*spatially statistically independent*' components. Each component is characterized by a unique time course.

There are many different flavours of PICA and fMRI data can actually be analysed in many different ways. One could, for example, estimate resting state maps at the subject level. It is also possible to define networks characterizing entire subject populations. In this case, all datasets are spatially aligned into a template space and then simply 'concatenated' along the time dimension and this is the approach that we have used for the identification of networks in fetuses.

1.8 Fetal motion and motion tolerant techniques in fetal MRI and fMRI

Motion severely corrupts imaging techniques such as fMRI and it manifests in the form of image artefacts. The best way to cope with motion is to persuade the study subject to remain still so minimising movement during imaging.

In fMRI, motion correction strategies usually involve the realignment of each acquired volume to a reference image. However, in addition to misalignment of anatomy, motion generally results in additional concomitant signal changes - spurious noise components are indeed formed each time the head changes position in the scanner and the magnitude of the noise is comparable to the BOLD effect [Friston et al., 1995, 1996]. Furthermore, other studies have proved that motion correlates to the BOLD signal and therefore their separation is, theoretically, impossible [Bullmore et al., 1999, Hajnal et al., 1994, Power et al., 2012].

Another typical strategy to cope with motion is to delete the most corrupted frames (*scrubbing*) [Power et al., 2012]. However, the larger the fraction of the data that is excluded, the greater the risk of bias. Such an approach is also inefficient in data usage, so decreases statistical power.

Sometimes, and especially when motion happens throughout the acquisition, it becomes necessary to discard entire datasets. For example, in the neonatal fMRI literature, we often find a high data rejection rate [Damaraju et al., 2014, Doria et al., 2010]. Furthermore, in section 1.6, we have already outlined the high data rejection that has characterized all previous fetal fMRI attempts [Jakab et al., 2014, Schöpf et al., 2012, Thomason et al., 2013].

There are also other strategies to cope with motion: the so called prospective methods make use or optical tracking devices or MR navigators to modify in real time the strength and direction of the gradients, accounting therefore for subject change of pose [Maclaren et al., 2013].

There are also retrospective methods that perform the correction after acquisition. In the case of fMRI data, these methods usually involve an inter-volume realignment step, scrubbing and denoising. The process of denoising is done in many different ways: the most common practice is to use motion time series as regressor of the GLM model [Friston et al., 1996]. However, there are studies that made use of independent component analysis to remove spatially independent components that were motion-related [McKeown et al., 2006], and others that regressed out nuisance noise from time series using well established physiological hypotheses [Glover et al., 2000].

The development of all these techniques arose because fMRI is an invaluable tool for assessing brain functions for a different and wide range of patients. However, it is very challenging to acquire high-quality fMRI data in fetuses and/or neonates since interaction between patient and operator is very limited.

Fetuses move sporadically and in an unpredictable fashion [Malamateniou et al., 2013]. These movements take place in both the in-plane and the out-of-plane directions. Motion, particularly head rotations and nodding, can be rapid. The quality and duration of periods of motion varies with gestational age, such that, as the fetuses get larger later in pregnancy, they may have longer quiet periods and body motion is more constrained [Hayat et al., 2011]. Figure 1.22 illustrates an example of changes in fetal position for a 28 week old fetus over a period of 4 minutes. The Figure shows 3 images taken from a real-time balanced steady state free precession (bSSFP) cine sequence acquired at 3.3 frames per second and it can be observed how the fetus changes position very frequently.

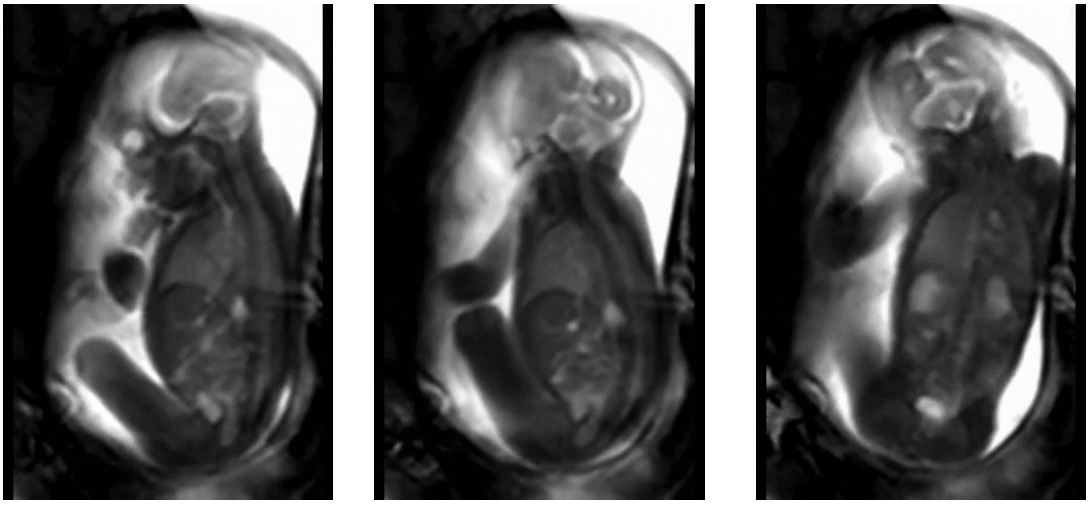

(A) Frame 1. (B) Frame 2. (C) Frame 3.

FIGURE 1.22: Three different frames taken from a real time cine MR sequence showing significant motion in a fetal subject at 28 weeks of gestation. The frames were extracted approximately at 18, 36 and 90 s from the beginning of the acquisition.

The high level of motion exhibited by fetuses has therefore justified the development of alternative strategies for prospective and retrospective motion correction. In the first case, sequences have been considerably accelerated. For example, the adoption of ssFSE sequences to image the fetal brain has proven to be beneficial in terms of image artefact reduction [Huppert et al., 1999]. In this technique, an echo train is formed via the application of a 90° degree excitation followed

by multiple spin echo refocusing pulses. The result is a heavily T_2 weighted image. This acquisition strategy, which is nowadays a standard in clinical practice, can be combined with other imaging techniques such as SENSE [Pruessmann et al., 1999] and Partial Fourier acquisition [Margosian et al., 2007]. SENSE is an acquisition-reconstruction method that makes use of the redundant information coming from multiple receiver coils to reconstruct an image acquired using highly undersampled k-space data. To work correctly, the technique needs to gather information about the spatially varying sensitivity distribution from all coils. This can be done via the usage of reference scans prior to the actual sequence. Partial Fourier techniques achieve a reduction of the imaging time by partial k-space coverage. Missing data can be inferred by using the k-space symmetry rule.

ssFSE sequences are designed to acquire individual 2D slices in hundreds of milliseconds. The result is that fetal motion can be considered as *frozen* for each slice. However, since the fetal head position changes in a complex series of 3 dimensional movements, and since the time needed to complete an ssFSE sequence can take up to 1-2 minutes, the anatomical content within each slice at a fixed location in the scanner can change substantially. Within any single stack of slices that provide whole brain coverage, the fetus may therefore change position significantly, so that the conventional approach of correcting motion by realigning whole imaging volumes is likely to result in registration errors.

This problem has motived the development of retrospective motion correction techniques that have been denominated *slice-to-volume registration* methods. They rely on the much more plausible assumption that motion manifests on the time-frame of the acquisition of each single slice. In these methods, each slice is treated independently and it is assumed that it undergoes rigid motion; subsequent slices might therefore be characterized by a different motion history, and the slice to volume registration procedures aim at the estimation of their positions.

Slice to volume techniques are more powerful than normal 3D registration methods since they can model the signal more accurately; in the context of fMRI, for example, 3D registration assumes that each volume is absolutely stationary within the time taken for its acquisition, or T_R. Furthermore, it relies on the assumption that the entire extent of motion happens exclusively between the acquisition of last and first slices of two different and consecutive volumes. Slice to volume registration techniques, instead, allow for a finer grained rapid description of the signal.

The field of fetal imaging has seen the implementation of many slice to volume registration routines mostly for ssFSE images [Gholipour et al., 2010, Jiang et al., 2007, Kim et al., 2010, Kuklisova-Murgasova et al., 2012, Rousseau et al., 2006]. An example among these studies is the work developed by Kuklisova-Murgasova et al. [2012], where the authors developed an automatic registration method for the reconstruction of fetal MRI data. Starting from the acquisition of 2D anatomical slices coming from 3 orthogonal planes, the method is able to reconstruct high resolution and high SNR volumetric data by realigning each slice into an anatomical space. Furthermore, the method includes super resolution techniques, stack intensity-matching and robust statistics for outliers' exclusion. Figure 1.23 shows an example of a fetal head acquired with a ssFSE sequence under extreme motion (first row), and the volume after motion correction (second row).

Another method was developed by Jiang et al. [2007]. Here, a similar framework was implemented in order to account for motion in the fetus. We will illustrate the functioning of the method is section 2.2.1.4.

The first paper that investigated slice to volume registration in fMRI data was published by Kim et al. [1999]. Here, an automatic registration pipeline was built up in order to account for inter-slice motion in adults. The authors demonstrated how this approach resulted in better performances when compared with conventional methods. As reference, the authors acquired a T_1 anatomical scan, with

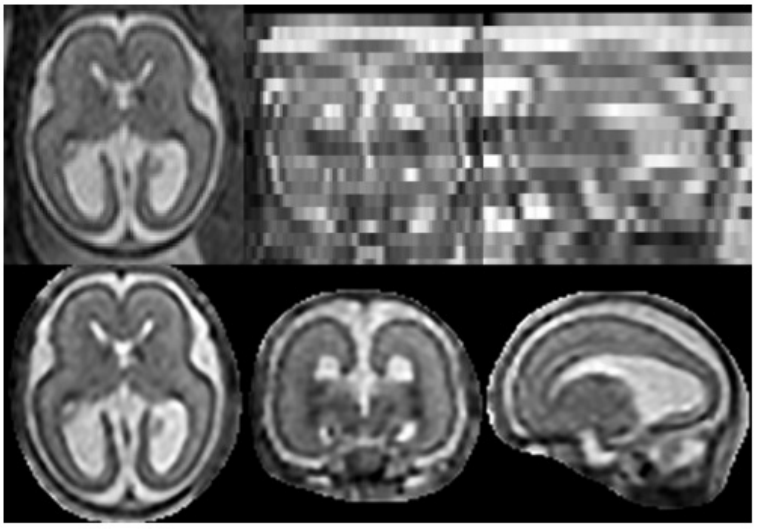

FIGURE 1.23: (First row): Transverse, coronal and sagittal views of a 23 weeks old fetus from a ssFSE image. (Second row): Image reconstruction using the algorithm published in Kuklisova-Murgasova et al. [2012].

high resolution and SNR. As cost function, they chose mutual information [7], and the problem of aligning each slice was solved using gradient descent.

There have been 2 other studies that corrected for fetal fMRI motion using a slice to volume registration approach. In Seshamani et al. [2013], a cascade slice to volume registration was built and applied to data acquired with a 3 mm isotropic resolution, T_R of 2000 ms and echo time of 50 ms. The pipeline included a distortion correction step (field map estimation from multiecho fMRI data), frame motion estimation and 2 levels of slice to volume registration. In Seshamani et al. [2015], a similar method was applied to the field of R_2^* mapping.

[7] Mutual Information (M) between images X and Y is defined as: $M(X,Y) = -\sum\sum p(x,y)\log\frac{p(x,y)}{p(x)p(y)}$. Here, X and Y represent reference image and the one to be processed, $p(x)$, $p(y)$ and $p(x,y)$ are singles and joint probability density functions from sample x and y taken from X and Y.

Chapter 2

Resting state fMRI in the moving fetus: a robust framework for data analysis

2.1 Motivation

The main motivation for this study is that the work of Doria et al. [2010] and of Smyser et al. [2010] suggests that it is of great interest to look at the development of RSNs directly *in utero*. However, this is a challenge, as during the several minutes taken to acquire a typical fMRI dataset, the fetal brain undergoes large-scale motion caused by changes in fetal position within the womb and also as a result of maternal respiration.

As mentioned in the literature review section, there have been some pioneering studies that explored fetal resting state fMRI using conventional processing pipelines. All of these studies led to a considerable amount of discarded data, mainly because of signal damage caused by motion.

This chapter proposes a framework for processing fetal fMRI data that is designed to operate when there is large-scale and frequent movement. It is divided into two macro subsections; the first that deals with data acquired at 1.5 Tesla, and the second that reports the results obtained on a larger population sample acquired at 3T.

The proposed approach seeks to directly accommodate movement on a slice-by-slice timescale and to correct for signal variations due to changes in position of the fetal head with respect to a spatially varying receiver coil sensitivity distribution. Image distortions caused by the usage of an EPI readout are also discussed and addressed. A consequence of fetal motion is that anatomical locations are sampled at irregular time intervals introducing spin history effects that are likely to be variable [Bhagalia and Kim, 2008, Yancey et al., 2011]. The proposed method seeks to model and correct for these, before rendering the now scattered data samples back onto a regular coordinate system, enabling further analysis by standard methods such as Group ICA. The aim is to achieve a robust framework that allows as much as possible, ideally all, of the acquired data to be retained and used as part of the Resting State Network analysis.

2.2 Fetal Resting State fMRI data at 1.5T

2.2.1 Material and Methods

2.2.1.1 Acquisition

This first set of data was from 16 fetuses (mean gestational age: 30.37 $\pm$ 4.35 weeks) who had been assessed as normal and were scanned on a Philips Achieva 1.5T scanner with a 32 channel receiver coil using single shot EPI ($T_R = 4000$ ms, $T_E = 50$ ms acquired with an in-plane resolution of $2.5 \cdot 2.5$ mm^2 and slice thickness of 5 mm). During each T_R interval, 35 slices were acquired with

interleaved slice ordering (1-3-5-7...2-4-6-8...). We denote the time to acquire a single slice as T_S.

To make the sampling as dense as possible, the slice positions were overlapped by up to 2.5 mm, with the overlap selected to ensure a large enough stack volume to encompass the fetal brain with a margin for motion.

A SENSE factor of 2 was used for all EPI acquisitions with calibration scans obtained at the beginning of the examination. Since the receiver coil used was fixed relative to the maternal anatomy, fetal movements within the womb changed only local anatomical content, with no substantial effects on coil sensitivity maps. The SENSE calibration scans were rerun if the mother changed her position substantially with respect to the scanner bore during the examination. This was easily detected as all fetal images also contain substantial information about the maternal anatomy.

To reconstruct the acquired data, the scanner software was used and magnitude images were made. Furthermore, all fMRI scans were within the regulatory SAR limits, and the sequence acoustic noise was measured and assessed to be low.

A complete fMRI acquisition consisted of 100 volumes acquired in a single dynamic time series. We also acquired a smaller number of volume stacks of slices in the coronal and sagittal planes to assist the registration algorithm by providing spatial information from different orientations. The phase encoding direction for transverse and sagittal views was Anterior-Posterior, so that spatial distortions were nominally in the same direction for these acquisitions. The number of acquired frames in the coronal and sagittal directions was chosen depending on the available scanning time. ssFSE images were also acquired in 3 nominally orthogonal anatomical planes for all subjects ($T_R = 15000\ ms$, $T_E = 180\ ms$, 5 packages with a resolution of $1.25 \cdot 1.25\ mm^2$, 2.5 mm slice thickness overlapped by 1.25 mm).

Functional studies employ prolonged data acquisitions, in this case almost 7 minutes for the transverse view. This is longer than routinely used for purely anatomical imaging, which in our practice consists of multiple shorter acquisitions typically lasting 1-2 minutes each.

There is thus an increased risk that fetuses may change position substantially in the womb during an fMRI acquisition. Despite prescribing imaging stacks with larger anatomical coverage than the actual fetal brain dimensions, there were 3 subjects that moved sufficiently to cause part of the brain to be outside the field of view, resulting in unrecoverable data loss (Figure 2.1, A). In a further 2 subjects there was substantial localized signal loss in part of the brain caused by gas bubbles in the maternal gut (see example in Figure 2.1, B). These 5 cases were excluded from this study.

Table 2.1 summarizes gestational age, slice overlap and the number of frames that were acquired in the coronal and sagittal directions for every subject that was imaged. Those subjects that were excluded because of incomplete data are shaded in blue.

The remaining 11 datasets constituted the study population upon which the methods were tested; in these instances subjects labelled 1-8 could be fully processed, and those labelled 9-11 couldn't be corrected because of excessive motion not recoverable by the registration algorithm.

2.2.1.2 Processing Pipeline

To process the acquired data we define two distinct coordinate systems: $\mathbf{S}_1$ denotes the native scanner space, and $\mathbf{S}_2$ represents a coordinate system fixed relative to the moving fetal brain. Different processing stages operate either in $\mathbf{S}_1$ or $\mathbf{S}_2$, and are schematically represented in Figure 2.2 (all reported symbols will be defined later on).

Fetus	Weeks	Overlap (mm)	Frames (Cor, Sag)	Comments
1	32	1.5	10, -	Corrected
2	34	2	10, 10	Corrected
3	26	2.5	10, 10	Corrected
4	30	2.5	2, -	Corrected
5	27	2.5	10, -	Corrected
6	38	1	10, 10	Corrected
7	36	2.5	10, 10	Corrected
8	33	2	10, 10	Corrected
9	33	1.5	20, -	Excessive motion
10	25	2.5	20, -	Excessive motion
11	26	2.5	20, 20	Excessive motion
12	34	2.5	20, -	Out of FOV
13	26	2.5	2, -	Out of FOV
14	27	2.5	20, -	Out of FOV
15	25	2.5	-, 20	Bubble
16	34	2.5	20, -	Bubble

TABLE 2.1: Fetal gestational age, amount of overlap between slices and number of frames in coronal and sagittal directions.

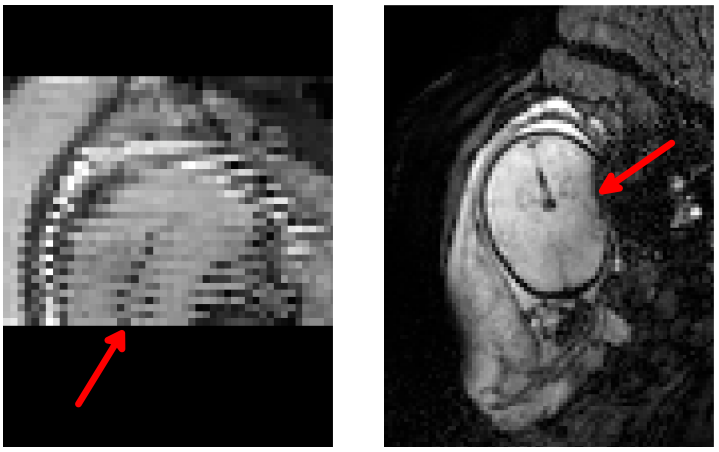

(A) Brain out the field of view.

(B) Signal drop due to bubble artefact.

FIGURE 2.1: In (A) the fetus moved so that part of the brain was no longer within the imaging volume (red arrow). In (B) a gas bubble in the maternal intestine caused signal loss in the fetal brain (red arrow).

The proposed framework is divided into 4 different parts: prior to any motion correction, bias field correction is applied to remove spatially variable receiver coil sensitivity. This is done in the native Scanner coordinates since the bias field is fixed relative to the maternal anatomy. Following this, a robust slice to

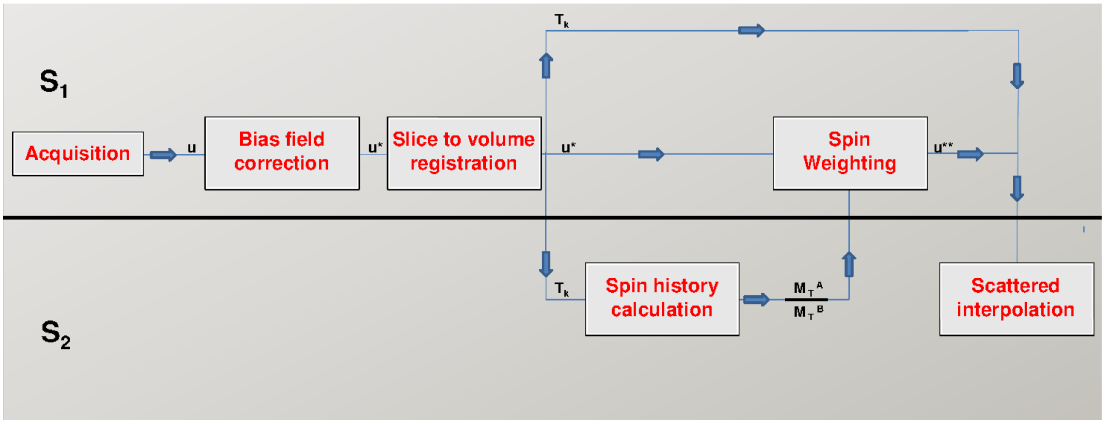

FIGURE 2.2: Processing Pipeline.

volume registration realigns each acquired slice into a consistent anatomical space. Information from image registration is then incorporated into a forward model of the imaging process to quantify saturation effects so that fMRI data can be corrected for these incidental fluctuations. Finally, the corrected scattered data in $\mathbf{S}_2$ space is interpolated onto an uniform voxel grid so that it is suitable for subsequent fMRI analysis. Four different interpolation methods for this important step were tested using simulated data for which a ground truth is known. The method with best performances was selected and used on *in vivo* data.

2.2.1.3 Bias Field Correction

As a preprocessing step, a binary mask was manually delineated around each fetal head. Masks were kept as close as possible to the fetal brain, but needed to be large enough to contain its full range of motion.

In fetal MR imaging, the receiver coils are strapped to the mother's abdomen, and therefore the receiver radio-frequency field $\mathbf{B}_1^-$ is consistent in the space of acquisition ($\mathbf{S}_1$) and does not vary with time provided the mother does not perform any gross movements. The coil elements are necessarily some distance from the fetal brain, so $\mathbf{B}_1^-$ is generally slowly varying in space on the scale of the fetal head. However, due to fetal motion, this intensity variation is not consistent

with respect to the fetal anatomy and so can effect both the performance of the registration algorithm used to perform motion-correction as well as the estimated fMRI signal.

The practise of estimating and removing $\mathbf{B}_1^-$ from the acquired data is called Bias Field correction and there have been numerous studies in the literature attempting this [Sled et al., 1998, Styner et al., 2000, Vovk et al., 2007]. The majority of these methods dealt with high resolution T_1 or T_2 weighted images in adults and, in one case, anatomical T_2 weighted images in the fetus [Kim et al., 2011]. There has been also one study that attempted to estimate $\mathbf{B}_1^-$ in fetal fMRI data [Seshamani et al., 2014].

Unlike previous fetal MRI bias-correction methods [Kim et al., 2011, Kuklisova-Murgasova et al., 2012] which were designed to correct bias field inconsistencies between acquired slices, our proposed method estimates the global volumetric bias field in the scanner space and can be considered an extension of the method proposed in the work of Wells III et al. [1996]. We take advantage of the fact that our fetal fMRI data have very low contrast between different brain tissues (white matter, grey matter and cerebro-spinal fluid) and amniotic fluids. Only narrow regions of low signal are detected from bone in the skull.

To estimate $\mathbf{B}_1^-$, we separate the voxels in the region of interest into two classes by fitting a mixture of Gaussians using the EM algorithm [Dempster et al., 1977, Duda et al., 2001]. The multiplicative bias field impacts the higher intensity class much more significantly than the lower intensity class, thus separation of these two classes is preserved even in presence of relatively high $\mathbf{B}_1^-$ inhomogeneity; Figure 2.3 shows the original estimated probability density functions (pdf) of the entire fMRI data for each of the 8 subjects before bias field correction is applied and demonstrates that a two class model is suitable (even for fetus number 5, where the assumption of a double class model was initially least well fulfilled, the bias correction worked well).

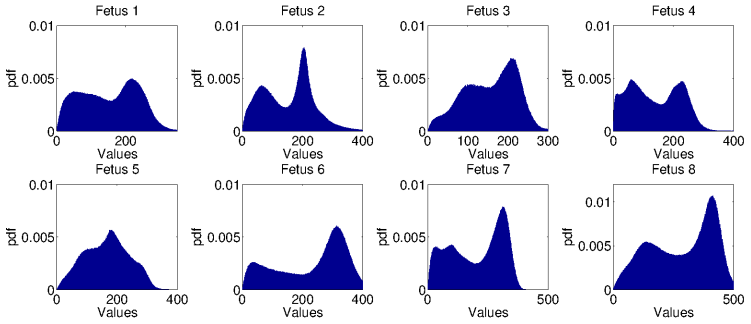

FIGURE 2.3: Probability density functions of the fMRI data for each of the 8 subjects before bias field correction is applied.

Voxels classified as having high intensities are used to fit a model for the bias field. Due to the low resolution, the data are strongly affected by partial volume effects that can influence the estimation of the bias field. Partial volume voxels are on the boundary between the two classes, and are therefore removed from the estimation using an erosion operation on the high-intensity class.

Let $\mathbf{x}_i$ denote locations of acquired voxels and $u_j(\mathbf{x}_i)$ their intensities in the j^{th} frame. Let s_{ij} be a segmentation of the high-intensity class, such that it is one if the voxels belong to this class and zero otherwise. Let $u_j^*(\mathbf{x}_i) = u_j(\mathbf{x}_i)e^{-b(\mathbf{x}_i)}$ denote the bias corrected intensities (in this formulation the absolute value of the bias field is modelled as $B_1^-(\mathbf{x}_i) = e^{b(\mathbf{x}_i)}$ and therefore its estimation is equivalent to the estimation of b).

Similarly to work presented by Wells III et al. [1996] and Kuklisova-Murgasova et al. [2013], we estimate the bias field by fitting a non-parametric regularized field. Specifically, the estimation of b is performed by minimizing the following cost function:

$$b = \underset{b}{argmin} \sum_{ij} s_{ij}(u_j(\mathbf{x}_i)e^{-b(\mathbf{x}_i)} - \mu)^2 + R(b) \tag{2.1}$$

where μ is the mean intensity of the fMRI voxels and $R(b)$ a regularisation term that ensures spatial smoothness of b.

To minimize 2.1 an iterative strategy is adopted; the estimation of b at a generic iteration n is interleaved with the calculation of the mean intensity

$$\mu^n = \frac{\sum_{ij} s_{ij}(u_j^*(\mathbf{x}_i))^n}{\sum_{ij} s_{ij}} \tag{2.2}$$

which serves as the estimated mean of the bias free intensities. b can therefore be estimated by comparing the corrected acquired intensities to this value. At each iteration we calculate the bias residuals $r_j^n(\mathbf{x}_i) = \log((u_j^*(\mathbf{x}_i))^n/\mu^n)$. This is followed by weighted spatial (3D) Gaussian smoothing of the residuals $r_j^n(\mathbf{x}_i)$ in each time-frame with weights $w_{ij}^n = (u_j^*(\mathbf{x}_i))^n s_{ij}$ and averaging in time to calculate the residual $\triangle b^n(\mathbf{x}_i)$ still present at the n^{th} iteration

$$\triangle\, b^n(\mathbf{x}_i) = \frac{1}{N_F} \sum_j \frac{\sum_l w_{lj}^n \phi_{\sigma_b}(d_{il}) r_j^n(\mathbf{x}_l)}{\sum_l w_{lj}^n \phi_{\sigma_b}(d_{il})} \tag{2.3}$$

where d_{il} represents the euclidean distance between voxels i and l, ϕ_{σ_b} is a Gaussian kernel with standard deviation σ_b for the smoothness of b, and N_F is the number of time-frames. The bias-corrected image is then updated as follows: $(u_j^*(\mathbf{x}_i))^{n+1} = (u_j^*(\mathbf{x}_i))^n e^{-\triangle b^n(\mathbf{x}_i)}$.

2.2.1.4 Slice to Volume Registration for fetal fMRI data

The readout duration of an EPI sequence is less than 100 ms and we did not observe signal degradation that could be directly attributed to intra-slice motion artefacts in our data. We investigate this aspect is section 2.2.2.4.

Inter-slice motion is, however, commonly present and can be many millimeters or even several centimeters on the timescale of the full fMRI time series. In this work performed at 1.5T, we have so far not accounted for image distortions and so have applied a rigid body motion model for the correction of each slice.

Motion correction methods seek a geometrical transformation of the data to place it in a self consistent coordinate system in which the fetal brain appears to be stationary [Jiang et al., 2007, Kuklisova-Murgasova et al., 2012, Rousseau et al., 2006]. Here we used the approach developed by Jiang et al. [2007], in which a hierarchical registration pipeline was built and successfully applied to reconstruct anatomical T_2 weighed fetal brains with high SNR levels.

The processing pipeline is organized as follows (see Figure 2.4). As a first step, complete stacks of slices (fMRI time series plus coronal and sagittal volumes) are registered and a reference image is formed by averaging the entire dataset. Data is then divided into temporally contiguous blocks (in Figure 2.4 each block is color coded), containing fewer slices. Rigid body registration to the reference is then performed, and the reference image is subsequently updated. This process is repeated, with progressively smaller temporal groupings, stopping when each block contains one slice. The last iteration of the algorithm corresponds to direct slice to volume registration. The cost function minimized by the algorithm is sum

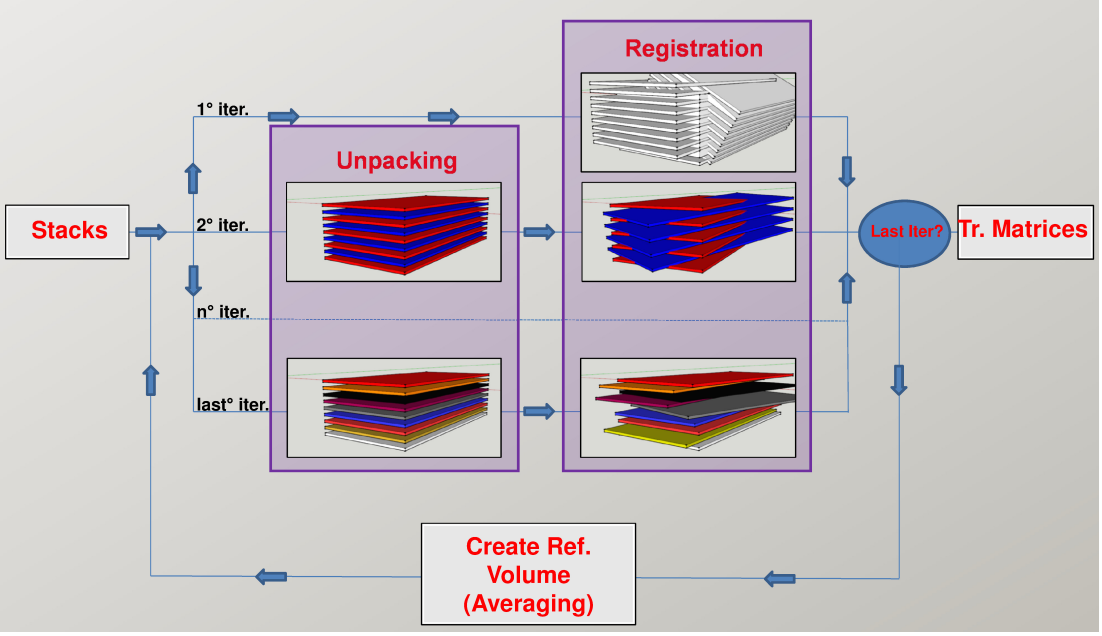

FIGURE 2.4: Motion correction Pipeline. Here each temporal block is color-coded and it represents the temporal unpacking of the data acquired during an interleaved acquisition.

of squares difference (SSD).

This process results in a set of rigid transformations that map all the slices from the fixed (i.e. stationary) Scanner coordinate system $\mathbf{S}_1$ into the moving fetal brain reference system $\mathbf{S}_2$. Using a single cumulative strictly positive index k to label each slice acquired during the whole fMRI time series we write:

$$\mathbf{S}_{2,k} = \mathbf{T}_k \mathbf{S}_1 \tag{2.4}$$

where $\mathbf{T}_k$ is a 6 degrees of freedom transformation applied to the k^{th} slice which was acquired at absolute time $(k-1)\,T_S$. In this formulation the first slice is assumed to be acquired at time zero.

2.2.1.5 Spin History correction for fetal fMRI data

In fetal fMRI imaging, spin history artefacts will appear as a natural consequence of motion, where successive slices acquired in the same Scanner coordinate system are effectively sampling the fetal brain at different anatomical positions. Changes of the baby's position will disrupt the steady state of the longitudinal magnetization, and each measure is then affected by an unknown scaling factor [Bhagalia and Kim, 2008].

If we model the RF pulse with a slice profile function ϕ, equation 1.17 modifies as follows:

$$\begin{cases} M_L^k(\mathbf{x}) = [M_0 - (M_0 - M_L^{k-1}(\mathbf{x})) \cdot e^{-\frac{T_S}{T_1}}] \cos[\alpha \cdot \phi(|\mathbf{x} - \mathbf{x}_{slice_k}|)] \\ M_T^k(\mathbf{x}) = [M_0 - (M_0 - M_L^{k-1}(\mathbf{x})) \cdot e^{-\frac{T_S}{T_1}}] \sin[\alpha \cdot \phi(|\mathbf{x} - \mathbf{x}_{slice_k}|)] \end{cases} \tag{2.5}$$

Here, $\mathbf{x}$ represents a generic position in $\mathbf{S}_1$ and $\mathbf{x}_{slice_k}$ its perpendicular projection onto the centerline of slice k. $M_0 = 1$ is the normalized longitudinal magnetization

at equilibrium, T_1 the longitudinal relaxation time and $\alpha = 90^o$ is the nominal flip angle used at acquisition. In this work, ϕ is approximated as a Gaussian function of FWHM of 5 mm such that $\phi(0) = 1$, and T_1 set at a typical value for neonatal brain of 1500 ms [Williams et al., 2005]. The model steps through time units of T_S, updating the current state of magnetization ($M_L^k(\mathbf{x})$ and $M_T^k(\mathbf{x})$) using the longitudinal magnetization computed at the previous iteration ($M_L^{k-1}(\mathbf{x})$). As initial conditions, the longitudinal and transverse magnetization components $M_L^0(\mathbf{x})$ and $M_T^0(\mathbf{x})$ were set to M_0 and 0 respectively.

Assuming that slice to volume registration provides the correct transformation matrices to map slices from $\mathbf{S}_1$ into $\mathbf{S}_2$, the equations for the longitudinal and transverse magnetization components in the presence of motion become:

$$\begin{cases} M_L^k(\mathbf{y}_k) = [M_0 - (M_0 - M_L^{k-1}(\mathbf{y}_{k-1})) \cdot e^{-\frac{T_S}{T_1}}] \cos[\alpha \cdot \phi(|\mathbf{y}_k - \mathbf{y}_{slice_k}|)] \\ M_T^k(\mathbf{y}_k) = [M_0 - (M_0 - M_L^{k-1}(\mathbf{y}_{k-1})) \cdot e^{-\frac{T_S}{T_1}}] \sin[\alpha \cdot \phi(|\mathbf{y}_k - \mathbf{y}_{slice_k}|)] \end{cases} \tag{2.6}$$

where $\mathbf{y}_k = \mathbf{T}_k\mathbf{x}$ and $\mathbf{y}_{slice_k} = \mathbf{T}_k\mathbf{x}_{slice_k}$.

Comparing equations 2.5 and 2.6 provide an intuitive representation on how spin history artefacts affect fMRI data. In the presence of strong motion, the magnetization never reaches the steady state value of equation 1.19, since the fetal brain is subjected to irregular temporal sampling. This is ultimately caused by slices being irregularly distributed in the $\mathbf{S}_2$ space.

We run both equations 2.5 and 2.6 on a 1 mm isotropic grid, obtaining a high resolution estimate of the magnetization components for each subject for each slice both with and without the estimates of motion. Each simulation took 2-3 hours using Matlab.

Since spin history corrections are applied directly to the original moving data (defined in $\mathbf{S}_1$ at the original coarse resolution), in the case of no motion, all the samples within each voxel $\mathbf{x}_i$ in $\mathbf{S}_1$ of sizes $2.5 \cdot 2.5 \cdot 5$ mm^3 (in-plane resolution

versus slice thickness) were averaged. For equation 2.6, all voxels at the fine resolution scale that were falling into $\mathbf{y}_{i,k}$ (projection of $\mathbf{x}_i$ into $\mathbf{S}_{2,k}$) were also averaged, and stored the resulting value at the original location in $\mathbf{S}_1$.

This produced two estimates of the transverse magnetizations, labelled respectively $M_T^{j,A}(\mathbf{x}_i)$ and $M_T^{j,B}(\mathbf{x}_i)$, defined for each frame j, at the original coarse resolution relative to the Scanner coordinate system $\mathbf{S}_1$. The labels B and A stand for the transverse magnetization components that are obtained when the presence of motion is and is not simulated.

To remove the variable saturation effects caused by intra-slice motion, each bias corrected fMRI voxel $u_j^*(\mathbf{x}_i)$ was weighted using the following formula:

$$u_j^{**}(\mathbf{x}_i) = u_j^*(\mathbf{x}_i)\frac{M_T^{j,A}(\mathbf{x}_i)}{M_T^{j,B}(\mathbf{x}_i)} \tag{2.7}$$

with $u_j^{**}(\mathbf{x}_i)$ representing the bias-spin corrected voxel acquired within the j^{th} frame at location $\mathbf{x}_i$.

2.2.1.6 Scattered Data Interpolation

The transformations determined by image registration provide a direct means of transforming from the original slice positions in $\mathbf{S}_1$ to the corresponding positions in $\mathbf{S}_2$. The slice data are irregularly positioned in $\mathbf{S}_2$ and need to be interpolated onto a uniform grid for further fMRI analysis. This is a key part of the pipeline where data can be degraded so we tested four different scattered data interpolation schemes, utilising both spatial and temporal proximity in different ways. Each method performs either locally linear interpolation based on Delaunay triangulation [Delaunay et al., 1934] or Shepard interpolation [Shepard, 1968].

Although complete stacks of fMRI slices are repeatedly acquired, each individual slice is a single-shot, which results in systematic timing offsets for each slice in

Scanner coordinates (in steps of T_S). Also, temporally adjacent slices do not necessarily have to be spatially adjacent, as slice time ordering can be chosen by the operator. There are thus two clear options; to regard the data as scattered in a 3D space, grouped into coarse time bins of duration T_R (stack repeat time), or to treat all the data as 4D space-time observations in which the distance between locations depends on both the spatial and temporal separation. Since all dimensions should have the same units, to create a distance metric, we scaled the time dimension by $\frac{res(z)}{T_R}$, where $res(z)$ is the resolution of the image in the through slice direction. We empirically observe that this scaling provides better results as opposed to $\frac{res(z)}{T_S}$.

Delaunay Linear interpolation: the Delaunay triangulation constructs a mesh by connecting nearest neighbours with straight edges. In 2D this results in a mesh of triangles, in 3D a mesh of tetrahedrons and so on. A Delaunay mesh is a tessellation such that the circumspheres associated with each simplex do not contain any other vertices in their interior. As a consequence of that, the Delaunay tessellation ensures that vertices belonging to the same simplex are also nearest neighbours. This property of the Delaunay mesh renders it particularly suitable for efficient scattered data interpolation, providing a means to estimate a value at a specific location from values in the local neighbourhood [De Berg et al., 2008]. In this case we used piece-wise linear interpolation from the vertices for each simplex that contains the target point.

Shepard interpolation: the second method considered, Shepard interpolation, uses a larger region of support, but ensures a continuous first derivative of the interpolation function. In this approach, the interpolated value $u(\mathbf{y})$ at a generic position $\mathbf{y}$ is estimated as a weighted sum of the values at the P nearest neighbours where the weights are a decreasing function of a metric of distance. Specifically:

$$u(\mathbf{y}) = \sum_{p=0}^{P} \frac{w(\mathbf{y}, \mathbf{y}_p) u(\mathbf{y}_p)}{\sum_{q=1}^{P} w(\mathbf{y}, \mathbf{y}_q)} \tag{2.8}$$

where $u(\mathbf{y}_p)$ is the p^{th} closest available value to the point to infer, and $w(\mathbf{y}, \mathbf{y}_p)$ the associated weight. We chose $w(\mathbf{y}, \mathbf{y}_p)$ to be $\frac{1}{d^2(\mathbf{y}, \mathbf{y}_p)}$, with $d(\mathbf{y}, \mathbf{y}_p)$ being the euclidean distance between $\mathbf{y}$ and $\mathbf{y}_p$. Squaring $d(\mathbf{y}, \mathbf{y}_p)$ ensures that the reconstructed function is continuous for $\mathbf{y} \to \mathbf{y}_p$ [Gordon and Wixom, 1978].

2.2.1.7 Validation of interpolation methods

A forward simulation was used to validate the interpolation schemes. In the first step, a synthetic dataset was constructed by taking a fetal head mask and defining a set of five spatial regions, color coded in Figure 2.5. Each mask was spatially smoothed to avoid ringing effects when resampling. A specific synthetic time course was assigned to each of these regions as follows: $s_1(t) = \sin(2\pi \cdot 0.05 \cdot t)$, $s_2(t) = \cos(2\pi \cdot 0.01 \cdot t)$, $s_3(t) = \text{sawtooth}(2\pi \cdot 0.02 \cdot t)$, $s_4(t) = \text{repbox}(2\pi \cdot 0.03 \cdot t)$, $s_5(t) = \sin(2\pi \cdot 0.08 \cdot t)$, with sawtooth and repbox representing a train of repeated sawtooth and boxcar functions respectively. A global mean of 500 units was assigned to the entire volume mask.

The simulation was set up at the time scale of T_S. To match the temporal structure of real data acquisition, a $T_R = 4$ *sec* and a total number of 35 slices for each stack were used. The spatial resolution of the simulated data was 1 *mm* isotropic.

The first step was to model the sampling of the object that the scanner performs. Initially, the transformations between $\mathbf{S}_1$ and $\mathbf{S}_2$ were set to identity, so that the object was stationary in $\mathbf{S}_1$. The simulated slice data consisted of voxels $\mathbf{x}_i$ in $\mathbf{S}_1$ of size of $2.5 \cdot 2.5 \cdot 5$ mm^3 (in-plane resolution versus slice thickness). The simulated 'acquired' signals were calculated as the mean of the values from all the voxels in the high-resolution model that fall within $\mathbf{x}_i$. In order to investigate possible effects of different slice overlaps on the final result, complete simulations were run with overlaps of 1 *mm* and 2.5 *mm*, which correspond to the minimum

FIGURE 2.5: Spatial distribution of the five regions used in the forward simulation.

and maximum amount of overlap in the real data. Acquisition slice ordering was interleaved (1-3-5-7...2-4-6-8...) and the acquisition of 100 volumes was simulated.

After simulated acquisition, Gaussian noise was added to each voxel. The variance of the noise was selected to provide a low BOLD effect-to-noise ratio, typical of RSNs, where the explained variance in adult studies is around 2 or 3%. The simulated data were then analyzed using Probabilistic ICA as implemented in FSL Melodic (http://fsl.fmrib.ox.ac.uk/fsl/fslwiki/) to determine if the temporal-spatial patterns built into the model could be detected.

Before running Probabilistic ICA, data were spatially smoothed with a Gaussian Kernel of FWHM of 2 mm.

Motion was then simulated by applying to each slice in $\mathbf{S}_1$ the set of rigid transformations observed in the subject in our study population that exhibited the largest level of movement. Each 'acquired' voxel, $\mathbf{x}_i$, in $\mathbf{S}_1$ was therefore projected into $\mathbf{S}_{2,k}$, obtaining its projected version $\mathbf{y}_{i,k}$. The signal for each position in $\mathbf{S}_1$ was then assigned to the average of the voxel values at the fine resolution that were within $\mathbf{y}_{i,k}$. Independent Gaussian noise with the same variance as before was then added to the signal for each acquired voxel in the moving object in $\mathbf{S}_1$.

Finally, to test each interpolation scheme, the simulated acquired (noisy) slice data in $\mathbf{S}_1$ was projected back into $\mathbf{S}_2$ to produce scattered data ready for analysis. Regular spaced data was then recovered using each of the interpolation schemes outlined in section 2.2.1.6 and 'Resting State Networks' identified using standard Probabilistic ICA, after smoothing with Gaussian Kernel of 2 mm.

2.2.1.8 Group Independent Component Analysis

Group Probabilistic ICA was used to discover Resting State Networks at the population level from the fetal data after correcting for bias field, spin history and motion. Brain extraction was performed on each subject using a manually delineated fetal brain mask.

The data from all subjects were placed into a common space defined by selecting a fetal T_2 weighted atlas of 32 weeks of gestation (the mean gestational age of the group). The atlas was created from separate data according to the method described by Serag et al. [2012]. The required registrations were carried out in two separate steps; first, for each subject separately, the fMRI data were rigidly registered to their corresponding T_2 weighted brain volume produced from the ssFSE images that had been realigned and reconstructed as described in Jiang et al. [2007]. The T_2 weighted volume reconstructions were aligned to the common target space using affine registration. The individual reconstructed fetal brain volumes achieve self-consistency, but may appear in an arbitrary pose. It was therefore frequently necessary to supply a starting transformation estimate. The transformations obtained by the two registration processes were composed and applied to fetal fMRI data in a single step. Finally, each dataset was spatially smoothed with a Gaussian Kernel of 2 mm.

2.2.2 Results

The following sections first report the results obtained on the synthetic dataset, and then those obtained from *in vivo* data.

2.2.2.1 Scattered Data Interpolation

Figure 2.6 shows the components recovered by Probabilistic ICA for the 1 *mm* and 2.5 *mm* overlap cases, when no motion is included in the simulation ($\mathbf{S}_1 = \mathbf{S}_2$). The Figure shows z-score maps thresholded using the cut-off value given by FSL Melodic. When running ICA the number of components was automatically estimated correctly to be five. As expected, in both cases, ICA is capable of recovering spatial-temporal patterns, that, if compared with Figure 2.5, demonstrate a good level of overlap.

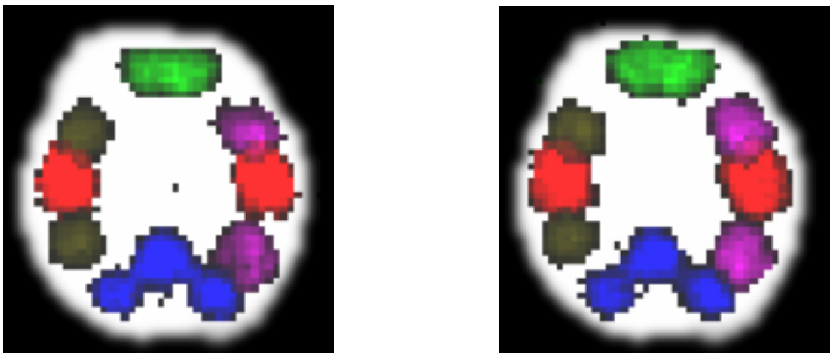

(A) Overlap of 1 *mm*. (B) Overlap of 2.5 *mm*.

FIGURE 2.6: Components recovered by ICA for the two different levels of overlap.

Running ICA on the moving object *without* motion correction does still partially recover some signal for the 5 components, but with substantial damage (Figure 2.7).

Figure 2.8 shows the recovered components obtained on the motion corrected objects after having performed scattered interpolation. Each column shows a

FIGURE 2.7: Spatial distribution of the 5 components in the simulated moving dataset when motion is not corrected. Here we are showing the result with slice overlap of 1 mm.

different method of interpolation: Delaunay 3D, Delaunay 4D, Shephard 3D, and Shephard 4D. Rows show recovered maps for the two different level of overlap. In all cases, we are able to recover the introduced components, with no substantial differences between the two levels of overlap.

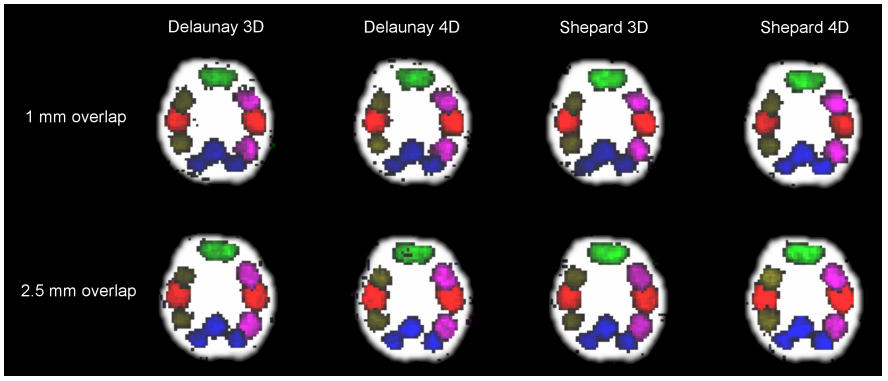

FIGURE 2.8: Spatial distribution of the 5 components for the 4 different scattered interpolation methods and for the two different overlaps each of which is corrected for motion.

To evaluate the performances of the two different scattered interpolation schemes, we calculated the normalized root mean square error (NRMSE) between the motion free dataset (obtained when $\mathbf{S}_1 = \mathbf{S}_2$) and motion corrected ones. The calculation was carried out on all noise free datasets and the NRMSE (in %) is shown in Figure 2.9.

Based on a visual inspection and the NRMSE results, the Delaunay 3D method appears to perform best for the problem in question, and we subsequently decided to apply this method to *in vivo* data.

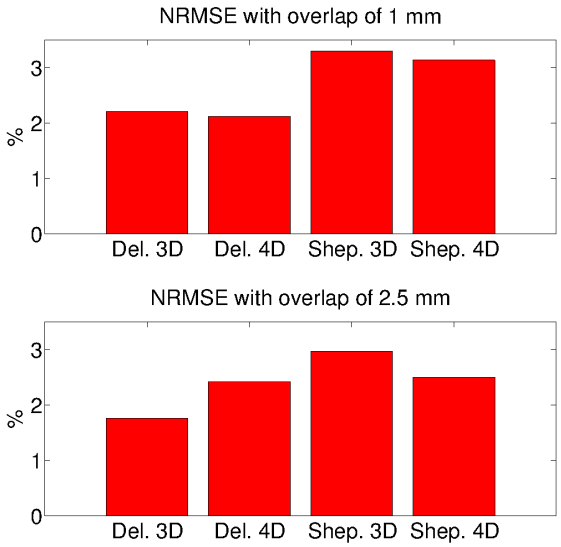

FIGURE 2.9: NRMSE for all scattered interpolation methods and for the two levels of overlap.

The choice of Delaunay interpolation over previously proposed multilevel B-splines scattered data interpolation [Jiang et al., 2007] and super-resolution reconstruction approaches [Kuklisova-Murgasova et al., 2012] is due to the following reason; while reconstruction of anatomical T_2 weighted images can exploit an oversampling factor that comes naturally by imaging the fetal brain multiple times for multiple views, in the context of fetal fMRI what is really desired is the reconstruction of time series. The consequence of this is that the natural rate of scattered positions versus points to infer is 1 to 1. This relationship may also get worse when big motion occurs, by opening up holes between slices that are spatially adjacent.

B-splines can be unreliable in this type of application because of isotropic kernels and an inability to fill areas with missing data. Furthermore super resolution approaches are suitable when oversampling in the data can be used to improve

its resolution. In fetal fMRI data there is no oversampling and therefore their usage is very undesirable.

2.2.2.2 Bias Field Correction

Figure 2.10 shows a slice in the transverse plane before (A) and after (B) bias correction for one of the subjects that presented with strong bias effects. The red arrow in (A) highlights a region in the brain affected by strong bias. In (B), the shading given by the inhomogeneities of $\mathbf{B}_1^-$ is largely resolved. The estimated bias field is shown in Figure 2.10 (C); its application results in much more homogeneous image properties, although this is hard to quantify in the absence of a ground truth estimate.

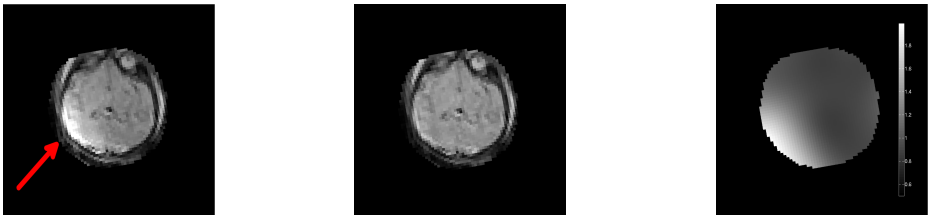

(A) Original Image. (B) Corrected Image. (C) Bias field.

FIGURE 2.10: Bias field correction results. An EPI slice (A) before and (B) after bias field correction using the bias field shown in (C). The red arrow highlights a region in the brain affected by strong bias.

Means and standard deviations for the estimated bias fields for all subjects over the region of interest were 1.024 ± 0.138, 1.036 ± 0.223, 0.994 ± 0.106, 1.005 ± 0.120, 0.932 ± 0.154, 1.002 ± 0.069, 0.993 ± 0.049 and 1.007 ± 0.078.

We have finally performed an exhaustive simulation on the data from this study to measure the performances of our bias correction algorithm. Having corrected every subject, we applied all the resulting bias field estimates to the corrected images of every other subject. Each bias field was projected and interpolated onto the space defined by the fetal head and the bias field applied to each image

independently. We therefore obtained a set of 56 examples, each of which was characterized by a different subject-bias field combination.

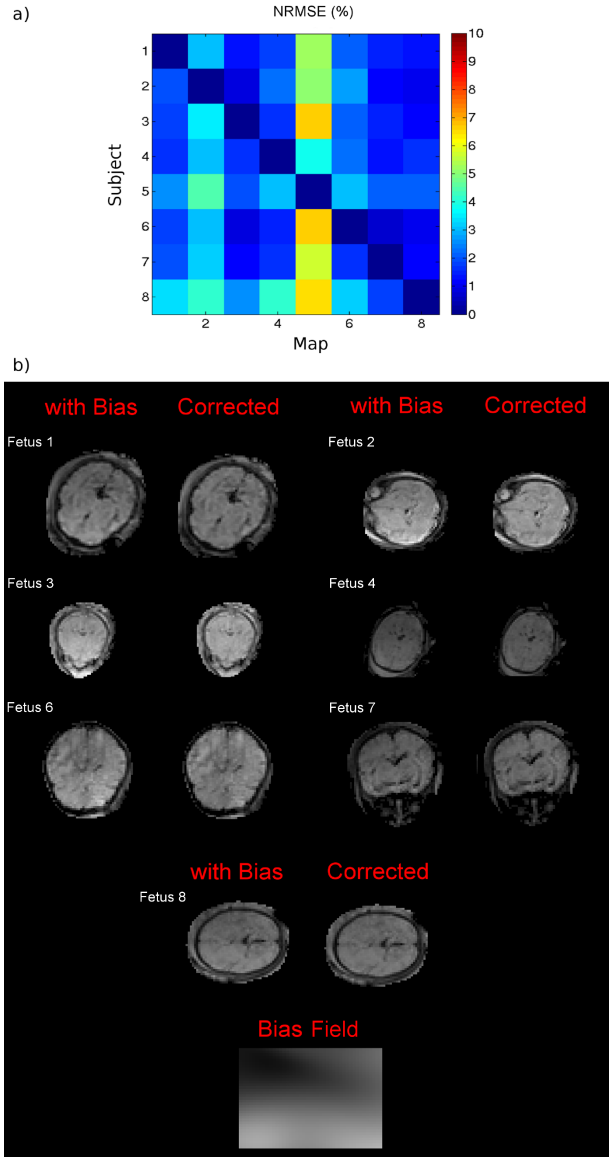

FIGURE 2.11: (a) NRMSE between estimated bias and ground truth in the permutation test. (b) Comparison between the 7 subjects corrupted with bias field number 5 and the corresponding bias corrected images.

The bias correction algorithm was then run on this set of 56 images, and the performances measured by calculating the NRMSE between the estimated and original bias fields. This led to the Table reported in Figure 2.11, where each row represents a subject, and each column the associated bias field. The NRMSE

was 1-2% for the majority of the cases, reaching peaks of 5-6% when using the bias field from subject number 5 (fifth column). Despite this bigger error, we observed good results even in this case; the bottom part of same Figure reports images before and after bias field correction using this $\mathbf{B}_1^-$ map, and shows a substantial reduction of inhomogeneities in all cases.

2.2.2.3 Slice to Volume Registration

In order to assess the registration performances, we used a forward simulation. We chose from our cohort of registered subjects the one that exhibited the highest level of motion (fetus number one from Table 2.1) and selected one volume with no substantial motion artefacts as reference. The entire volume was then projected into the space of acquisition by using the transformation matrices that had been previously computed when registering the original data. The signal coming from the projected volumes was then interpolated onto the space defined by each slice using B-splines [Lee et al., 1997]. The use of B-Splines is here convenient as the scattered space formed by the projected volumes is regular. Isotropic noise was finally added to each voxel to reach typical levels of SNR.

The synthetic moving dataset was then fed into the registration framework and the estimated motion parameters compared with the ground truth. Means and standard deviations of the absolute error were 0.047 ± 0.066 mm, 0.039 ± 0.075 mm, 0.066 ± 0.096 mm for translations, and $0.194 \pm 0.147°$, $0.174 \pm 0.130°$, $0.122 \pm 0.122°$ for rotations.

Table 2.2 summarizes motion of all the corrected subjects showing that there was substantial translation and especially rotation. The grey row of the Table reports the means and standard deviations of the motion parameters obtained from one of the three subjects for which the registration algorithm failed, whereas the blue one refers to one of those subjects that exceeded the field of view.

In the case of excessive motion, the registration procedure reduced the observable motion substantially, but residual movement was still clearly seen and at some time points the interpolated volumes were obviously damaged. The motion estimates, although incorrect, do give an indication of the magnitude of the motion exhibited, which was higher than all the other subjects in most motion parameters.

Figure 2.12 shows the estimated motion parameters plotted against the acquired volume index for subject number one. Parameters are arranged according to the slice acquisition order. The translations are comparable in magnitude with the dimensions of each voxel. Estimated rotations take values within the range $-20°$ and $+10°$ around the x and y axes, reaching a peak of $-60°$ for rotations around the z axis. To illustrate the accuracy of the registration algorithm, we focus on the red segment of Figure 2.12, which corresponds to volumes 23 and 24 in the original data and coincides to the period in which fetus one moved the most.

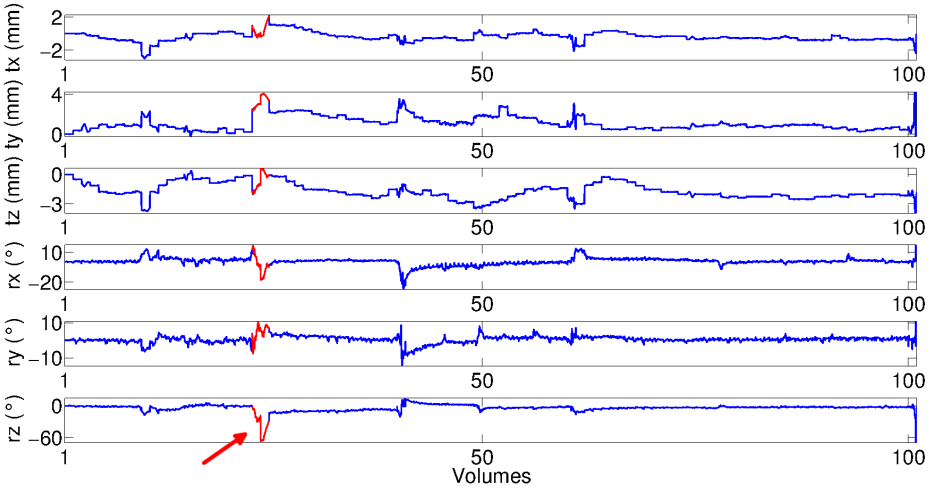

FIGURE 2.12: Behaviour of the estimated motion parameters. The red segments of the curves (indicated also by the red arrow) will serve as illustration of the performances of the registration later on.

Figure 2.13 (a) shows an 8 second period of the time course. The same motion estimates, but rearranged in geometrical slice order, are shown in Figure 2.13 (b). The oscillating nature of the reconstructed motion parameters in (b) derives

	Translation			Rotation		
Fetus	tx (*mm*)	ty (*mm*)	tz(*mm*)	rx (°)	ry (°)	rz(°)
1	-0.37 ± 0.55	1.10 ± 0.72	-1.69 ± 0.82	0.56 ± 3.72	0.48 ± 2.15	-4.41 ± 7.21
2	-0.41 ± 1.09	-1.03 ± 1.07	-0.48 ± 0.52	1.52 ± 3.32	-0.93 ± 4.03	2.09 ± 2.64
3	0.69 ± 0.61	-1.37 ± 1.10	1.36 ± 1.13	2.13 ± 1.90	1.01 ± 1.50	0.75 ± 1.30
4	0.98 ± 0.62	-2.86 ± 1.30	2.94 ± 1.97	4.18 ± 3.40	3.40 ± 1.91	-0.78 ± 1.47
5	1.66 ± 1.70	0.16 ± 0.64	0.42 ± 1.19	-0.28 ± 2.27	2.94 ± 5.98	1.18 ± 5.49
6	0.04 ± 0.59	0.69 ± 1.33	0.35 ± 0.76	0.87 ± 2.13	0.97 ± 3.12	-1.84 ± 4.00
7	-0.25 ± 0.89	0.98 ± 1.27	0.96 ± 0.96	-0.04 ± 3.46	0.25 ± 3.05	-0.79 ± 2.91
8	0.61 ± 1.12	-0.53 ± 0.88	0.59 ± 0.89	0.14 ± 2.07	-2.42 ± 3.59	1.37 ± 3.16
9	6.70 ± 4.00	-1.12 ± -1.79	-2.03 ± 2.57	13.53 ± 16.38	7.85 ± 9.28	8.59 ± 17.73
12	-0.79 ± 2.86	3.33 ± 2.97	0.04 ± 2.49	0.79 ± 5.27	-0.79 ± 4.66	-7.26 ± 9.57

TABLE 2.2: Mean and standard deviation of rigid body motion parameters for all the corrected subjects (1-8), for one of the fetuses for which the registration algorithm failed (9) and for one that exceed the field of view (12).

from the interleaved slice ordering used at acquisition. This oscillatory behaviour appears to decline at the edges of the stacks of slices in Figure 2.13 (b) (region shown in lighter blue), where the acquired slices are in fact outside the brain at its superior and inferior extremes. These slices cannot be aligned to the target reconstructed brain during the final slice-by-slice stages of registration process and so their parameters remain static after the registration with other slices that are inside the brain; the hierarchical strategy proposed by Jiang et al. [2007] initializes the registration of each sub-block of slices with an initial transformation computed when performing the registration of the corresponding parent block. Sudden jumps of the motion estimates in Figure 2.13 (b) between volumes 23 and 24 do not correspond to sudden movements, but are a natural effect of the registration framework.

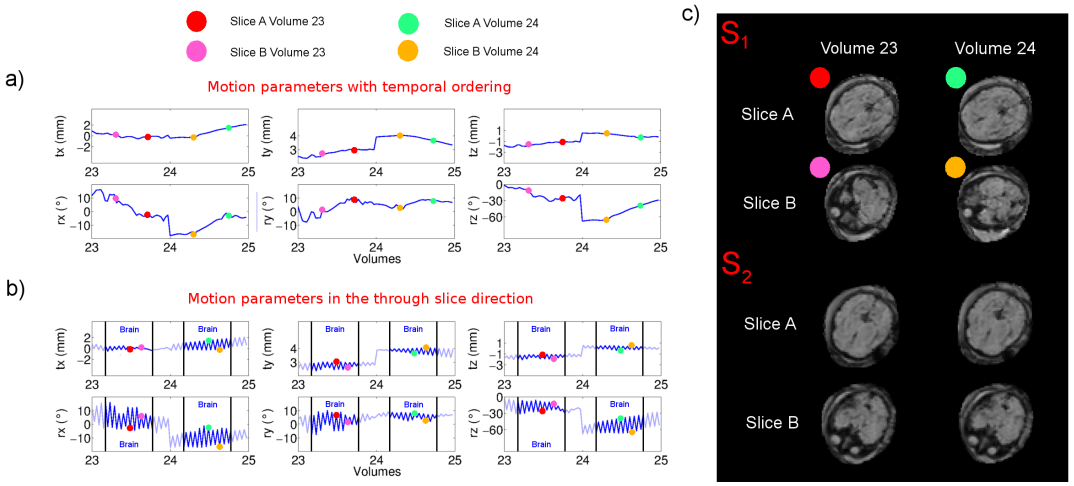

FIGURE 2.13: (a) Reconstructed motion parameters with temporal ordering for the red segment of Figure 2.12. (b) Motion parameters presented in geometrical slice order. Slices belonging to the brain are highlighted, those beyond the superior and inferior margins of the brain are in lighter blue. (c) Two slices taken from the 3D slice stack at volumes 23 and 24 before motion correction, i.e. in Scanner coordinates $\mathbf{S}_1$ (first two rows), and after motion correction, i.e. in Patient coordinates $\mathbf{S}_2$ (last two rows).

Figure 2.13 (c) (first two rows) shows slices taken at two different levels of the brain from volume stacks 23 and 24. The Figure provides a striking, but not untypical, illustration of how fetuses frequently change position, particularly by

rotation within the time taken to acquire a single complete stack. The lower half of Figure 2.13 (c) shows the same set of slice locations after motion correction. The corresponding motion estimates are also highlighted in Figure 2.13 with colored circles.

Finally, in order to be able to provide a measure of absolute motion for those examples in which the registration algorithm failed, the pupil of the left eye was chosen as a landmark, and its motion tracked by taking the distance of its position between the 2 volumes of the time series in which the motion excursion was maximal. The same calculation was repeated for subjects labelled 12 to 14 of Table 2.1, but for these cases the start and end frames were the first volume of the time series and the volume in which the fetus first moved partly outside the imaged region. The calculated absolute displacements were 55.2, 37.6 and 36.2 mm for subjects 9, 10 and 11, and of 36.5, 22.3 and 53.7 mm for subjects 12, 13 and 14.

2.2.2.4 Intra-Slice Motion Artefacts

In section 2.2.1.4 we observed that intra-slice motion artefacts in fetal fMRI data are small in comparison to other effects in our sample. To determine more systematically what the effects of intra-slice fetal motion are, the following simulation was performed. Using the registration data from the fetus who had shown most movement, translations and rotations that occurred between consecutively acquired slices were determined. Since the duration of the EPI readout ($T_{RO} = 58$ ms) is actually shorter than T_S, the total time interval between two excitations, each intra-slice motion estimate was scaled down by the factor $\frac{T_{RO}}{T_S}$. The absolute value of the intra-slice motion estimates was then averaged, providing an average total readout rotation Z_M around z of 0.1622°, and average translations X_M and Y_M along x and y of 0.0045 and 0.0038 mm (for simplicity here we have only considered in plane motion).

The fetal motion pattern was then assumed to have constant velocity throughout the readout. A test slice taken from the same subject was then moved in equal increments from $-\frac{X_M}{2}$ to $\frac{X_M}{2}$, from $-\frac{Y_M}{2}$ to $\frac{Y_M}{2}$ for translations along x and y, and from $-\frac{Z_M}{2}$ to $\frac{Z_M}{2}$ for rotations around z. For each configuration, the image was interpolated using B-splines and then Fourier transformed to the k-space domain, with the current readout sample extracted and stored. When all the readout segments for the EPI trajectory were assembled the now motion corrupted k-space data was back transformed to produce a final image with intra-slice effects embedded into it.

Direct voxel by voxel comparison between original and motion corrupted slices gave a maximum relative error that was always less than 0.1%, suggesting that intra-slice motion artefacts in fetal fMRI data tend to be small in comparison to the other effects that we have endeavoured to address.

2.2.2.5 Correction of Spin History Artefacts

Figure 2.14 shows the result of the application of equations 2.5 (a) and 2.6 (b), where, when used, motion parameters were the ones from subject number 3. The Figure shows a cut along the through slice direction for the longitudinal and transverse magnetizations (left and center plots), and the integrated signal over the current excited slice ($M_T^{j,A}(\mathbf{x}_i)$ of equation 2.7). When there is no motion, the signal is not modulated. However, signal variation appears as soon as slices are subjected to motion.

Figure 2.15 shows transverse, sagittal and coronal views of the transverse magnetization as predicted by the spin history model for subject number 3 (one volume). This has been converted into % signal change. Predicted signal change varies within a rage of roughly $\pm 10\%$ for the majority of the voxels.

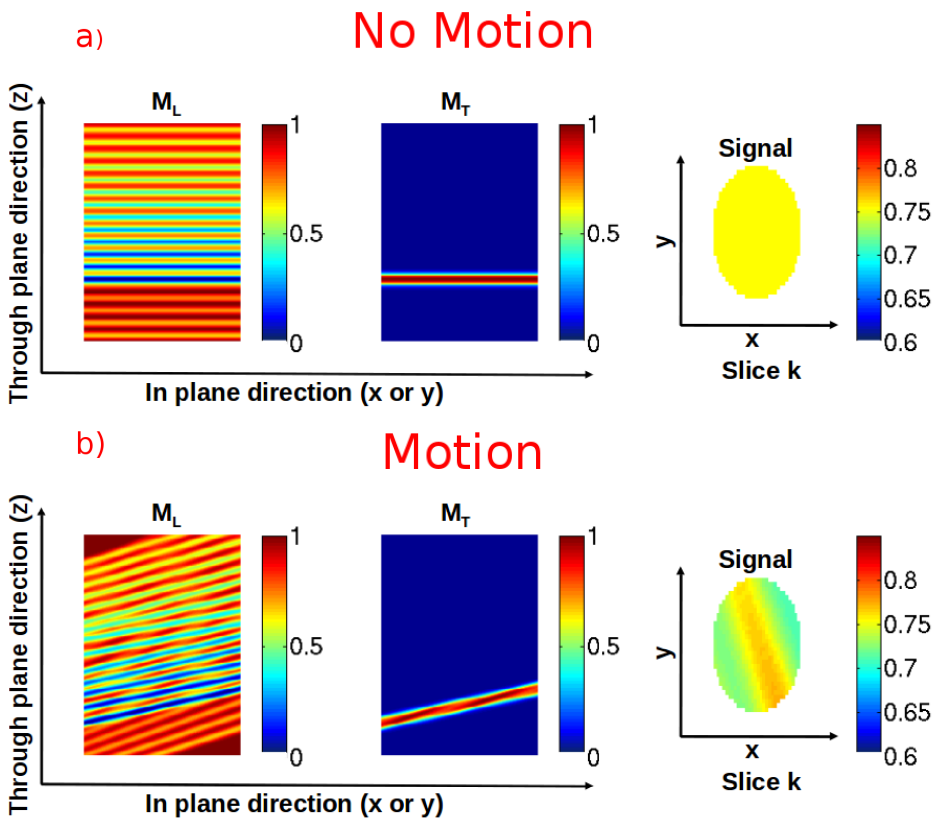

FIGURE 2.14: Longitudinal and transverse magnetization at the same representative time point in the absence/presence (a/b) of motion (left and center plots). Right plots: signal over the fetal head in both conditions.

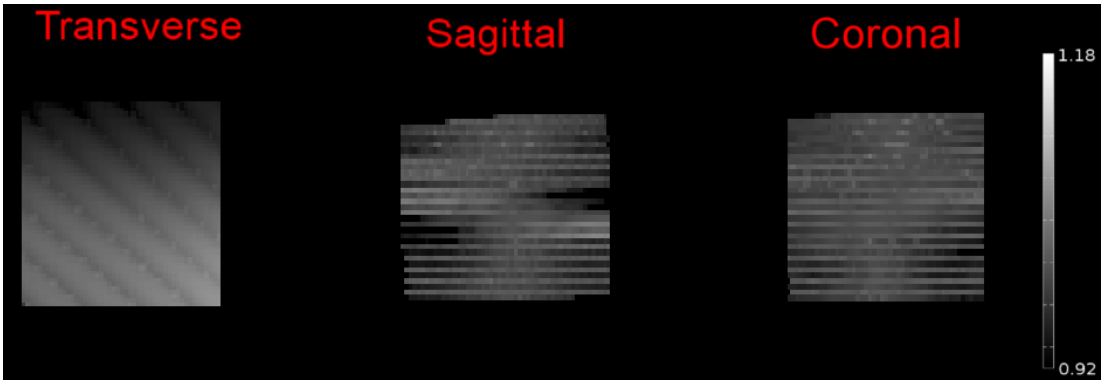

FIGURE 2.15: Transverse, Sagittal and Coronal views of the saturation factors as predicted by the spin history model.

2.2.2.6 Validation of the Spin History model

The transverse magnetization at a specific space-time location in functional imaging is proportional to the stored longitudinal magnetization that is available at that spatial location just prior to the application of the excitation RF pulse. If the spin history model is correct then we would expect correlation between the time courses of the observed fMRI data and the predicted saturation factors. Conversely, if the model did not predict these effects, the saturation factors would not relate to the data at all, so there would only be chance correlation.

We therefore calculated the cross correlation between the predicted time varying saturation factor (M_T^B) at each location in anatomical space ($\mathbf{S}_2$) and the recorded time series after motion correction. To do this, the saturation factors for each slice calculated in Scanner coordinates $\mathbf{S}_1$ were transformed into $\mathbf{S}_2$ and interpolated onto a regular grid. Figures 2.16 (a) shows the resulting correlation map for subject number one and suggests that the signal is generally correlated with the saturation time courses predicted by the model. Considering the subject group as a whole and taking the average correlation score across each brain shows mean values of -0.79% for the least correlated subject and 24.63% for the most correlated one.

To test the performance of the model, a permutation test was conducted on subject number one. The saturation time courses for each voxel predicted by the model were randomly assigned to another voxel position in $\mathbf{S}_2$. Correlation maps between the original fMRI data and this new configuration of saturation factors was then recalculated. The procedure was repeated 1000 times and the mean correlation score calculated each time. We then tested the null hypothesis that these 1000 correlation scores are a realization of a Gaussian distribution. This null hypothesis was accepted ($p > 0.05$).

Finally, in order to see whether the original configuration (i.e. without reshuffling) of the saturation factors is capable of describing sensible variations in the data,

we tested the hypothesis that its mean correlation score belongs to the Gaussian distribution computed in the previous step. This test had negative outcome as the mean correlation score was found to lie beyond 70 standard deviations from the center of the Gaussian distribution, confirming that the time saturation factors as given by the spin history model are correlated with the fMRI signals by more than chance and therefore justifying their removal.

To assess the sensitivity of the spin history model to changes of T_1, the estimation M_T^B was repeated using a $T_1 = 3000\ ms$ and the correlations with the fMRI data recalculated. Results for subject one are shown in Figure 2.16 (c), and confirm that the correlation score does not depend strongly upon the choice of T_1. However, a t-test under the null hypothesis of the results in Figures 2.16 (a) and (c) being realizations of Gaussian random variables with identical means and variances was rejected ($p < 0.05$), confirming that the choice of T_1 does influence the estimation of the saturation factor to be applied at each spatial-temporal voxel location in a detectable way.

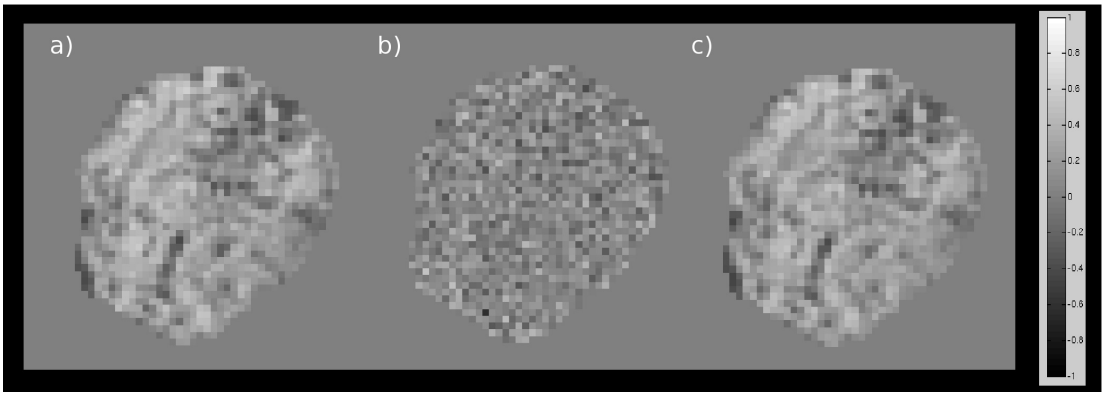

FIGURE 2.16: (a) Correlation score between M_T^B given by the model and the corresponding fMRI time series ($T_1 = 1500\ ms$). (b) Correlation score between the same fMRI data with saturation factors from the permutation test. (c) Correlation score between original data and model prediction using $T_1 = 3000\ ms$.

We also performed a last test where we imposed a temporal shift to the magnetization in multiples of T_R. Circular boundary conditions were used. The correlation between the original data and the shifted magnetization was subsequently

calculated.

We ran this on independent data so that to check the robustness of the method across different subjects. Average correlation for subject number 5 of Table 2.1 expressed as a function of this temporal shift is shown in Figure 2.17. When there is no lag, average correlation is maximal.

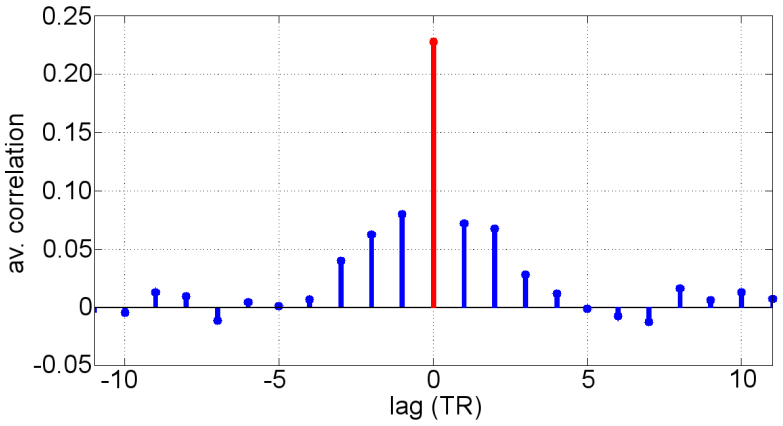

FIGURE 2.17: Average correlation between the data and shifted magnetizations as a function of the temporal lag (in steps of T_R).

Figure 2.18 shows the results obtained from subject number 5. In this case, 120 volumes had originally been acquired and they are all used here. The first row of the Figure shows the correlation map between the data and the saturation time courses. It can be observed how the signal is generally correlated to the model output. The second and third rows show, respectively, the predicted signal modulation and the original data for one voxel (indicated in Figure 2.18 by the green cursor). Both traces are expressed in % signal change.

By comparing the two time courses, it can be observed that 3 spiky events in the original data are predicted by the spin history model (red arrows). Furthermore, there is substantial correlation throughout. The dynamic range of the introduced modulation is however slightly different; this can be due to differences in T_1, model limitations, registration errors and other effects.

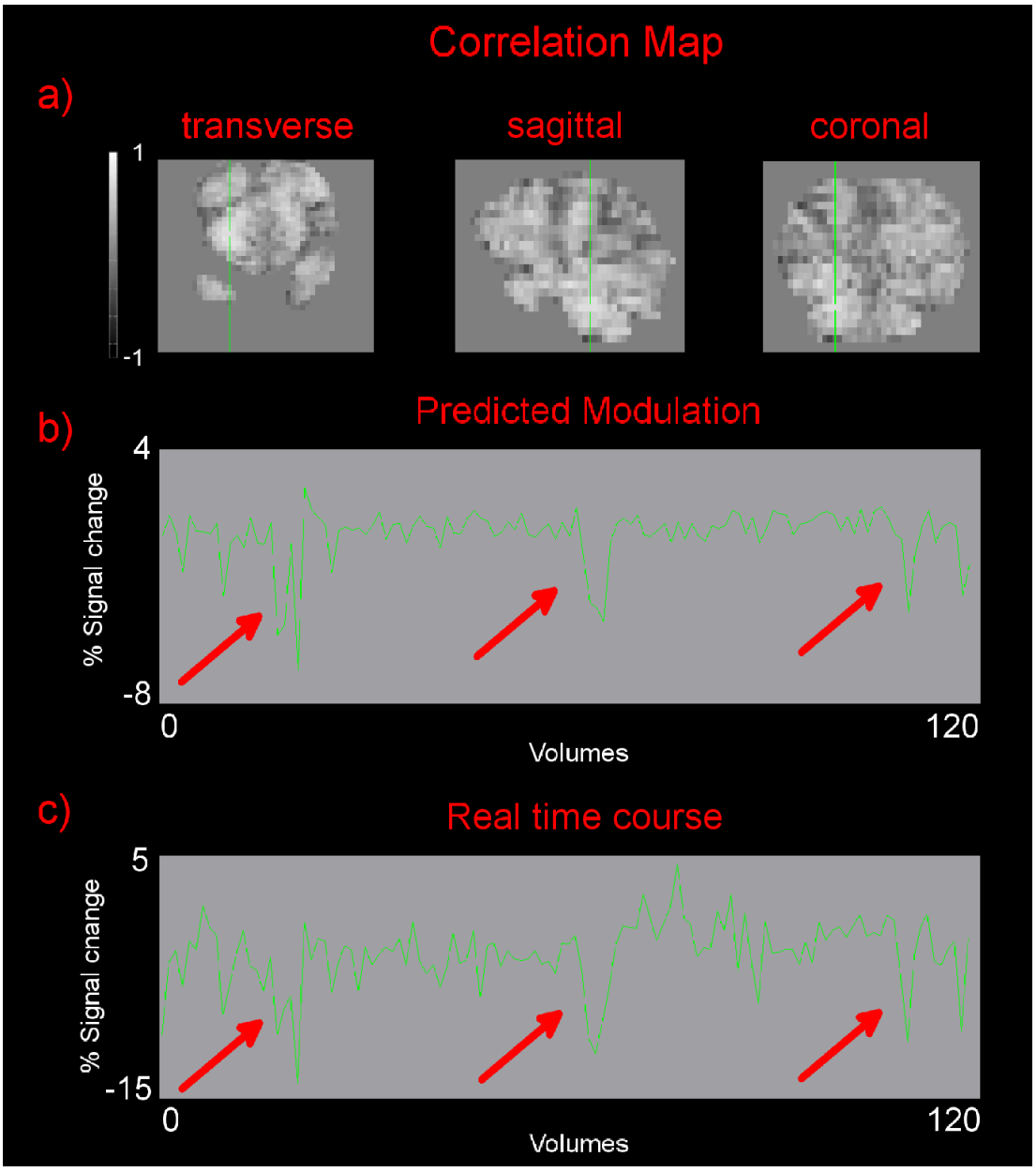

FIGURE 2.18: (a) Correlation map between saturation time courses and data for subject number 5. (b) Signal modulation (in %) as predicted by the model at the location highlighted in (a) by the green cursor. (c) fMRI data at the same location converted in % signal change.

2.2.2.7 Group Independent Component Analysis

Group ICA extracted 20 components, 6 of which (Figure 2.19) were identified as spatially resembling those previously described in preterm neonates by Smyser et al. [2010] and by Doria et al. [2010].

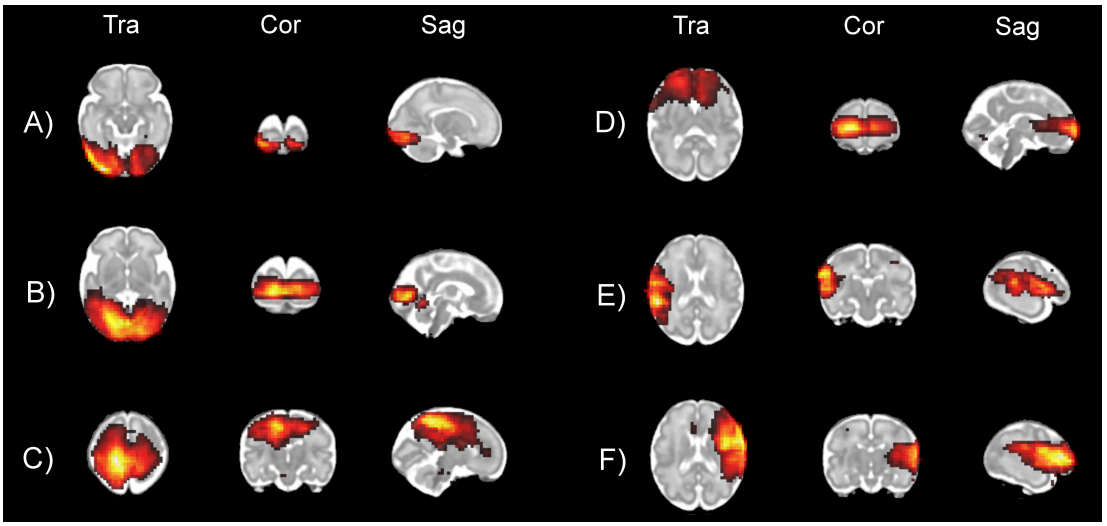

FIGURE 2.19: Transverse, coronal and sagittal views of RSNs given by Group ICA overlaid onto a fetal template of 32 weeks (all z-score maps were thresholded using the cut-off value given by Melodic). The left side of the Figure corresponds to the left side of the brain.

These consisted of: (A) lateral visual network encompassing the extra-striate visual areas; (B) a medial visual network comprising the striate and parastriate areas; (C) a bilateral sensori-motor network in the superior parietal lobe encompassing the primary motor and somatosensory cortices (anterior and posterior to the central sulcus respectively); (D) a primitive default mode network in the medial prefrontal and anterior cingulate cortices; (E) and (F) unilateral auditory networks in the superior temporal and insular areas in the left and right hemispheres respectively. In accordance with the findings of studies with preterm infants, a trend towards a more bilateral network representation (between one region and its homotopic counterpart) was seen in those encompassing medial areas (such as the sensori-motor and medial visual networks). In contrast, networks presumed to demonstrate more long-range connectivity in their mature forms (such as the auditory and default mode networks) were found to be unilateral or incomplete.

2.3 Fetal Resting State fMRI data at 3T

The next sections report the results obtained by gathering and analysing fetal resting state fMRI data at 3T. The methods can be considered as an extension of the work proposed so far. However, differences in the acquisition protocol and in the processing steps, coming from lessons learnt from the data acquired at 1.5T, have been adopted and will be described accurately in the next paragraphs. All other processing steps are the same.

2.3.1 Material and Methods

2.3.1.1 Acquisition

The data used in this study were from 32 fetuses (mean gestational age: 29.09 $\pm$ 4.25 weeks) who were scanned on a Philips Achieva 3T scanner with a 32 channel receiver coil using single shot EPI ($T_R = 2900\ ms$, $T_E = 50\ ms$, with an in-plane resolution of $2.5 \cdot 2.5\ mm^2$ and slice thickness of $3.5\ mm$). During each T_R interval, 29 slices were acquired using an ascending slice order. The flip angle was set to 70°, that corresponds to the Ernst angle calculated with T_1 and T_R of 2700 and 2900 ms. A SENSE factor of 2 was used for all EPI acquisitions, and 130 resting state fMRI volumes were acquired. There was no acquired data in sagittal and coronal directions.

A field map acquisition [Jezzard and Balaban, 1995] was added to the main fMRI protocol. The field map consisted of an axial set of slices covering a field of view of $320 \cdot 320 \cdot 100\ mm^3$. Resolution was $5 \cdot 5 \cdot 10\ mm^3$ and ΔT_E 2.3 ms.

A failure mode of the previous study was when the fetal head moved outside the field of view. Despite trying to enlarge the sampling volume to match the fetal brain size, this occurred in three cases in our sample. As increasing spatial coverage takes more time or requires less dense sampling in the slice direction, there

is a tension between reducing the risk of data loss through large-scale changes in position and other key factors.

Data loss needs to be avoided by all means and we make the following considerations; the field of view along the third dimension is influenced by the slice thickness, the number of acquired slices and a possible overlap/gap between them. Also, the total number of slices determines the minimum T_R and therefore its choice is a critical factor. To assess how many slices are needed to cover the fetal head, we selected and projected all fetal brain masks from the data acquired at 1.5T into the $\mathbf{S}_2$ space. Maximal and minimal extensions were then calculated, resulting in a required coverage of 110 mm.

For the data acquired at 3T, the FOV in the z direction was set to 101.5 mm. This apparent contradiction derives from the following consideration: the lay of the fetus adds constraints to its movement, so that careful planning can allow a reduced coverage to be adequate. Figure 2.20 shows an fMRI dataset from one subject. The fetal resting position is predictable as, often, the head is engaged within the maternal pelvis (red arrow). Therefore, when doing the imaging, the latter can used used as one of the extremes of the field of view, minimizing the changes of data loss in the opposite direction.

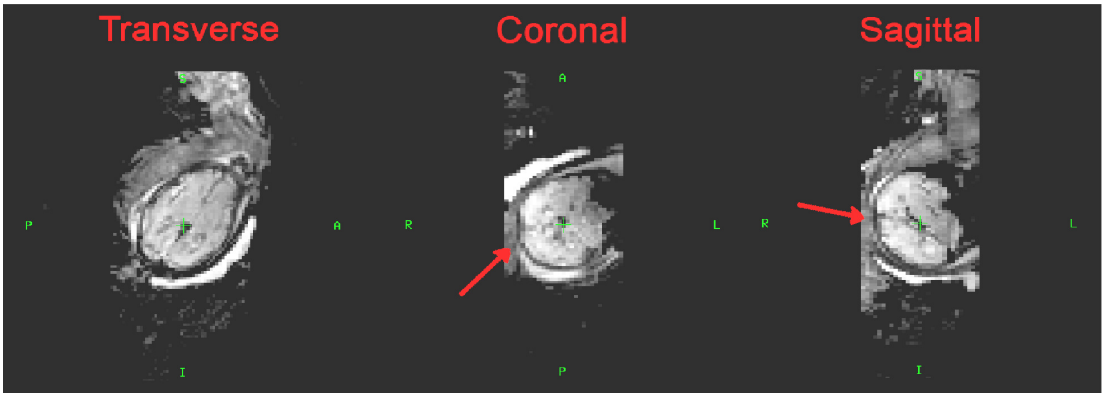

FIGURE 2.20: Standard fetal fMRI dataset. Red arrows indicate the maternal pelvis.

Our cohort of subjects spanned a wide range of different clinical conditions. In total, we were able to acquire 13 controls (mean gestational age: 29.9 ± 3.9 weeks) and 19 clinical subjects (mean gestational age: 29.2 ± 4.6 weeks).

Clinical cases were referred to an MRI scan for the following: ventriculomegaly (7), down syndrome (3), suspected cerebellar vermis rotation and hypoplasia (1), small cerebellum (1), talipes and rocker bottom feet (1), clenched left hand and overlapping fingers with an oedema in the scalp (1), tuberous sclerosis (1), Blake's pouch cyst (1), absent septum pellucidum (1) and maternal myasthenia gravis with asthma (1). There was also one monochorionic diamniotic (MCDA) twin pregnancy.

All data underwent the processing pipeline so far described. However, only the controls underwent final GICA decomposition. In total, we were able to successfully retain 78 % of data. The reasons for rejection were too much motion not recovered by the registration algorithm (2 cases), 2 very artefacted datasets, and the fetal head being outside the imaging FOV (3 cases). However, the latter instances happened again because of bad planning.

2.3.1.2 Acquisition Slice Order

Saturation effects are likely to be more severe for the data acquired at 3T. This is because:

- T_R has changed from 4000 to 2900 ms and the fetal brain is sampled more frequently.
- T_1 increases when the field strength increases.

For this set of data, the acquisition slice order was changed from interleaved 1-3-5-7...2-4-6-8... to ascending 1-2-3-4... .

This choice derived from the results of the following simulation: from one fetal dataset that showed significant movement, we extracted its motion estimates. We then simulated the behaviour of the transverse magnetization with the spin history model of section 2.2.1.5. Different acquisition slice orders were adopted: these were: ascending 1-2-3..., interleaved 1-3-5...2-4-6, and interleaved 1-6-11...2-7-12...3-8-13 (the latter being another option available in Philips). For these simulations, T_1 was set to 2700 ms.

After having run the model, we obtained 3 sets of transverse magnetization, M_T^1, M_T^2 and M_T^3, one for each condition. We then considered the modulation introduced by the disrupted magnetization to the data and defined a score to assess this. Since the output of the spin history model provides a magnetization which is defined in the Scanner coordinates system $\mathbf{S}_1$, it was necessary to project the 3 solutions into the Patient coordinate system, $\mathbf{S}_2$. Our score, P, is defined as the inverse of the coefficient of variation of the magnetization time series.

To verify that the results of the simulation were reliable, an in vivo test was also performed. More specifically, 10 volumes of fetal fMRI data were acquired using the acquisition schemes described above. This subject showed significant motion throughout, so that there was an increased change of observing saturation. Finally, the extent of the modulation on the signal caused by motion was assessed visually.

2.3.1.3 Distortion Correction

All fetal fMRI scans were acquired either using linear or PB shim. During acquisition, linear shimming was always adopted and only 1 volume acquired. This data was used to check whether distortions were not too severe and the presence of other artefacts. If acceptable, a normal fMRI experiment was run using linear shimming; otherwise, PB volume was used. In total, 6 datasets were acquired using PB volume. Field maps were always acquired by setting the shim terms

g_i of equation 1.23 to 0. This is because the Philips environment did not allow copying of the shim calculated during the EPI scans into the field maps.

Therefore, prior to distortion correction, it was necessary to estimate ΔB_0^f of equation 1.24 by adding the field generated by each shim coil to the acquired ΔB_0. This was done by using the pixel shift map of equation 1.22:

$$\Delta ps_{pe} = \frac{\gamma(\Delta B_0 + \sum_{i=1}^{8} \phi_i)}{BW} \cdot \Delta r_{pe} \tag{2.9}$$

This apparently straightforward step is however not trivial. A very important point (and that links with section 1.4.3) is that shim values are always given with respect to the Scanner coordinate system. This is because shim gradients are obviously bound to the scanner and won't move with the table. However, the header file of fetal fMRI data contains only information about the Patient coordinate system.

This fact has two disadvantages:

1. Scanner and Patient coordinate systems don't coincide and the relationship changes for different patient orientations.
2. If the table has moved during the acquisition, this won't be retrievable from the header file.

The first problem was solved by designing a simple experiment: images from a spherical phantom were gathered using 2D-single shot EPI. A field map with all g_i set to 0 was also acquired. For the purpose of distortion correction, the spherical phantom was acquired using the acquisition protocol described in section 2.3.1.1, and it was imaged both feet and head first. The phantom was imaged repeatedly with each of the available shim terms set successively to a non-zero value with all others set to zero. Linear shims were always 0.05 $\frac{mT}{m}$, and the non linear ones 0.5 $\frac{mT}{m^2}$. The purpose of the experiment was to reconstruct the spherical shape of

the phantom. When this is achieved, the exact relationship between Patient and Scanner coordinate systems is established.

Finally, once a displacement field had been calculated, the original fMRI datasets were projected into the undistorted space by using B-splines [Lee et al., 1997].

2.3.1.4 Group Independent Component Analysis at 3T

This last section analyses fetal fMRI data at 3T and those subjects that were considered healthy underwent standard Group ICA. In total, we were able to process 11 subjects out of 13. These two datasets suffered from data loss and a severe fold-over artefact. Similarly to section 2.2.1.8, the data from all patients was placed into a common space defined by selecting the fetal T_2 weighted atlas of 32 weeks created in Serag et al. [2012]. Following this, data was spatially smoothed with a Gaussian Kernel of 4 mm.

2.3.2 Results

2.3.2.1 Acquisition Slice Order

The results from the slice ordering simulation are given in Figure 2.21, where in the first row we show transverse, sagittal and coronal views of the test data from which the motion estimates were taken (first row); and the spatial distribution of P over the fetal head for each of the 3 slice acquisition orders. Mean and standard deviation of these maps for the ascending and the two interleaved acquisitions were 16.89 $\pm$ 12.43, 14.72 $\pm$ 9.56 and 12.17 $\pm$ 7.85. Therefore, this metric suggests that the ascending order is the best acquisition strategy.

It is also interesting to have a closer look at the distribution of P in the 3 conditions - both interleaved acquisitions introduce a modulation across spatially

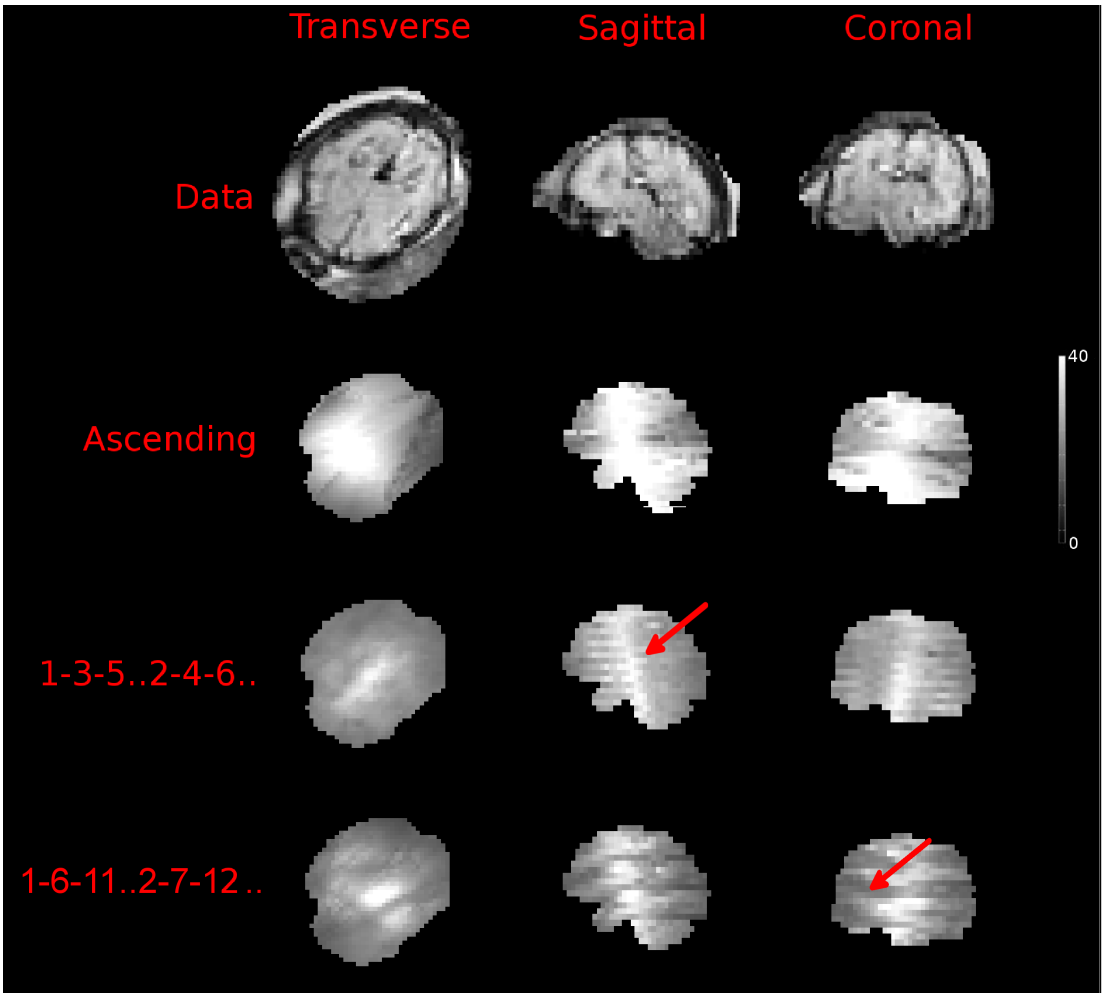

FIGURE 2.21: Transverse, sagittal and coronal views of original data (first row). Second, third and fourth rows represent the score P obtained by simulating the behaviour of the transverse magnetization in the presence of motion using ascending, interleaved 1-3-5...2-4-6 and interleaved 1-6-11...2-7-12...3-8-13.

adjacent slices (red arrows). This modulation appears every 2 slices for interleaved 1-3-5...2-4-6, and every 6 slices with interleaved 1-6-11...2-7-12...3-8-13.

An ascending slice order has the nominal disadvantage of exciting portions of spatially contiguous slices every T_S seconds. However, in the presence of disruptive motion, these slices are likely to be parallel to each other because of the short period of time that interleaves between them. Conversely, interleaved 1-3-5...2-4-6 and 1-6-11...2-7-12...3-8-13 have an increased chance of slices to overlap in

anatomical space. If this happens, spatially contiguous slices will be excited, on average, every $\frac{T_R}{2}$ and $\frac{T_R}{5}$ ms respectively.

The results from the in vivo acquisition is shown in Figure 2.22, where we plot a sagittal cut of the fetal brain obtained by using an ascending slice order (top Figure) and the two interleaved (center and bottom Figures). In all cases, the snapshots were selected to be at times immediately following a sudden/substantial movement. In accordance with the simulation, we observe better data quality when an ascending slice order is selected. We also find evidence that the acquired signal is modulated in a similar fashion to what is predicted by the simulation (red arrows).

FIGURE 2.22: Example of fetal fMRI data acquired at 3T using an ascending slice order (first Figure), interleaved 1-3-5...2-4-6 (second) and interleaved 1-6-11...2-7-12...3-8-13 (third). All data has been acquired using a T_R of 2900 ms. In total, 10 volumes were acquired during each run.

2.3.2.2 Distortion Correction

The distorted data from the phantom experiment acquired as head and feet first is shown in the first and third rows of Figure 2.23 (A and C). Data is presented in the transverse, coronal and sagittal directions for all 8 different shim conditions (columns). We can observe that every time a different shim term is used, the shape of the phantom changes and, in the Figure, areas characterized by large distortions are highlighted with red arrows. In almost every image, there is signal loss due to an air bubble in the phantom. Furthermore, the case head first - g_6 was not acquired. The relationship between Patient and Scanner coordinate system was retrieved by testing each case separately and assessing the recovered spherical shape. Results are shown in the second and fourth rows (B and D) of Figure 2.23.

2.3.2.3 Effect of table motion on high order shim

For simplicity, we assume that Patient and Scanner coordinate systems defined in section 1.4.3 coincide apart from a table net displacement z_0. The relationship between the two coordinate systems is therefore: $x = x_p$, $y = y_p$ and $z = z_p - z_0$. Here, the letter p stands for Patient.

Written in the Patient coordinate system, equation 1.23 becomes:

$$\begin{cases} \phi_1 = G_1 \cdot x_p & \phi_5 = G_5 \cdot z_p = G_5 \cdot (z + z_0)x_p \\ \phi_2 = G_2 \cdot y_p & \phi_6 = G_6 \cdot z_p = G_6 \cdot (z + z_0)y_p \\ \phi_3 = G_3 \cdot z_p = G_3 \cdot (z + z_0) & \phi_7 = G_7 \cdot (x_p^2 - y_p^2) \\ \phi_4 = G_4 \cdot f(x_p, y_p, z_p) & \phi_8 = G_8 \cdot 2x_p y_p \end{cases} \tag{2.10}$$

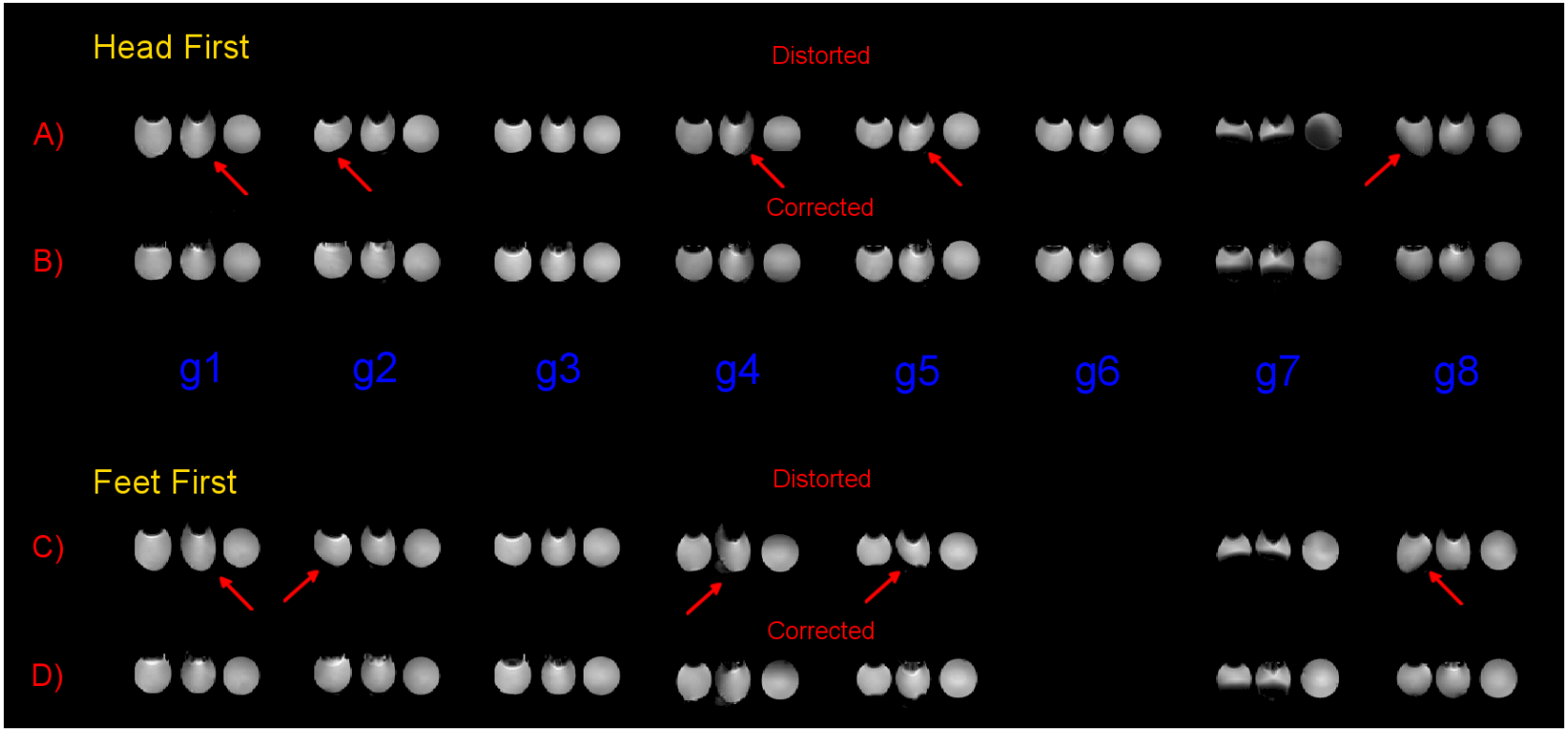

FIGURE 2.23: Distortion correction experiment: rows A and B report the spherical phantom acquired as 'feet first' before and after distortion correction. Data is shown in transverse, coronal and sagittal order. Rows C and D report the same data acquired 'head first'. All data was acquired using different shim settings (term g_i of each column) and areas characterized by large distortions are indicated with red arrows.

where $f(x_p, y_p, z_p) = z_p^2 - 0.5x_p^2 - 0.5y_p^2 = (z+z_0)^2 - 0.5x_p^2 - 0.5y_p^2$. If the expressions for ϕ_4, ϕ_5 and ϕ_6 are expanded, we find linear terms of type $(2G_4 z_0) \cdot z$, $(G_5 z_0) \cdot x$ and $(G_6 z_0) \cdot y$. These terms vary linearly along the directions z, x and y, and they are proportional to the table net displacement z_0 and shim strengths [1].

This effect is depicted in Figure. 2.24, where we show an fMRI dataset from a 31+1 weeks old fetus. Linear and quadratic shim terms were 0.012944, 0.015406, 0.030413 $\frac{mT}{m}$ and 0.232347, -0.117341, 0.107429, -0.129547, -0.034591 $\frac{mT}{m^2}$ and the table net bed displacement from laser calibration was 56.19 mm. The first row (A) shows transverse, coronal and sagittal views of a T_2 anatomical reference scan, and the second (B) the distorted fMRI data. Third row (C) shows the result of distortion correction achieved by including the table position, whereas the fourth row (D) reports the same when this is deliberately and incorrectly set to 0. Better distortion correction was achieved in the first case and, actually, the last row shows a linearly varying distortion pattern due to the 3 extra linear terms of equation 2.10.

2.3.2.4 Group Independent Component Analysis at 3T

Group ICA extracted 27 components, 9 of which were selected as resembling RSNs in the fetal brain. The spatial distribution of these components is shown in Figure 2.25. A remarkable feature that we observe is that the first six components (A to F) have a very similar spatial distribution to those networks that we have obtained from the data at 1.5T (Figure 2.19). The cross correspondence of networks obtained from independent data reinforces the belief that the effect described is physiological. Furthermore, the following networks are detected: (G) predominately left sided motor network comprising the primary motor cortex anterior to the central sulcus (while C is a somatosensory network posterior to the central sulcus - and the sensori-network at 1.5T is now divided into two distinct

[1] Note that, when expanding ϕ_3, the term $G_3 z_0$ appears. However, as opposed to ϕ_4, ϕ_5 and ϕ_6, this is a constant shift in frequency, and therefore it is accounted for by the frequency calibration step that is always performed prior to scanning.

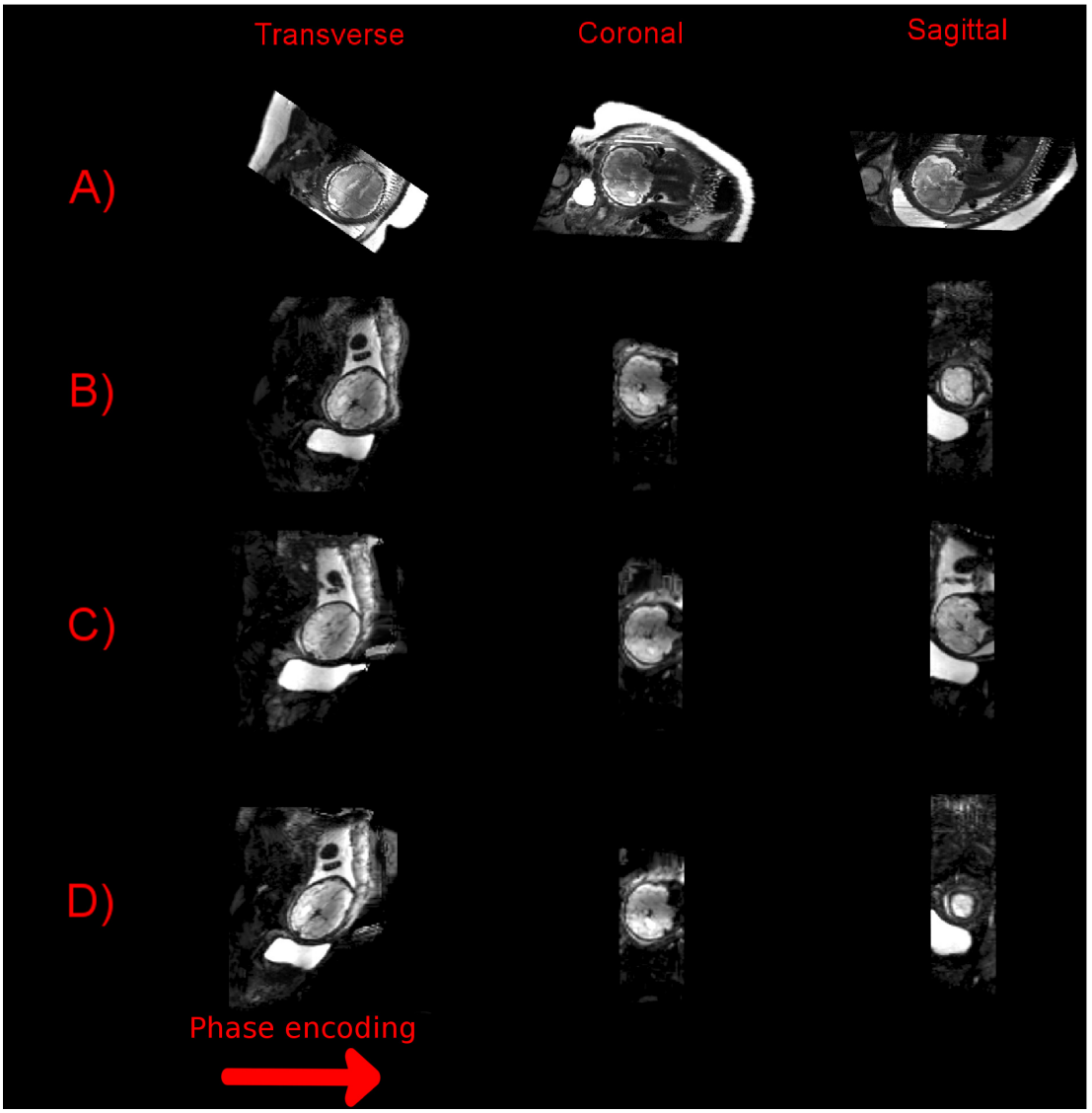

FIGURE 2.24: Effect of table net displacement. First row (A) shows an anatomical T_2 weighted image acquired as reference and second (B) original distorted fMRI data. Third and fourth rows (C and D) show respectively the distortion correction that is achieved by considering and not considering the table net displacement z_0 from the calibration of the laser.

parts); (H) is a left sided dorsal visual stream network over the posterior parietal lobe; (I) a network comprising the cerebellum; (L) most likely the effect of blood in the straight sinus and therefore not related to neuronal activity. It is still interesting because it underlines the capability of ICA to recover signal with a physiological meaning.

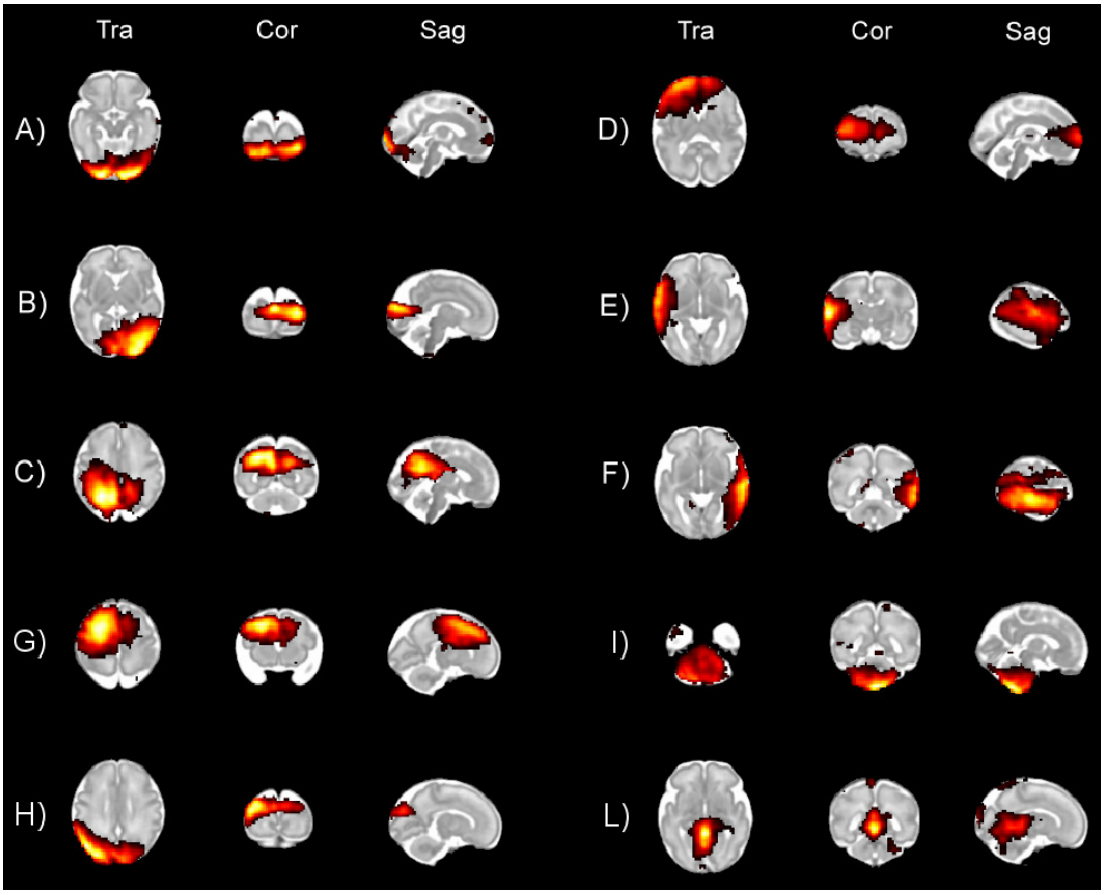

FIGURE 2.25: Transverse, coronal and sagittal views of RSNs at 3T given by Group ICA overlaid onto a fetal template of 32 weeks (all z-score maps were thresholded using the cut-off value given by Melodic). The left side of the Figure corresponds to the left side of the brain.

2.4 Conclusions

This chapter proposes a framework to investigate spontaneous fluctuations of the BOLD signal in the human brain during a key period of development, before the natural term of birth. Performing fMRI of the fetus *in utero* requires methods that are tolerant of the large displacements caused both by maternal respiration and by unpredictable spontaneous movements performed by the fetus, leading to a challenging motion correction problem. Previous studies on fetuses employed methods directly adapted from those applied to adult data, in which complete stacks of slices covering the whole brain volume are processed together assuming negligible intra-stack movement. This assumption is frequently violated and

results in a high rejection rate of data.

Here we present a method designed to directly address the consequences of motion with the aim of utilizing as much as possible of the acquired data. The method has been tested on a population formed by 16 fetuses acquired at 1.5T, and subsequently extended to process a larger population sample at 3T.

The 5 fetuses at 1.5T for whom there was incomplete data or signal voids cannot be recovered by application of a motion correction procedure. So they represent a loss, but not a failure of our method. As far as we can tell the success rate quoted for previous studies [Jakab et al., 2014, Schöpf et al., 2012, Thomason et al., 2013] was for data that was otherwise acceptable, so should be directly compared to 11 of our subjects. Thus the most conservative statement for the success rate of this study is 73%. For the 3 cases that we could not process, the problem was that the registration step failed. However, if we had adopted a strategy of data rejection, we could have preserved more than half of each of these time series, but this would have clouded the eventual comparisons with other methods so we did not do this.

For the fetuses acquired at 3 Testa, the success rate is 93 %. The increase is due to a reduction of the repetition time T_R, a more efficient coverage of the fetal head via careful planning plus other factors. Having changed the slice acquisition order from interleaved to ascending was furthermore not only beneficial in terms of spin history attenuation, but it improved the registration accuracy as well as the quality of scattered interpolation scheme.

The proposed method is a combined approach of slice to volume registration and scattered data interpolation with bias field and spin history corrections. More conventional distortion correction methods were also used. The framework was tested both with simulations and on *in vivo* data acquired from fetal subjects. Starting from raw stacks of EPI images acquired as parallel slices in Scanner coordinates, it outputs data on a regular grid in an anatomical space in which

the subject is static over the time course. These regular data are then available for any choice of fMRI analysis method. In this case, Group ICA was applied and was able to recover Resting State Networks that are consistent with those already mapped in preterm babies [Doria et al., 2010, Smyser et al., 2010] and have common features with RSNs found in older, term born neonates [Fransson et al., 2007, 2009]. We also show how Resting State Networks remain consistent between independent datasets and this confirms the reliability of the pipeline as a whole.

The modular approach adopted in this study, in which motion correction is a separate step from functional data analysis offers great flexibility and is in line with most other processing pipelines currently adopted. It allowed us to focus on the key challenging feature of fetal datasets while providing results that are directly comparable with other analyses. A more integrated approach would be possible and there have been a number of studies in the adult fMRI literature that attempt to jointly address motion correction and functional analysis [Liao et al., 2005]. A natural extension of the current approach for group analyses would be to project the scattered data directly into standard space and only then interpolate onto a standard regular grid. This is something we will explore in future studies.

The key enabling process in the proposed pipeline is alignment of each acquired slice within anatomical space ($\mathbf{S}_2$). The simulations demonstrated that without this step the capability to detect functional signals is substantially reduced and there is supporting evidence from adult studies [Kim et al., 1999]. Slice by slice alignment is well established for anatomical fetal imaging and proved effective in this application. However, there were three fetal subjects acquired at 1.5T and two at 3T for which we were not able to sufficiently correct for movement. The babies in question had moved rapidly for extended periods so that the earlier stages of the alignment processes, which rely on working with packages of temporally contiguous slices to robustly determine approximately correct slice locations,

failed. Developing registration methods that can succeed with such chaotic data remains a challenge to be addressed further.

EPI images are extremely vulnerable to geometrical distortions caused by magnetic field inhomogeneity [Jezzard and Balaban, 1995]. However, distortions *in utero* tend to be less pronounced than in other fMRI experiments for the simple reason that the fetal head is surrounded by amniotic fluid and maternal soft tissue; susceptibility differences at air-tissue boundaries are therefore generally not present close to the fetal head. The pattern of distortion is more variable than in ex-utero brain imaging, because the origins of magnetic field inhomogeneity (such as bubbles in the maternal gut) have no fixed relationship to the fetal head. For the data acquired at 1.5T, we found that distortion was not the first priority to be addressed and so focused on other key challenges. We however managed to correctly address the problem for all data acquired at 3T.

Notwithstanding the limitations discussed above, we were able to identify in the fetuses studied RSNs with spatial representations consistent with those previously described in preterm infants. Networks that are likely to involve an underlying structure of long-range connectivity in full term neonatal subjects were found to be unilateral or incomplete in our fetal population, further supporting theories that their maturation is associated with rapid neuronal growth in the third trimester of human gestation [Doria et al., 2010].

So far all data has been treated as a single group for the analysis, which means that a range of gestational ages and hence maturational states were combined. This will have increased the variability in the data, and the extracted networks are likely to emphasize the most conserved features, without sensitivity to detect emerging or rapidly changing features within the age range. Applying the proposed techniques to a larger study population will enable changes with gestational age to be explored. It can also equally be applied to experiments that seek to correlate fetal brain activity to external stimuli [Fulford and Gowland, 2009, Gowland and Fulford, 2004].

By fully correcting for fetal motion and the secondary effects of variable bias field, spin history and image distortions, it is now possible to start to systematically perform fMRI in utero on a larger scale without the need to discard large fractions of data. The presented framework, which can be applied to resting state and stimulus based paradigms, holds promise as the basis for reliable and detailed functional brain mapping across the third trimester of gestation.

Chapter 3

An exploration of task based neonatal fMRI with echo shifting EPI

3.1 Motivation

Optimal BOLD to noise contrast (BNC, described in section 1.5.2) in neonatal and fetal fMRI is hard to achieve because of the much longer T_2^* values in developing brain tissue in comparison to those in the mature adult brain.

Fetal, preterm and neonatal brains are indeed characterized by longer T_2^* values than adults. This is due to their higher content of water and to incomplete myelination, synaptogenesis and synaptic pruning processes [Rivkin et al., 2004]. The difference between newborns and adults is substantial. In healthy adults, T_2^* ranges from 40 to 60 ms at 1.5T [Bandettini et al., 1994]. In contrast, for the same field strength, the literature reports T_2^* values of 154 ± 24 ms in the thalamic deep grey matter of healthy fetuses [Vasylechko et al., 2014], and of 137 ± 13 ms for babies born prematurely [Rivkin et al., 2004]. T_2^* decreases as a function of

age, and in neonates at term equivalent age the same study shows measurements of 127 ± 23 ms.

Most often, the echo time selected in previous neonatal and fetal fMRI studies had been substantially shorter than the T_2^* in the developing brain [Doria et al., 2010, Ferrazzi et al., 2014, Fulford and Gowland, 2009, Schöpf et al., 2012, Smyser et al., 2010, Thomason et al., 2013]. This contradicts the conventional approach of optimizing fMRI sequences, where it is suggested the matching of the echo time and T_2^* [Bandettini et al., 1994]. However, the use of a long echo time would typically increase the minimum repetition time, resulting in inefficient sampling.

This information motivates a re-think of 2D-EPI sequences to match the magnetic tissue properties of neonates and fetuses, and raises interesting challenges as longer echo times usually decrease the rate with which data can be acquired. This is also regarded as an important factor in fMRI.

In this chapter, we apply echo shifting [Moonen et al., 1992] to task based neonatal fMRI in order to achieve an improved BNC and efficient data sampling at the same time. Echo-shifted EPI (es-EPI) is a modification of a standard 2D-EPI sequence which enables echo times longer than the time between consecutive excitations.

The idea of extending the echo time while maintaining efficient sampling was firstly introduced in Moonen et al. [1992]. Since then, echo shifting has found different applications - for example, in the field of T_2^* weighted bolus tracking [Moonen et al., 1994] and diffusion weighted images (DWI) [Delalande et al., 1999]. Another popular sequence that implements echo shifting is the PRESTO sequence [Liu et al., 1993].

There have been two studies whose aim was to perform an es-fMRI experiment [Chang et al., 2013, Gibson et al., 2006]. In the work of Gibson et al. [2006], images with an echo time of 40 ms were acquired. The acquisition time per slice was 27 ms. 5 healthy volunteers were scanned utilizing a visual stimuli in the form of a flashing checkerboard. The efficient sampling of es-EPI allowed

the authors to acquire a set of 9 sagittal slices placed over the left hemisphere in 243 ms. The work of Chang et al. [2013] also made use of echo shifting to perform a fast fMRI experiment. Eight healthy participants were recruited and engaged in a visual experiment. The purpose of the study was to dynamically sample the hemodynamic response function. This was achieved by designing a sequence with a repetition time of 25 ms. The reported echo time was 33.2 ms.

While the main focus of these 2 studies was to shorten the repetition time allowing, for example, the separation of neuronal signal from cardiac pulsation and respiration [Birn et al., 2006] - our approach is different. Here, for given and fixed repetition time T_R, we use echo shifting to stretch the echo time T_E and to match it to the magnetic properties of neonatal and fetal brains. To assess whether an increase BOLD signal sensitivity would be observed, fMRI experiments were performed on neonates with the es-EPI sequence and a conventional 2D-EPI acquisition performed with two different echo times (the longest equivalent to the effective echo time for es-EPI) and a passive motor stimulus was used. From the results of the latter analysis, an average increase of 78 $\pm$ 41 % in BOLD to noise contrast was observable when comparing late to short echoes. Furthermore, es-EPI allowed the acquisition of data with an identical contrast to the late echo, but more efficiently.

3.2 Materials and Methods

3.2.1 The concept of Echo Shifting

es-EPI is a modification of a standard 2D-EPI sequence which enables echo times longer than the time between consecutive excitations ($T_E > T_S$).

Figure 3.1 shows an es-EPI sequence. Similarly to what was presented in Chang et al. [2013], the coloured components indicate the gradients that achieve echo shifting, whereas the black lines represent a normal 2D-EPI sequence. In this

representation, dashed lines are part of a standard 2D-EPI readout, but they are not present when performing echo shifting. The Figure shows two consecutively acquired slices of the entire fMRI acquisition; the signal coming from the j^{th} slice is immediately crushed after excitation and only gets refocused after excitation of the next slice. The signal coming from the excitation of the $(j+1)^{th}$ slice is crushed, and later read after the following slice has been excited. Our implementation introduces a phase accumulation of 2π (or multiples) along each pixel in the read, phase encoding and/or slice directions. With this choice, spins positioned symmetrically with respect to the center of every voxel sum up destructively.

There is a simple set of constraints that need to be fulfilled in order to achieve echo shifting. These constrains are highlighted in Figure 3.1, where we indicate with A_x, A_y and A_z the crushers and with B the slice selective gradient. In this example, the phase dispersion along each direction is 2π and the effective echo time is $T_E = T_S + T_E^*$, where T_E^* is the nominal echo time of the corresponding standard EPI sequence.

Let's consider the crusher A_z after the j^{th} RF pulse. After its application, the accumulated phase $\Delta\phi_z$ across a slice of thickness Δz is [Haacke et al., 1999]:

$$\Delta\phi_z = \gamma A_z \Delta z \tag{3.1}$$

Therefore, in order to achieve a $2\pi n$ shift (with $n = 0, 1, 2...$), A_z needs to be:

$$A_z = \frac{2\pi n}{\gamma \Delta z} \tag{3.2}$$

Equivalent considerations can be applied when considering spins along the phase encoding direction and therefore $A_y = \frac{2\pi n}{\gamma \Delta y}$. A slightly different area is needed to shift the signal along the read direction (k_x). This is equal to $A_x = \frac{\pi(2n-1)}{\gamma \Delta x}$.

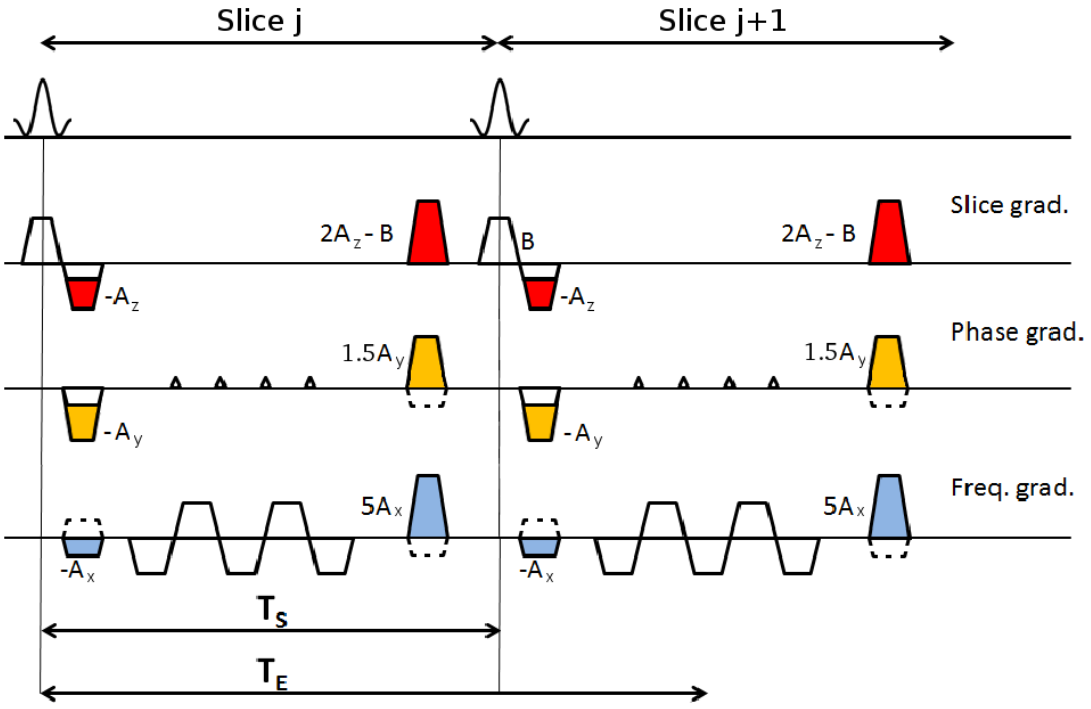

FIGURE 3.1: es-EPI sequence. The coloured components highlight the gradients that achieve echo shifting as in Chang et al. [2013], whereas the black lines refer to a standard 2D-EPI sequence. Dashed black lines belong to a standard 2D-EPI sequence and the shift is 2π along each direction.

Let's imagine an experiment in which the signal is shifted *along the read direction only*. We further assume that the number of phase encodes is even. The green portion of Figure 3.2 represents the k-space acquisition trajectory achieved with standard EPI. However, a shift is applied along the read and this corresponds to the horizontal direction in the Figure. To achieve this, the polarity of the prephaser gradient of Figure 3.1 is inverted ($-A_x$ term) and the effect is to move in the opposite direction along k_x (Figure 3.2, position 1 instead of position 4 as in 2D-EPI). A standard EPI readout is then played out and a shifted k-space plane is acquired (red portion in Figure 3.2, finishing at position 2). Following this, the refocusing gradient (of area $5A_x$) is applied (Figure 3.2, position 3) and subsequently the second prephaser gradient belonging to the following excitation (Figure 3.2, position 4). Only at this stage, the readout encodes the signal coming from the previously excited slice. The same process is then repeated for all other

slices.

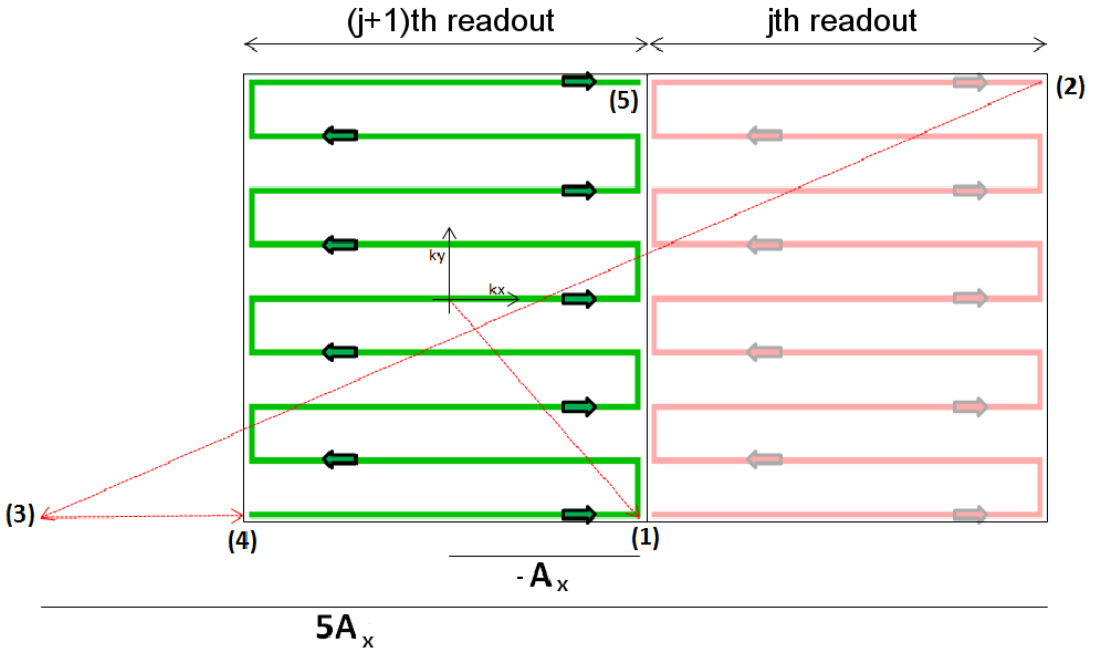

FIGURE 3.2: es-EPI k-space trajectory achieved by shifting the signal along the read direction. The phase dispersion is 2π for each voxel.

An equivalent diagram can be derived when considering the phase encoding direction k_y. However, it is not possible to do it for the slice direction. This is because, in 2D multislice imaging, there is no simple k-space representation of the third dimension.

3.2.2 Contamination effect and tSNR test

During the $(j+1)^{th}$ readout, there is the potential issue of contamination of the signal corresponding to the j^{th} excitation with that coming from the slice excited by the $(j+1)^{th}$ pulse. If this happens, j^{th} and $(j+1)^{th}$ slices will be encoded together, hindering further analyses. This effect can potentially be very detrimental as the second excitation carries more signal than the first due to the shorter effective T_E^*.

The gradient following the $(j+1)^{th}$ excitation must sufficiently crush the signal excited by that pulse so that it does not contaminate the signal refocused from the j^{th} slice.

To assess this, we characterize the contribution of the signal excited by $(j+1)^{th}$ pulse onto the $(j+1)^{th}$ readout. When this is null, it should be comparable to noise. The polarity of the refocusing gradients at the end of each readout was therefore inverted so that the signal coming from the j^{th} slice would not refocus. The strength of the crushers was modified, so that the phase accumulation across each pixel was either 2π or 4π. This was repeated using different combinations of shifts along frequency, phase and slice encoding directions. All of the data was acquired on a 3-Tesla Achieva Philips system and the tests were performed on a water phantom. Images were acquired with a T_E^* of 20 ms and a SENSE factor of 2. With this set up, the effective echo time T_E was 63 ms and data resolution $2.5 \cdot 2.5 \cdot 2\ mm^3$. A noise reference scan obtained by turning the RF pulse off was also acquired.

We also quantified the temporal Signal to Noise Ratio (tSNR) of the sequence and compared it to an equivalent EPI acquisition. To do so, another bottle phantom was scanned at an isotropic resolution of 2 mm, repetition time T_R of 2545 ms and effective T_E of 75 ms with a SENSE factor of 2. The phantom contained 31.5 $mmol$ of $NiCl_2$ to ensure a short T_2, therefore avoiding signal propagation of the transverse magnetization across different time points [Chung and Duerk, 1999]. To match the repetition time of the standard EPI sequence to echo shifting, roughly half of the slices were acquired. Resolution and echo time were kept the same and, in total, 200 volumes were imaged. Image based shimming was employed [Schneider and Glover, 1991], and shim values kept constant across the 2 scans. Finally, due to the different coverage achieved in the two acquisitions, the tSNR was evaluated only within overlapping regions.

3.2.3 Data Reconstruction

By using echo-shifting, the slice position corresponding to each readout no longer matches the slice excited by the most recent RF pulse. This causes SENSE reconstruction to fail unless the labelling of the slices is corrected.

To investigate this, two spherical phantoms were imaged using echo shifting with a 32 channel cardiac coil. Sequence parameters where: $T_R = 1300\ ms$ and effective $T_E = 69\ ms$. To achieve this, T_E^* was 25 ms and 30 slices were acquired at the resolution of $2.8 \cdot 2.8 \cdot 3.5\ mm^3$. Shifts of 4π were applied along read, phase and slice directions. An equivalent standard EPI acquisition was run, using a T_E of 69 ms and a repetition time of 2600 ms. The SENSE factor was 2 and the acquisition slice order interleaved (1-6-11..2-7-12..).

Reconstruction was performed offline with the ReconFrame software (http://www.gyrotools.com/products/gt-recon.html), and the results compared to standard scanner reconstruction.

3.2.4 Neonatal fMRI experiments

This section focuses on the use of echo shifting to perform an optimized neonatal fMRI experiment. The acquisitions were performed on a 3T system using a standard 32 channel head coil. Ethical approval for the study was obtained from the NHS research ethics committee, and written parental consent was obtained prior to all sessions of data acquisition. The study population consisted of 5 healthy infants at term (3 of which were sedated with oral chloral hydrate at 30-50 mg/kg/dose prior to scanning) of 41.4 ± 1.14 weeks at scan; and 8 preterm infants of 33.6 ± 1.5 weeks at scan (images acquired during natural sleep). One preterm infant was known to have intra-uterine growth retardation (IUGR). Infants with focal brain pathology (such as stroke or intracerebral hemorrhage), diagnosed metabolic or genetic abnormalities, and those with a history of requiring vigorous

resuscitation at delivery were excluded from the study. es-EPI data was acquired with T_E and T_R of 75 and 2545 ms respectively. These parameters were chosen to ensure that the transverse magnetization had decayed away completely prior to the application of the next RF pulse ($T_2 << T_R$ - Williams et al. [2005]). In plane resolution was 2 mm, and the SENSE factor 2.

To test the hypothesis that echo shifting provides an improved sensitivity to BOLD contrast functional responses, dual-echo single shot EPI datasets were also acquired with T_E of 25 and 75 ms, an identical T_R of 2545 ms and matched spatial resolution. To ensure identical sampling properties, a reduced number of slices was again used in the dual-echo experiments (20) compared to the es-EPI sequences(46). The slice thickness was either 2 or 3 mm (the latter selected when better coverage of the motor cortex was required for the dual echo acquisitions). The number of frames was 125 (total scan time roughly 5 minutes and 20 seconds) and echo shifting was the first scan to be run. A sensori-motor stimulus was achieved by using a fully automated and pneumatically driven fMRI compatible robotic interface designed and built for use with fragile neonatal subjects [Allievi et al., 2013]. The interface was placed onto the right wrist and hand of the majority of infants prior to scanning (the left hand was used for the IUGR infant due to pre-existing venous access on the right hand).

Precisely controlled and highly reproducible passive extension/flexion movements of the wrist were achieved through a piston actuator, controlled by compressed air and dedicated software [Allievi et al., 2013]. The timing of stimulation was synchronized to the image acquisition via detection of the MRI scanner transistor-to-transistor logic (TTL) pulse emitted with each T_R. A simple block experimental paradigm was used, consisting of alternating 22.9 second periods (9 T_R) of 0.5 Hz wrist extension/flexion ('on') and rest ('off'). Data was analysed with tools implemented in the FMRIB software library (FSL; `http://fsl.fmrib.ox.ac.uk/fsl/fslwiki/` [Smith et al., 2004]). Standard pre-processing steps were applied to the data after visual identification of high motion frames; these included linear

spatial realignment to the middle volume, spatial smoothing (Gaussian filter of 4 mm FWHM), slice timing correction, and high-pass filtering (cut-off 50 seconds). Data was then analysed using the General Linear Model (GLM) as implemented in FEAT, with the input boxcar function convolved with a set of linear basis functions optimised for use with neonatal subjects [Arichi et al., 2012].

We finally quantify the the % of BOLD signal change and the BNC in all datasets. To evaluate the latter, we used equation 1.26. In this study ΔR_2^* is not known, but it is dependent on the brain activation rather than acquisition parameters, so was treated as a constant in all single subject comparisons between acquisitions. Before calculating % of BOLD signal change, all time series were low pass filtered with a standard Butterworth filter (cut-off frequency 0.12 Hz) to remove high frequency noise. We finally compare the z statistics from all activation maps in the 3 sequences.

3.3 Results

3.3.1 Contamination effects and tSNR test

Figure 3.3 shows the results obtained from the contamination experiment. The first row shows a reference scan acquired by using the standard 2D-EPI sequence. Read, phase and slice directions are outlined in red. The noise scan is presented in the second row of the same Figure. Noise has a structured appearance because of SENSE [Pruessmann et al., 1999]. Nevertheless, this is the image that we would like to reproduce when using echo shifting with the refocusing gradients acting as crushers instead.

Rows A-G show echo shifted images for different directions and degrees of gradient spoiling. When a specific shift/strength is not present, it means that set of data was not acquired. Apart from the very first image, all images have identical display settings. Shifting only along one direction did not completely suppress

the signal. This effect becomes less prominent using stronger gradients (second column) - imposing a crusher along the read (A) direction produced an edge artefact along the phase encoding direction; echo shifting can in fact be seen as a shift of the sampled k-space domain as presented in Figure 3.2. When a shift is applied along the read direction, the effect is that the k-space region actually sampled is shifted to the right or to the left along the k_x direction relative to a standard EPI readout. However, the same range of k_y spatial frequencies is still sampled as in the corresponding 2D-EPI sequence. After Fourier transforming, the result is an edge artefact along the phase encoding direction. Similar considerations can be done when imposing the shift along the phase encoding direction (B). Also, when the shift is applied along the read and phase at the same time (D), the edge artefact appeared rotated by 45° along the xy plane.

Imposing a 2π shift along the slice direction (C) did not suppress the signal entirely. However, the effect was reduced when using a stronger slice dephaser. Combining slice with read or phase shifts (E and F) suppressed the signal well. There were however remaining localized components of signal. When shifting along all three directions at the same time (G), the signal was well suppressed both using a shift of 2π and 4π and the latter was used for subsequent in vivo acquisitions.

Finally, the tSNR test showed almost identical values for echo shifting and standard EPI run at long echo times (18.5 ± 4.4 and 18.7 ± 4.3 in the first and second case), suggesting that the stability of the signal is not compromised.

3.3.2 Data Reconstruction

Standard and es-EPI data from the reconstruction experiment (scanner reconstruction) are shown in the first and second columns of Figure 3.4. The third column shows a magnified version of the es-EPI data and it is immediately visible the presence of an artefacted region (right red arrow). This corresponds to

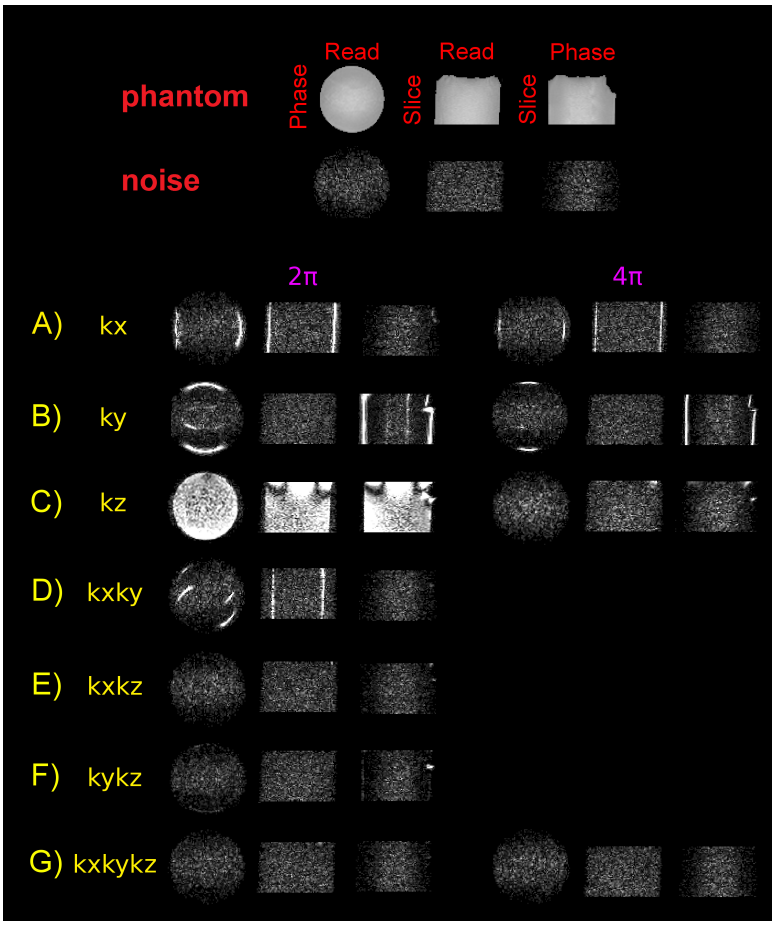

FIGURE 3.3: Echo shifted contamination experiment: first row shows the reference scan and the second the noise measurement. Read, phase and slice directions are outlined in red. Rows A to G show the contaminating signal excited by the $(j+1)^{th}$ RF pulse for different combinations of shifts along read (k_x), phase (k_y) and slice (k_z) directions. First and second columns correspond to shifts of 2π and 4π.

slices 1 to 5 counting from the inferior to the superior direction. Also, when comparing EPI with es-EPI data, the latter appears shifted towards the superior direction (central red arrow) of 6 slices.

As mentioned before, the labelling of slices is incorrect when using echo shifting and SENSE. This results in the failure of the reconstruction at the edges of the image because those slices are paired to sensitivities coming from the opposite sides of the field of view.

The first two columns of Figure 3.5 show a coronal view of the reconstruction

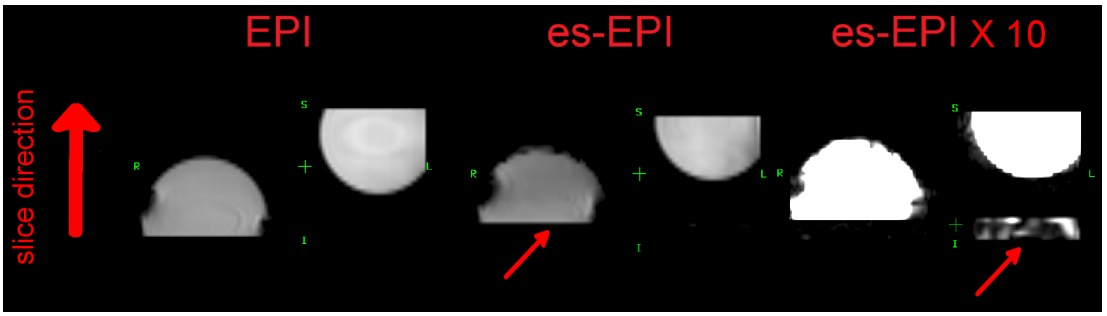

FIGURE 3.4: Scanner reconstruction for the experiment described in section 3.2.3. The Figure reports the coronal view of two spherical phantoms. First column is a reference EPI scan, second and third es-EPI data. The third column is windowed differently to delineate a region with artefacts.

obtained with ReconFrame for the standard and es-EPI data, and there are differences from the scanner reconstruction. However, after rearranging the k-space data matrix, it is possible to recover the signal at the edges of the image (right red arrow).

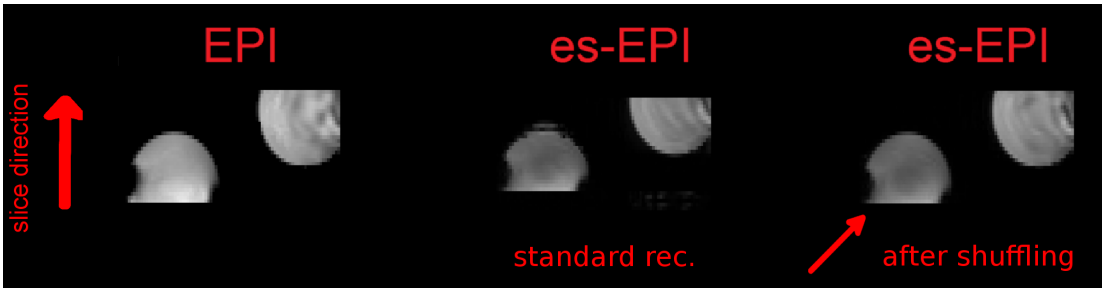

FIGURE 3.5: ReconFrame reconstruction for the experiment described in section 3.2.3. The Figure reports a coronal view of reconstructed EPI data (first image) and es-EPI before and after reshuffling (second and third images).

3.3.3 Neonatal fMRI experiments

In total, the scanning duration for each scan was 5 minutes and 20 seconds. There was therefore a high chance for a neonate to move during this period.

Motion corrupted frames were removed from all datasets. When both dual and echo shifted EPI could be analysed, the same number of frames was always removed from both time series so as not to favour either of the two acquisitions

when assessing BOLD activation. Table 3.1 reports the success rate of this study plus the age at scan of all infants (ascending order). When 'Yes', activation resembling the predicted behaviour was found in the left hemisphere in the motor cortex (right motor cortex for the baby with IUGR). In unsuccessful datasets ('No'), head motion was either too great or frequent to allow accurate analysis even following frame removal and standard motion correction steps during data pre-processing. The number of frames that were retained for the final analysis are reported in the fourth column of the Table.

Baby	Weeks	Dual-Echo	es-EPI	Retained frames
1	32	No	Yes	125
2	32	Yes	Yes	105
3	33	Yes	Yes	125
4	33	Yes	No	125
5	33	Yes	No	125
6	35	Yes	No	125
7	35	Yes	Yes	99
8	36	No	No	-
9	40	No	No	-
10	41	Yes	No	78
11	41	No	Yes	90
12	42	Yes	Yes	70
13	43	Yes	Yes	74

TABLE 3.1: Age of scan (ascending order) in weeks and positive/negative outcome (Yes/No) for dual-echo and es-EPI. The number of retained frames is on the right hand side.

Figure 3.6 presents transverse, coronal and sagittal views of the es-EPI data (first row) and of the dual-echo data (second and third rows) for subject number 3. Tissue contrast is very different between the echoes of the dual echo sequence, which also provided only partial brain coverage given the same repetition time used in all acquisitions. Overlaid on the EPI images, are the clusters of activated voxels obtained by the GLM analysis. Activated clusters are in the left contralateral primary somatosensory cortex.

Figure 3.7 (A) reports the % of BOLD signal averaged over the the top quartile of active cluster for the 11 subjects for which there was a detectable activation

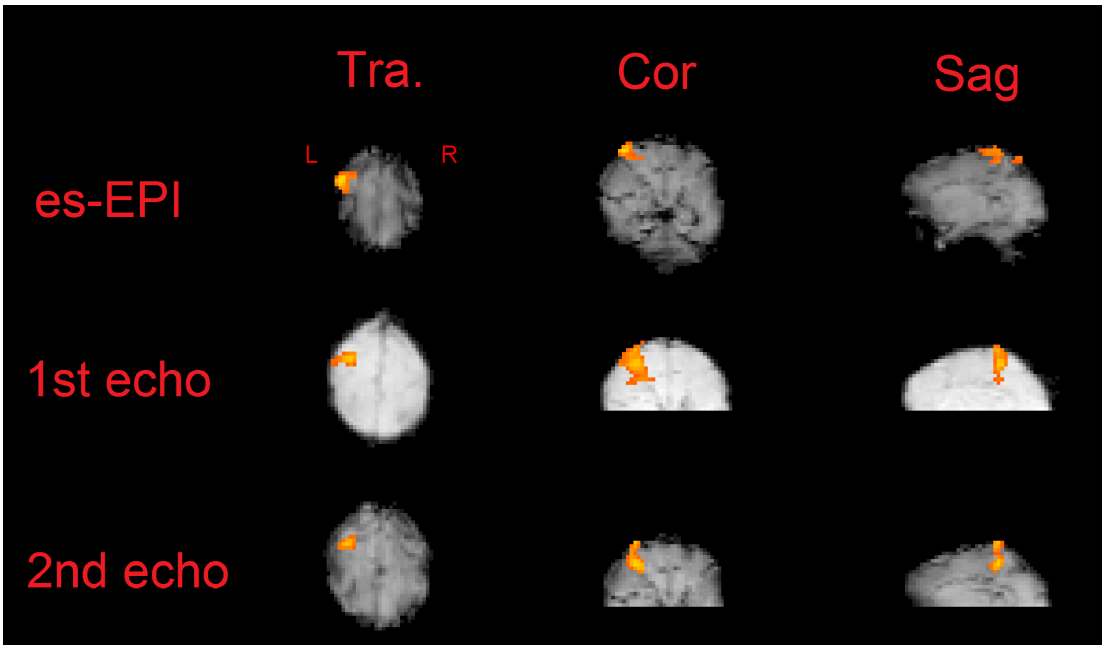

FIGURE 3.6: Left: transverse, coronal and sagittal views of the activated clusters for es-EPI data (first row) and dual-echo experiments (second and third rows) for subject number 3.

in one or both acquisitions. Left plots show BOLD activation in dual echo data (time courses relative to first and second echoes are represented in blue and red respectively), and on the right the same for es-EPI. The data relative to the second echo tends to vary more than the first in all cases.

In total, there were 5 cases in which both echo shifting and dual echo EPI produced clear activation signals in the motor area.

Figure 3.8 reported original (first row) and filtered (second) BOLD time series for subject number 3. These were used to calculate % of BOLD signal change which is reported in Table 3.2. In all the dual echo experiments that were successful, there was a larger BOLD activation during the second echo. We also observed a similar trend in echo shifted data - and means and standard deviations of the % of BOLD signal change across all subjects were $0.3 \pm 0.1\%$ and $0.7 \pm 0.3\%$ in the dual echo sequence, and $1 \pm 0.5\%$ for es-EPI.

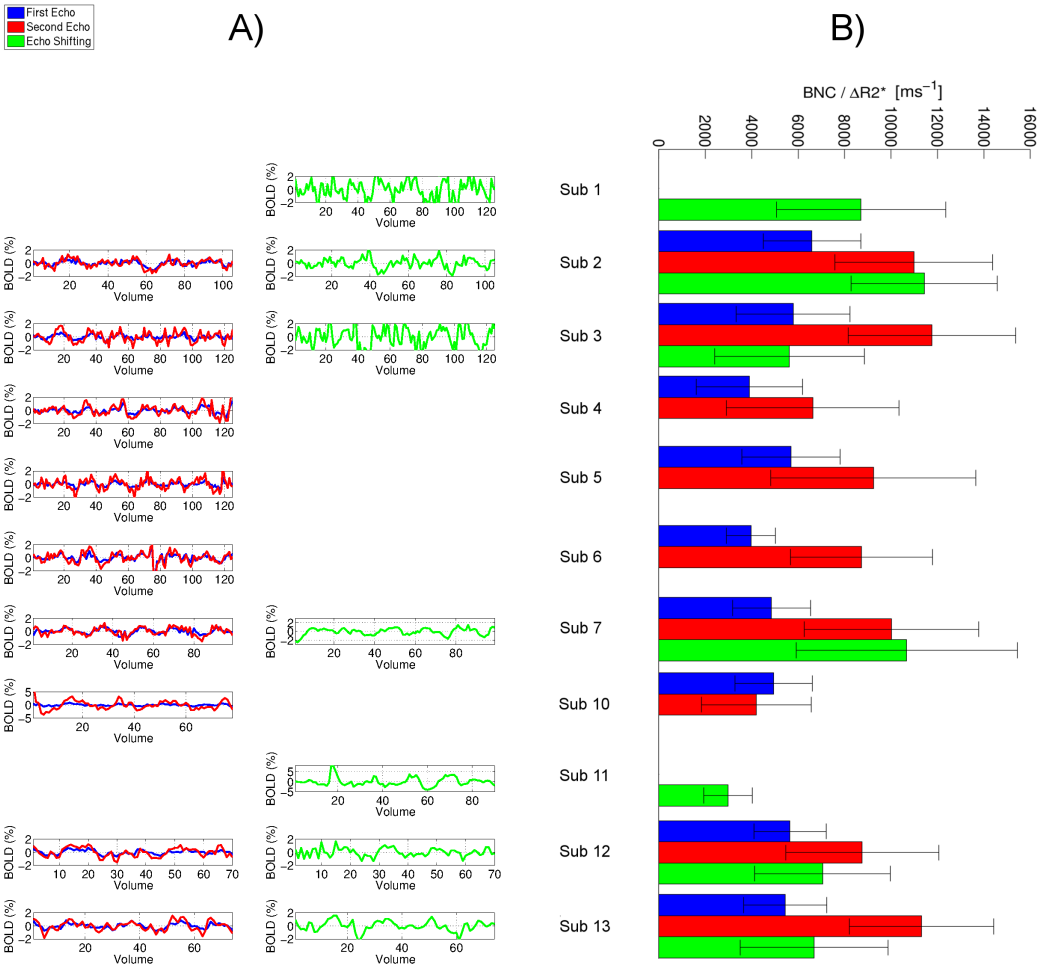

FIGURE 3.7: A) Left column: BOLD signal change over active clusters in the motor cortex converted in % signal change for each subject (rows). Blue plots correspond to the data acquired with an echo time of 25 ms, red 75 ms. Right column: BOLD signal change achieved with echo shifting. Plots that are not present correspond to data where there was either no activation or too much motion. B) BOLD to noise contrast (scaled by ΔR_2^*) in each subject. Data ordering follows Table 3.1.

Figure 3.7 (B) reports the BOLD to noise contrast within the active clusters for all subjects. Apart from subject number 10, there is a substantial increase in the second echo of all dual echo datasets, with the BOLD to noise contrast being roughly double than in the first echo. This increase follows the theoretical predictions - by hypothesising a basal T_2^* value of 120 ms [Rivkin et al., 2004], we get that the ratio $\frac{BNC_{75}}{BNC_{25}} = \frac{tSNR_{75}T_{E,75}\Delta R_2^*}{tSNR_{25}T_{E,25}\Delta R_2^*} = \frac{e^{-\frac{75}{120}}}{e^{-\frac{25}{120}}} \cdot \frac{75}{25} = 1.98$. Here, the $tSNR$

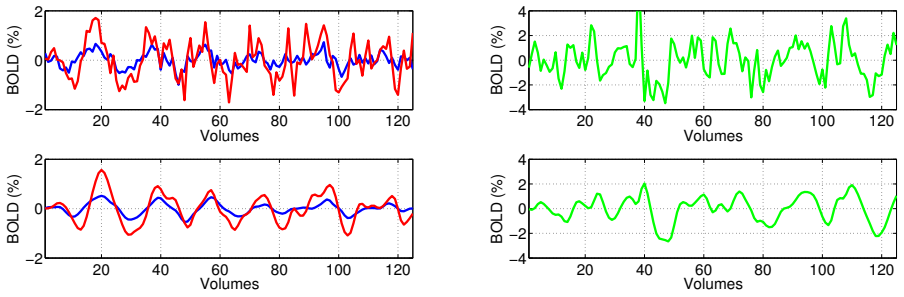

FIGURE 3.8: First row: dual Echo (first blue and second red) and es-EPI time courses (green) as in Figure 3.7 (A) for subject number 3. Second row: same data after low pass filtering.

Baby	First Echo	Second Echo	Echo Shifted
1	–	–	1.03 %
2	0.34 %	0.52 %	0.63 %
3	0.25 %	0.64 %	1.19 %
4	0.35 %	0.66 %	–
5	0.27 %	0.66 %	–
6	0.42 %	0.68 %	–
7	0.35 %	0.5 %	0.79 %
10	0.28 %	1.47 %	–
11	–	–	1.94 %
12	0.28 %	0.59 %	0.45 %
13	0.34 %	0.59 %	0.67 %

TABLE 3.2: Standard deviation of the BOLD signal in % for the 3 sequences in each subject. The symbol '-' indicates datasets with no detected activation.

is modelled as $\frac{S_0 \cdot e^{-\frac{T_E}{T_2^*}}}{\sigma}$, where S_0 is the available signal after excitation and σ the standard deviation of the noise time series. S_0 and σ are also assumed to be the same for both echoes.

Data from second echo of the multi-echo and echo-shifted acquisitions are also in partial agreement. The discrepancy, when present, can be explained by motion.

Figure 3.9 reports the BNC plotted against the standard deviation of the absolute displacement traces obtained from the GLM. Blue, red and green points correspond to dual echo and echo shifted datasets. A clear feature of the data is a significant linear trend in $\frac{BNC}{\Delta R_2^*}$ with the simple marker of the magnitude of the motion (R^2 of 0.54, 0.22 and 0.79 in each case). Figure 3.10 shows the BOLD

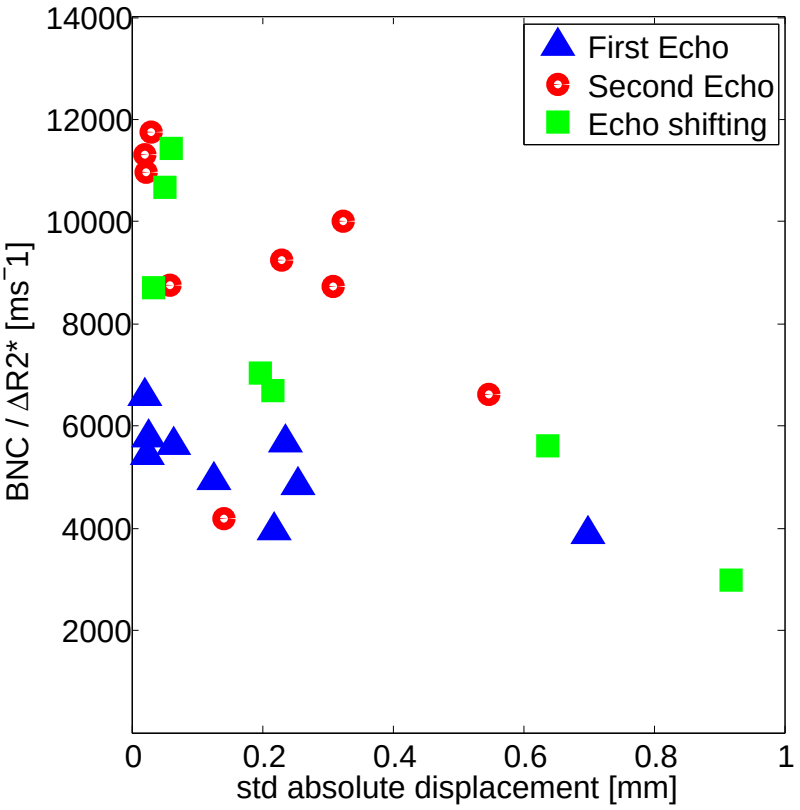

FIGURE 3.9: Standard deviation of the displacement field plotted against the BOLD to noise contrast (scaled by ΔR_2^*) for all subjects. Blue, red and green points correspond to dual echo and echo shifted datasets.

to noise contrast of Figure 3.7 (B) with the effect of motion factorized out. This was achieved by multiplying the data points of Figure 3.9 by the factor $\frac{b}{a \cdot x_{mot} + b}$, where a and b are the coefficients from the linear fit, and x_{mot} the variable in the horizontal axis in Figure 3.9. The BNC of echo shifted and second echo acquisitions are now in agreement. Furthermore, when comparing long to short echoes, an average increase of 78 $\pm$ 41 % in BNC was observed across all subjects.

We finally compared the z statistics from the GLM analysis. In this study, we do not observe significant differences between the z scores of first/second echoes and echo shifting (mean across all subjects 3.12 $\pm$ 0.35, 3.04 $\pm$ 0.21 and 3.03 $\pm$ 0.1).

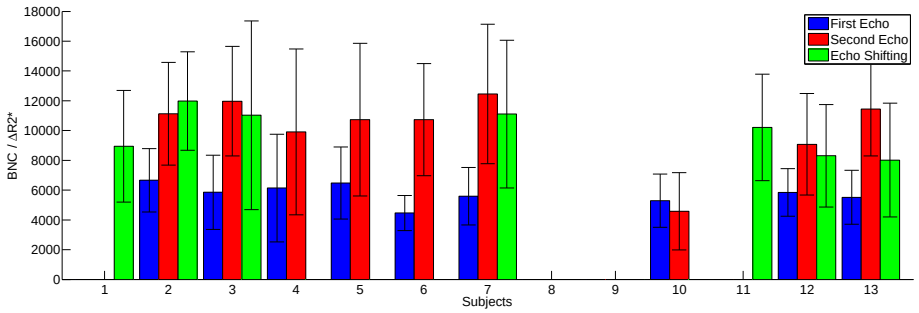

FIGURE 3.10: BOLD to noise contrast of Figure 3.7 (B) with the effect of motion factorized out.

3.4 Artefacts

3.4.1 Signal Loss

A problem that we have encountered when using echo shifting was the loss of signal at the boundaries between the brain and the air. At long echo times, spins within a voxel might indeed dephase substantially. What we observe in our data is that fMRI images at long echo times occasionally suffered from signal loss. Figure 3.11 shows one example, and more specifically data from a 33+2 weeks old premature baby at the short (a) and long (b) echo times. In (b), the Figure also overlays in yellow the edges of the brain from the short echo.

3.4.2 Fat signal

es-EPI does not include fat suppression.

Figure 3.12 reports an example of such artefact. The fat signal is clearly present in the data from the short echo (red arrows of Figure 3.12, a). Figure 3.12 (b) shows the corresponding es-EPI dataset. Here the fat signal is less prominent since its T_2^* is shorter. However, remaining components may be present.

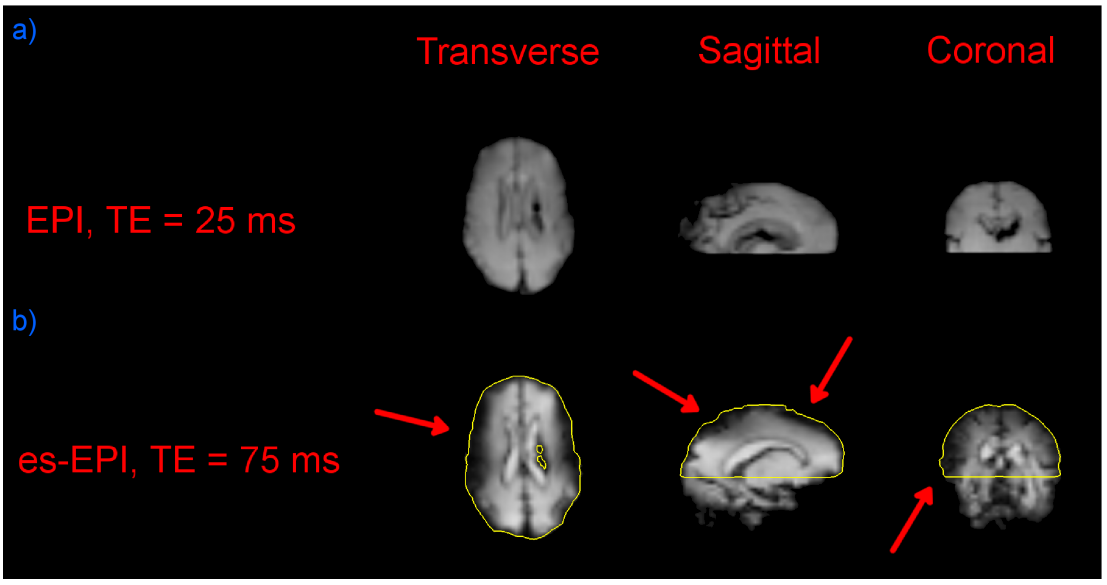

FIGURE 3.11: (a) Transverse, sagittal and coronal views of a 33+2 weeks old premature baby scanned with 2D-EPI (echo time of 25 ms). (b) es-EPI data. Red arrows indicate zones affected by signal loss.

Including fat suppression with echo shifting is possible. If implemented, the refocusing gradient would simply have to compensate for the slice selective gradient of the fat suppression pulse. Initial experimentation has provided information that suggests that this is feasible. However, this would take up to 10 ms per slice, therefore increasing the minimum repetition time.

3.5 Conclusions

This chapter investigates the possibility of increasing the echo time T_E via the use of es-EPI to match the longer T_2^* of developing brain tissue without sacrificing sampling rate. The effectiveness of the sequence was tested on a series of task fMRI experiments run on preterm and term equivalent babies. Dual echo EPI data with identical readout structure to es-EPI was also acquired and used as control data to assess BOLD to noise contrast. The use of a task based approach is challenging in the neonatal population, but offers the advantage of creating consistent activation conditions across runs in the same subject.

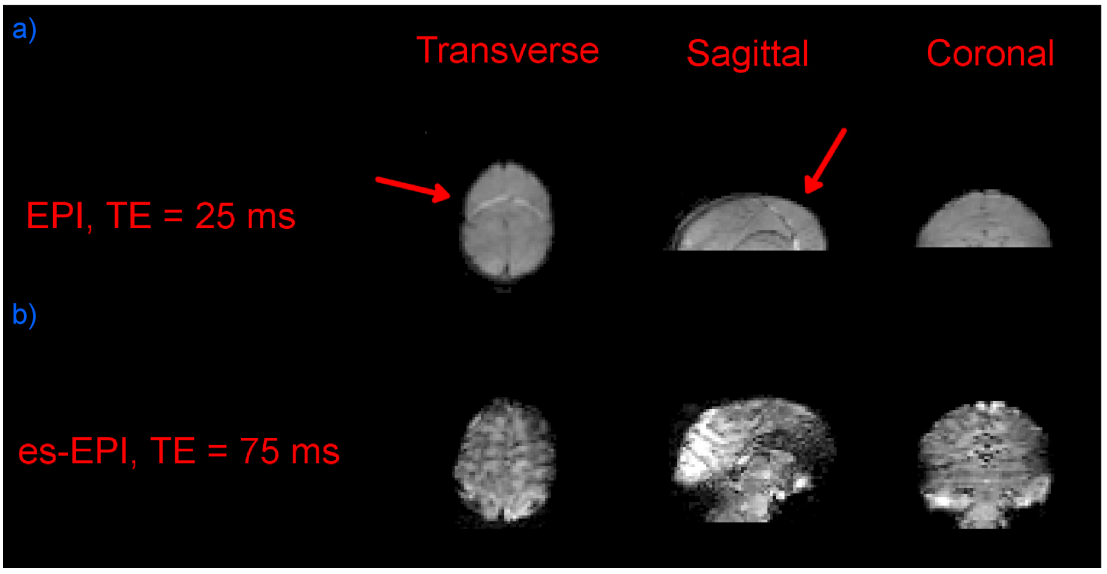

FIGURE 3.12: a) Transverse, sagittal and coronal views of a 40+5 weeks old baby scanned with 2D-EPI (echo time of 25 ms). The fat is indicated by the red arrows. (b) es-EPI data.

The equivalence between the properties of es-EPI and the second echo of the dual echo EPI signal was assessed using a phantom. The result from that test suggested that a shift of the signal along the three orthogonal directions x, y and z is the safest to achieve good suppression.

The choice of performing a task based fMRI experiment as opposed to gathering resting state data enabled the identification of a specific signal change following stimulation which could be quantified and therefore compared between the different sequences. Having a model able to predict the BOLD response proved indeed to be important when trying to separate useful signal from other sources. However, the advantages offered by echo shifting in neonatal and fetal fMRI should remain the same with resting state data.

The task activation experiments were extremely challenging, particularly as there was a need to perform two task activation runs and motion was not predictable. The baby could furthermore wake up or cry during acquisition and its safety and comfort were obviously the first priority.

Motion is a common problem in neonatal fMRI. In this study, motion corrupted frames were removed from the fMRI time series. Head motion is known to be a significant source of bias and inaccuracy in fMRI data analysis, and when not appropriately accounted for can lead to false positive results and artificial patterns of correlation [Power et al., 2012]. As the aim was to assess BOLD to noise contrast, we could not reliably trust segments of data with motion. However, discarding data decreases statistical activation power. Furthermore, several other factors may have contributed to some of the experiments not working. These include technical difficulties or habituation effects [Poellinger et al., 2001]. In this study, the scanning order of echo shifting and dual echo EPI was fixed. It remains to be assessed whether a randomized approach would have been more beneficial in terms of BOLD signal detection.

Nonetheless, 5 examples were obtained consistent with the proposition that echo shifting does allow access to longer echo times without loss of temporal efficiency. Furthermore, when successful, dual echo experiments generally provided fMRI data with increased BOLD to noise contrast.

Despite an increase in BNC, the z scores did not change.

Chapter 4

Echo Volumar Imaging of the fetal brain

4.1 Motivation

Echo Volume Imaging (EVI) is an extension of the well-known EPI sequence that allows the acquisition of a whole fMRI volume following a single RF excitation; this leads to a repetition time T_R in the order of a few hundreds of milliseconds depending on the field of view and image resolution. The main benefits are increased temporal resolution and robustness to motion. The downside is that EVI is extremely sensitive to $\mathbf{B}_0$ field inhomogeneities and T_2^* signal decay limits the achievable image quality; these factors have so far limited the usage of EVI in functional neuroimaging.

However, the maternal tissue offers a potentially optimal environment for EVI since $\mathbf{B}_0$ field inhomogeneities are much less pronounced than in adult fMRI experiments because of the lack of air-tissue boundaries within the fetal head and the womb. Furthermore, T_2^* values were recently measured across the fetal brain and shown to be much longer than in the adult brain [Vasylechko et al., 2014], paving the way for EVI applications.

EVI was firstly introduced by Mansfield [1977] and the first implementation can be attributed to Song et al. [1994].

The aim of this last study was to reduce the impact of physiological noise [Triantafyllou et al., 2005] in the fMRI time series by considerably enhancing the acquisition sampling rate. The increase in temporal resolution that can be achieved with EVI is indeed outstanding: for example, in Song et al. [1994], the readout duration was only 70 ms and the repetition time T_R was purposely set to 1 second to avoid signal saturation. Nonetheless, the authors acknowledged the main limitation of the sequence which was the heavy hardware demands imposed on the gradients. Another feature of EVI is that it is highly sensitive to off-resonance effects and this manifests mainly along the slowest phase encoding direction. A careful shimming technique is therefore essential.

The first functional EVI study was performed in Yang et al. [1997]. In this study, a dedicated localized echo volumar experiment was designed and used to acquire data from a healthy volunteer at 1.5T, attaining a resolution of $3.75 \cdot 5 \cdot 5$ mm^3 with a FOV of $240 \cdot 45 \cdot 45$ mm^3. The imaging target was the superior part of the motor cortex and the sensitivity of the sequence to the BOLD effect assessed via a finger-tapping paradigm. Activation was demonstrated in the contralateral primary sensorimotor cortex. In Van der Zwaag et al. [2006], an Echo Volumar sequence that made use of a high gradient switching frequency and outer volume suppression was implemented. Rewinding blips reduced ghosting and image distortions along the slowest phase encoding direction. The reported repetition time was 167 ms. In Rabrait et al. [2008], the extent of image distortions was reduced by combing EVI with parallel imaging techniques. Two human subjects were scanned at 1.5T using a slow event auditory paradigm. Almost full brain coverage was obtained with a repetition time of 200 ms and this allowed both the hemodynamic response function over the entire field of view to be measured and active regions in the auditory cortex to be localised.

In this chapter, we present exploratory work in which we implemented and tested various options for an EVI readout paired to localised excitation [Nehrke et al., 1999, Pauly et al., 2011] of the fetal brain. A key issue for EVI is the very long echo train that is needed to encode the full volume and this is particularly a challenge when imaging the fetal brain in the context of the maternal anatomy, which occupies a large field of view. Therefore, a localised excitation approach was adopted to achieve control over the volume that has to be spatially encoded. The method uses a special RF pulse and gradient waveforms to excite a tight cylinder centered on the fetus. A 3D readout is then used to encode only this narrow region.

4.2 Material and Methods

4.2.1 The EVI sequence

To achieve EVI, an existing multi-echo EPI sequence was modified. The sequence is schematically represented in Figure 4.1 (A); pencil beam (PB) excitation gradients and RF pulse waveform are shown in blue. These excite a cylindrical column [Pauly et al., 2011] aligned with the foot-head (FH) axis. A multi-echo EPI gradient pattern with readout along this axis and primary phase encoding (PE) along the right-left (RL) was augmented by extra PE gradients on the anterior-posterior (AP) axis (shown in red) to achieve EVI encoding.

The k-space acquisition trajectory of EVI is shown in Figure 4.1 (B). For consistency with earlier material on EPI, the k-space axes are defined with k_x along the readout direction, and k_y along the primary phase encode. k_z is the second phase encode. To help the reader, corresponding time-points in the sequence are highlighted in (A) and (B) with numbers. The number of k_y blips was kept odd. This reduces ghosting along the second phase encoding direction as consecutive k_z planes are traversed following identical paths [Van der Zwaag et al., 2006].

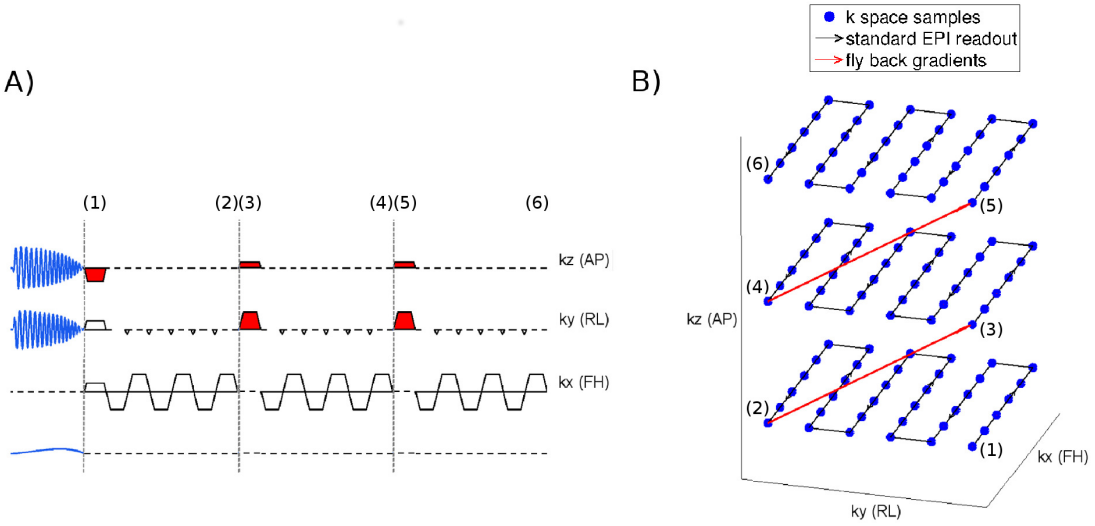

FIGURE 4.1: (A) An EVI sequence with localized excitation. Gradients not in scale. (B) EVI k-space acquisition trajectory.

4.2.2 Acquisition Protocol

Running an EVI sequence during fetal examinations turned out to be a challenging task since there was no scanner reconstruction software able to interpret the data and to correctly reconstruct an image on the fly. To have the entire set of variables under control and to make sure that everything was running properly, a lot of effort was therefore spent in designing an acquisition protocol in which supporting data was progressively acquired to build confidence that the examination was correctly progressing towards a successful EVI acquisition, which would remain unconfirmed until after the examination was completed. Eventually, we decided on the following acquisitions for when performing an EVI experiment on fetal subjects. However, this detailed description refers only to the first set of images acquired from the first fetal examination, and there are differences from phantom to in vivo acquisitions.

1. **Standard Survey and Reference scans.**

2. **Initial B_0 map to perform image based shimming:** $5 \cdot 5 \cdot 10\ mm^3$ resolution scan for a field of view of $320 \cdot 320 \cdot 150\ mm^3$ with $\Delta T_E = 2.3\ ms$.

3. **3D-EPI large field of view:** $2 \cdot 2 \cdot 3\ mm^3$ high resolution scan for a field of view of $320 \cdot 320 \cdot 150\ mm^3$. 3D-EPI is a multishot gradient echo sequence whose design lays in between 2D-EPI and EVI [van der Zwaag et al., 2009]. A schematic representation of its gradient waveforms is given in Figure 4.2. In this example, the excitation pulse is a pencil beam as required for step 4 below. However, for this step, a conventional slab selective pulse was used. After the application of each RF, phase encoding blips are applied along the through slice direction and data is encoded along the third dimension (in red). Furthermore, after the end of each readout, crushing gradients are also applied (in yellow).

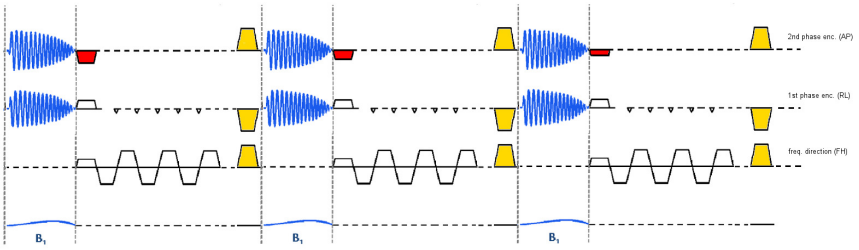

FIGURE 4.2: A 3D EPI sequence with localized excitation. Gradients not in scale.

The advantage of 3D-EPI over the 2D case is a detectable increase in SNR since each voxel is formed by complex weighting of signal coming from n shots instead of just one. However, this sequence is more prone to motion induced artefacts that may happen between shots.

4. **3D-EPI large field of view with localized excitation:** The excitation pulse is modified to achieve pencil beam excitation (as shown in Figure 4.2). The flip angle is 15° and the diameter of the beam 70 mm.

5. **3D-EPI small field of view and coarse resolution with localized excitation:** Field of view and resolutions are matched to the a desired EVI readout (scan 7). The echo time T_E is also matched.

6. **3D-EPI small field of view and coarse resolution with localized excitation and odd number of phase encodes:** The default behaviour of Philips scanners for multi echo EPI-like sequences is to keep the number phase encodes even. This represents a potential issue in EVI, since an odd number of phase encodes is preferable [Van der Zwaag et al., 2006]. This was achieved by using a Partial Fourier acquisition and by excluding the very last phase encode line of each $k_x k_y$ plane. It is also important to notice that, from this point onwards, it was not possible to reconstruct images using standard Philips reconstruction software and that in house Matlab reconstruction scripts were used.

7. **EVI with localized excitation:** We finally changed the structure of the sequence to perform EVI. Different combinations of resolutions were used. However, the fetal data was acquired with a 5 mm isotropic resolution. Furthermore, by having matched the EVI sequence bandwidth, resolution and echo time to the 3D-EPI scans 5 and 6, a direct comparison between these datasets was always possible.

4.2.3 Phantom Experiments

To test the sequence and the reconstruction procedure, a spherical phantom flask was filled with a solution made of 0.5% agarose gel (0.02% sodium azide as biocide/anti-fungal) so that T_2 and T_1 are nominally long.

However, the phantom turned out to have strong $\mathbf{B}_1^+$ inhomogeneity and the actual flip angle always exceeded the one prescribed. To prevent this, the slice excitation profile was measured under the assumption that the flip angle of a standard slab excitation pulse coincides with pencil beam excitation. Therefore,

after switching the phase encoding gradients off, a standard EVI readout was played out. The read direction was changed from FH to AP and the sequence was repeated using flip angles of 15, 30, 60 and 90°.

Another encoding parameter was investigated in order to assess the quality of the excitation pulse, which is the ratio between encoded versus excited regions along the slice direction.

After having selected the slice excitation parameters, we started an extensive period of testing. The image reconstruction was performed with in house Matlab scripts able to process Philips raw data. Ghost correction along the primary phase encoding direction was either achieved using a self-reference method as proposed in Buonocore and Gao [1997], or calibration data. Data was either acquired using an 8 or 32 head channel coil. Data from each coil was combined with simple sum of squares.

4.2.4 In vivo Echo Volume Imaging, first attempt on adults and on the fetus

The data used in this section comes from 3 healthy adults (males, age range: 24 to 33 years) and 1 fetus (gestational age of 30+4 weeks) who had been assessed as normal. Informed consent was obtained for all examinations. Scans were performed on a Philips (Best, the Netherlands) Achieva 3T scanner with 32 channel receiver coils – a head coil to image the ventricles in adult brain and a cardiac torso coil for fetal imaging. The ventricle region was chosen to ensure a good shimming and long T_2^*.

To achieve maximal encoding rate, ramp sampling was used on the EVI readout with 0.377 ms required per data line. Prior to testing on a fetus, the acoustic noise produced by the sequence was measured using a calibrated MR compatible microphone, but the sound level exceeded established local guidelines. A coarser

resolution was therefore adopted allowing lower gradient amplitudes for the fetal test leading to a readout window per k-space line of 0.355 ms. For all localised acquisitions, the FOV was $200 \cdot 100 \cdot 100$ mm^3, with an excited PB diameter of 70 mm and 15° flip angle. The FOV was encoded at a resolution of $3.5 \cdot 3.5 \cdot 3.5$ mm^3 for the adult scans (matrix size $56 \cdot 28 \cdot 29$, total readout time 348 ms) and $5 \cdot 5 \cdot 5$ mm^3 for the fetus (matrix size $40 \cdot 18 \cdot 20$, total readout time 154 ms). For comparison, multi-shot 3D-EPI images (29 shots with $T_R = 500$ ms for the adult cases and 20 shots for the fetus) with matching FOV and resolution to the EVI images were also acquired with a T_E of 80 ms. Furthermore, to provide a visual anatomical reference to the adult cases, high resolution 3D multi-shot EPI images were acquired with a FOV of $240 \cdot 200 \cdot 240$ mm^3, resolution of $2 \cdot 2 \cdot 2$ mm^3 and T_E of 80 ms. To minimize geometric distortions in all acquisitions, image based shimming [Schneider and Glover, 1991] was performed over the adult and the fetal brains and the shim values kept the same throughout the exam.

After reconstruction, data was corrected for geometric distortions as presented in chapter 2: along the RL direction for the 3D-EPI data and considering only the slower PE direction for EVI.

4.2.5 Shimming

During this first fetal EVI experiment, the shimming process failed and the resulting $\mathbf{B}_0$ field was not homogeneous enough for EVI. A possible explanation was that a very small region encompassing the fetal head was used to shim, which may have led to a sub-optimal solution elsewhere within the PB volume. Furthermore, since the fetus was moving substantially between sequences, it could have moved outside the shimmed area. However, on further investigation, it emerged that the shimming code, although fully functional for head imaging with the subject in one fixed location and a standard orientation, failed to account for changes in bed position and for the different options for patient orientation.

All the work that is presented here has been carried out in partnership with Andreia Gaspar and Anthony Price. More specifically, all the infrastructure needed to perform image based shimming was implemented by Andreia. However, the following considerations and measurements were performed together and they are very relevant here. The Image based shimming code consists of a series of Matlab functions that can import and handle PAR/REC Philips field maps. The program is available to run in a computer next to the main console and the two are interconnected. After signal acquisition, the field maps are fed into the program that calculates appropriate shim values. Shim values are then sent to the scanner and used during the following acquisitions.

Initial attempts were unsuccessful and this was tracked down to a problem in the geometry definition - the program was not able to handle images that were acquired under arbitrary positions and orientations and that, actually, the only configuration for which it would have worked was when images were acquired as supine head first. In our local fetal imaging practice, however, the mothers are positioned feet first as this has been found to be most acceptable to them and it minimises claustrophobic effects.

The code was therefore extended in order to deal with all possible combinations of patient positions and orientations. Furthermore, as the PAR/REC header does not incorporate table displacements, the EVI sequence was modified so that it could print its position to an external file every time a new field map was acquired.

4.2.6 Acoustic Noise

The acoustic noise produced by EVI was too loud to be used routinely in a clinical set up. Furthermore, while the mother's auditory system can be protected with adequate padding, nothing can be done to protect the fetus. Fetal ears are also developing in utero, and we don't want to do anything that could possibly harm this process. Luckily, the maternal tissue offers a natural environment for sound

attenuation: before reaching the fetal auditory system, sound waveforms have to pass through the maternal abdomen and the uterus. This results in considerable sound attenuation; moreover, as low sound frequencies carry more power, they penetrate more than high frequency noise. Gerhardt and Abrams [1996] measured the sound in the uterus of pregnant sheep. What was found was an attenuation of low frequencies (less than 500 Hz) of 5 decibels (dB) and from 20 to 30 dB above 500 Hz. There have been other studies that tried to measure the attenuation in the human womb. For example, Richards et al. [1992] placed a hydrophone in the maternal uterus and played low and high frequencies from a stereo speaker placed close to the abdomen. On average, the attenuation was of -3.7 dB (noise amplification) for low frequencies, but reached a maximum attenuation of 10 dB for sounds at 4 kHz. In contrast, Glover et al. [1995] estimated an attenuation of 30 dB in the sound perceived by the fetus during an MR scan. Reeves et al. [2010] investigated whether the fetal hearing exposure to MR is associated to cochlear injury after birth, and significant impairments were not observed. Furthermore, as the fetal auditory system is not yet well developed in the uterus and since the amplification of the human pinna is not functioning during pregnancy, the actual sound perceived by the fetus seems to diminish even further [Gerhardt and Abrams, 1996].

Our research group has local guidelines for noise assessment. Even though the maternal tissue attenuates noise, it is crucial that all scans are strictly within these limits. We have therefore systematically tested the noise produced by EVI. The measurements were performed with a MR compatible microphone that was placed at isocenter in the scanner. Three different set of measurements were taken. These are defined by the manufacturer (castle microphone GA 221):

1. **leq dBa:** measure (in dB) of the acoustic noise averaged across a certain amount of time.

2. **peak dBa:** measure of the maximum acoustic noise (in dB).

3. **peak linear:** measure of the maximum acoustic noise (in dB) with linear weighting.

We performed the first set of measurements on the 5 and 3.5 mm isotropic EVI sequences of section 4.2.4. Measurements were performed by modifying the repetition time T_R from 500 to 1000 ms. As the RF pulse interacts with the microphone, it was necessary to turn it off prior to each measure.

There are 2 parameters that can be adjusted in order to decrease acoustic noise. These are the *slew rate* and the *maximum gradient strength*. Options include reducing the slew rate to the minimum value and to allow the gradient strength to be maximal, achieving a gradient waveform very much like a sawtooth function, or instead to do the opposite achieving a blocky waveform. These adjustments change the noise in the bore, but at the time of the study there were no tools available to reliably predict the outcome of a change. A practical approach was therefore adopted in which a range of options were tested for acoustic output and the best slew rate/gradient strength combination was selected.

Although initially acoustic measurements were obtained with the microphone at the scanner isocenter, this required switching the RF system off to avoid interference to the measurement equipment. It was found that there were problems in restoring the scanner to its normal configuration after this procedure and so, in order to be able to make systematic measurements, a strategy of placing the microphone in a fixed location away from the RF transmit coil was adopted. Moreover, prior to performing the measurements, the flip angle was always set to the minimum allowed value of 1°. By repeating measurements of sequences already assessed but with the microphone in the new position, it was determined that there was a fixed difference of about 20 dB, which was then used as a conversion factor.

4.2.7 Multi echo acquisition

Given a selected readout structure, we assessed how many k_z planes could be acquired without observing signal loss.

A fetus of 30+1 weeks underwent a 3D multi echo EPI acquisition with resolution and field of view matched to EVI. The first echo occurred at 11 ms and the subsequent echoes every 21.8 ms. A total of 20 echoes were acquired with PB excitation (70 mm beam diameter and flip angle of 45°). Resolution was 3.5 mm isotropic.

4.2.8 Echo Volume Imaging on the fetus, second and third attempts

The sequences designed in the previous paragraphs were used to image a 28+5 weeks old fetus. As anatomical reference, a T_2 weighted ssFSE image was also acquired. k-space samples acquired within 55 ms from the excitation were excluded (the reason for this will be given in the results section). Furthermore, those coils that did not provide signal because of being too far apart from the fetal head were excluded. Partial Fourier acquisition [Margosian et al., 2007] along the third direction was used to shorten the readout. Images were reconstructed by firstly depriving the data from its phase and then by applying the conjugate symmetry rule.

A new acquisition varying the flip angle was also tested - in all our previous EVI attempts, the flip angle was purposely set to 15°. This choice was originally adopted because of the $\mathbf{B}_1^+$ properties of the phantom that we had used to test the sequence. The bladder of an adult volunteer was chosen as imaging target and scanned with EVI. This is because the long T_2^* in this region. Imposed flip angles were 15, 30, 45, 60 and 75°. To assess the strength of the signal, the 20% top highest voxels were used to calculate the mean signal within the bladder.

The third and last fetal EVI acquisition used a flip angle of 45° (chosen from the previous test) and it was run on a 35+1 weeks old fetus.

4.3 Results

4.3.1 Phantom Experiments

The slice profiles obtained during the phantom experiments are shown in Figure 4.3 (a), where we plot the data obtained by averaging each k-space line after Fourier transforming along the AP direction. It can be clearly seen that for flip angles 60° and 90°, the central part of the slice profile starts to drop. To ensure a good excitation profile, we therefore decided to use a flip angle of 15° and this value was subsequently maintained in all phantom experiments.

The results obtained by varying the encoded versus excited ratio are shown in Figure 4.3 (b), where we plot different slice profiles. It can be observed that, for example, a ratio of 0.7 results in a strong wrap. We finally decided to use a ratio of 1.2, which is the standard value for Philips and that ensures the flattest profile while also being efficient in terms of minimising the excess encoded volume beyond the useful signal region.

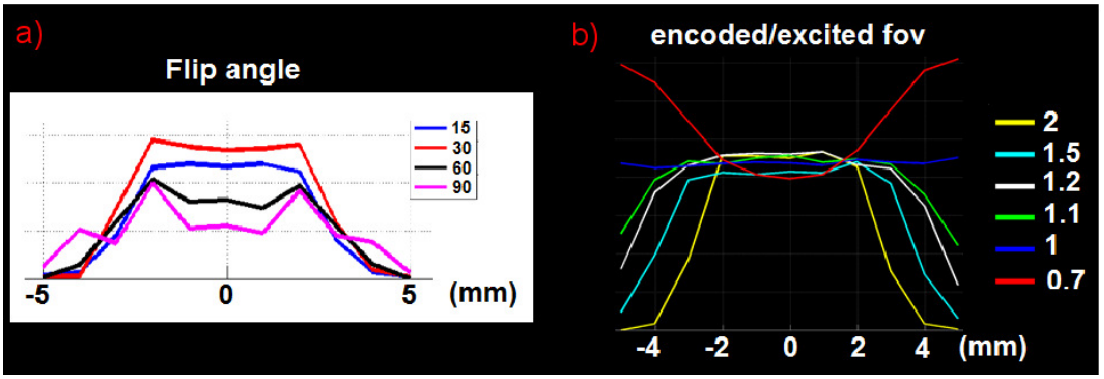

FIGURE 4.3: (a) Slice profiles as measured on a spherical phantom for increasing flip angles. (b) Slice profiles for different encoded versus excited ratios.

Examples of 3D-EPI and EVI data with pencil beam excitation from one of our successful experiments are shown in Figure 4.4. The first row is a reference 3D-EPI scan of the spherical flask acquired with a resolution of $4 \cdot 4 \cdot 3\ mm^3$ and large field of view of $200 \cdot 200 \cdot 210\ mm^3$. The second row is a 3D-EPI scan of the same flask at a resolution of $4 \cdot 4 \cdot 7.36\ mm^3$ and field of view of $200 \cdot 77 \cdot 81\ mm^3$. A pencil beam excitation excites a cylinder of 30 mm diameter along the FH direction and T_E is 10 ms. The third row shows an equivalent EVI experiment with geometry and resolution matched to the previous case. Prior to encoding, the same excitation pulse is used and T_E is roughly 50 ms.

4.3.2 In vivo Echo Volume Imaging, first attempt on adults and on the fetus

Acquisitions were successful in all three adult volunteers and in the fetal brain, although the quality of the achieved shim was poorer in the latter case; for example, for one of the adults, the standard deviation of the residual field (converted into frequency) after image based shimming was $\pm 30\ Hz$ within the brain, whereas in the fetal case this value was $\pm 46\ Hz$.

Figure 4.5 shows the images from the same adult subject along the three orthogonal planes for high resolution 3D-EPI images with standard excitation (A) and with PB excitation (B), 3D-EPI image with $200 \cdot 100 \cdot 100\ mm^3$ FOV and 3.5 mm isotropic resolution (C), and matching EVI (D). Distortion correction was performed on all of these acquisitions enabling geometrical matching of the EVI to the 3D-EPI acquisitions. The fetal images (three orthogonal planes) are displayed in Figure 4.6 and include: a single-shot multi-slice Fast Spin Echo T_2-weighted anatomical image as reference (A), the standard 3D-EPI image with localized excitation (B), the equivalent EVI image prior to (C) and after applying geometric distortion correction (D). Although the resolution of the images is coarser than

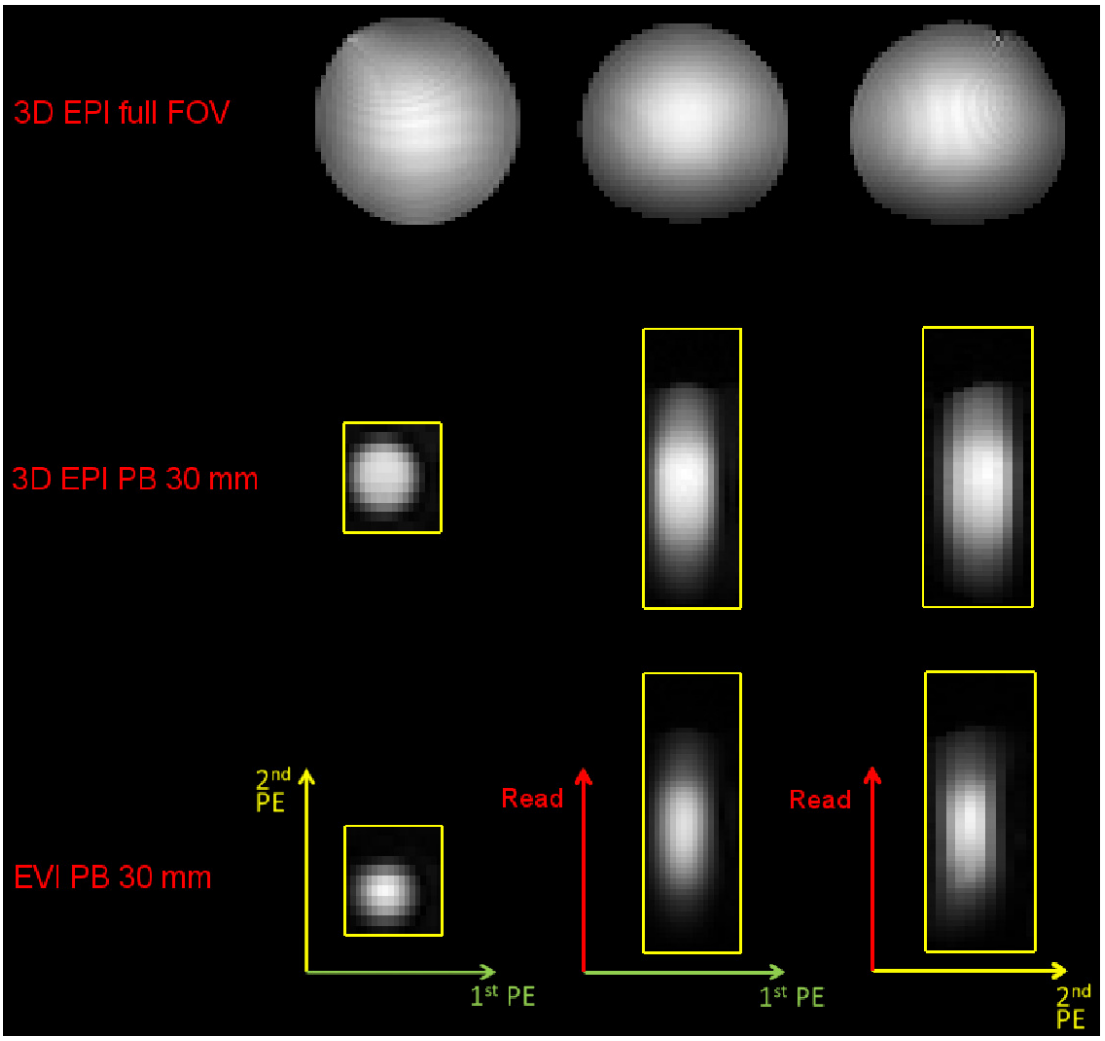

FIGURE 4.4: The first row represents a reference 3D-EPI scan of spherical flask. The second row is a 3D-EPI scan using pencil beam excitation and a reduced FOV. The third row shows an equivalent EVI experiment with geometry and resolution matched to the previous case. Second and third rows outline in yellow the edges of the FOV together with read, 1^{st} and 2^{st} phase encoding directions.

the adult equivalent, it is still possible to identify the mother's bladder (white arrow) and the fetal brain (red arrow).

4.3.3 Shimming

Figure 4.7 (a) (first row) shows an example of a coronal field map from a bottle phantom acquired as feet first. The field of view was purposely rotated around

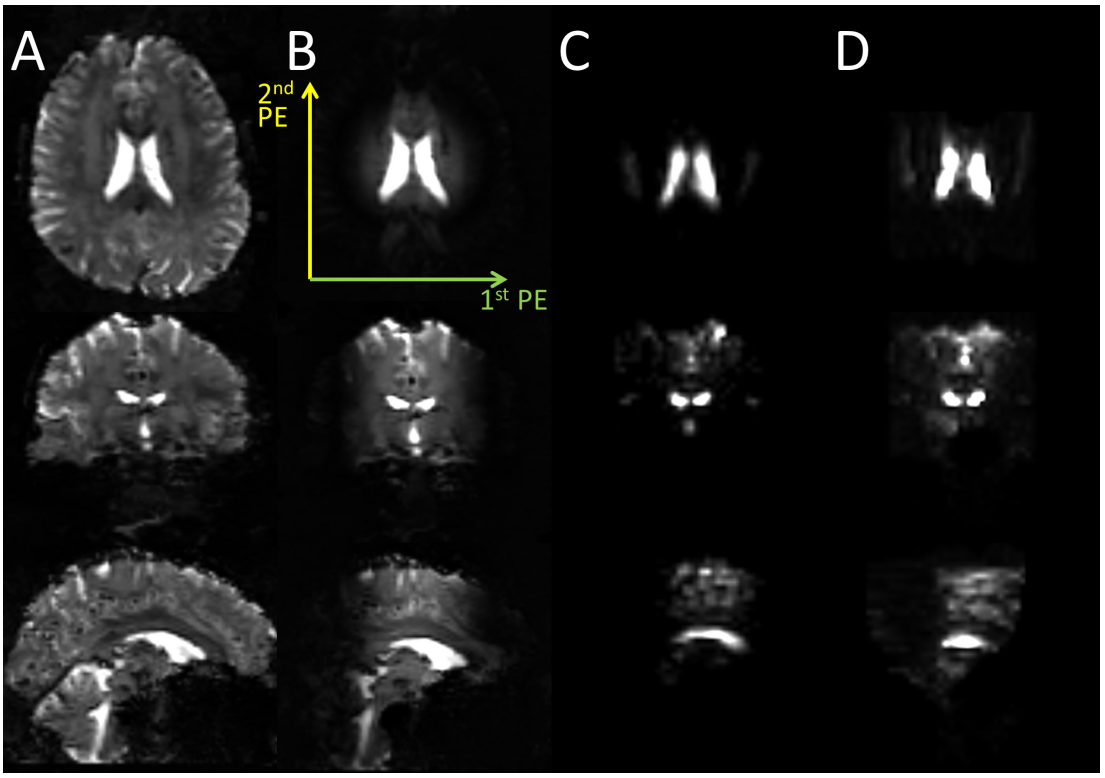

FIGURE 4.5: Example of adult images. (A) 3D-EPI with large FOV. (B) 3D-EPI with large FOV and PB excitation. (C) 3D-EPI with small FOV and localized excitation. (D) EVI with PB excitation. Phase encoding directions indicated in green (1^{st}) and yellow (2^{nd}).

the AP, FH and RL axes of angles 10, 40, 19.47° and the table net displacement z_0 from laser calibration was $-50\ mm$. The predicted field map from the image based shimming procedure is shown in the second row. The measured residual field after shimming is shown in the third row and the two coincide. Figure 4.7 (b) shows their frequency distributions.

4.3.4 Acoustic Noise

Acoustic noise measurements with the default values for slew rate and gradient strength (180 $\frac{mT}{m \cdot s}$ and 30 $\frac{mT}{m}$) are given in Table number 4.1. Local guidelines consider a sequence to be noisy if the leq dBa parameter exceeds **105 dB**. All of the sequences exceed this limit. The average noise decreases as the repetition

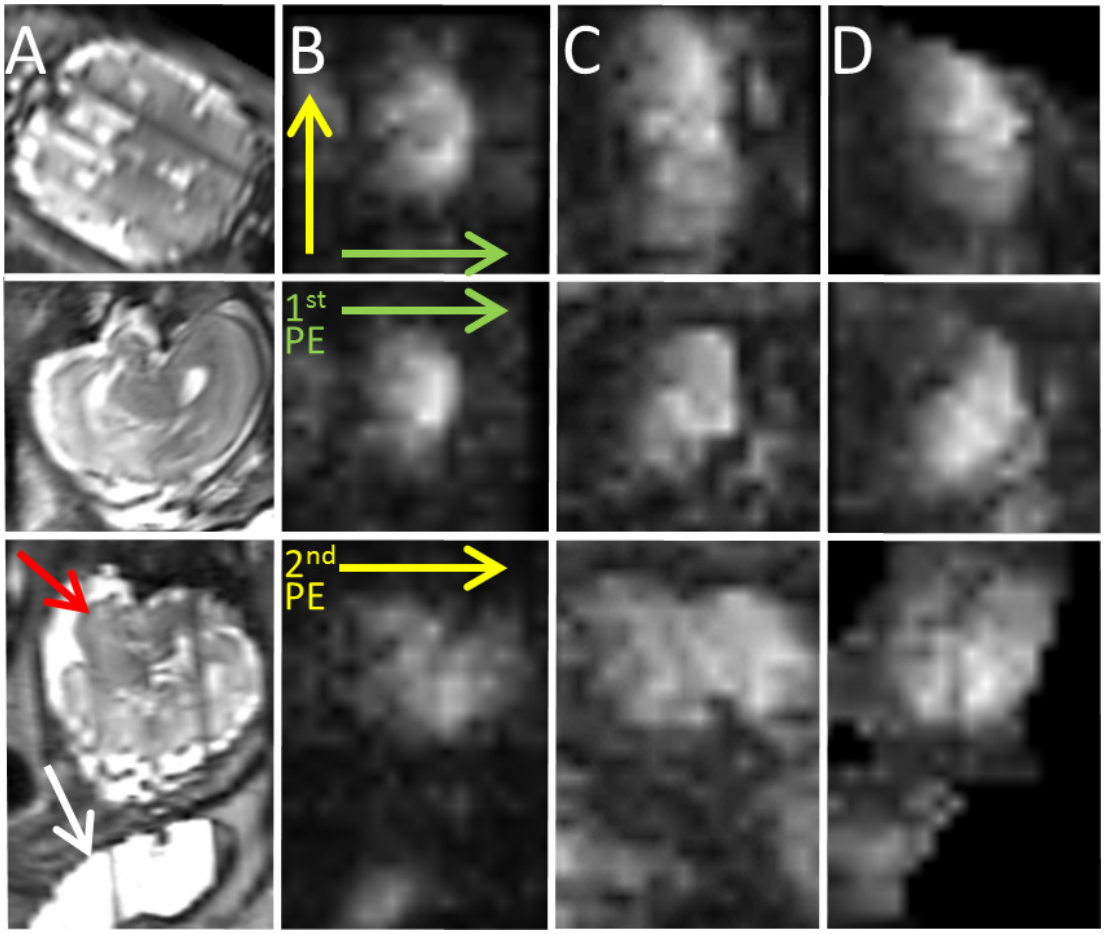

FIGURE 4.6: Fetal images along orthogonal planes: (A) anatomical T_2 weighted image showing the fetal brain (red arrow) and the mother's bladder (white). (B) 3D-EPI with PB excitation. (C) EVI. (D) EVI after distortion correction along the slow phase encode direction. Phase encode directions shown in green (fast) and yellow (slow).

time increases since there is more dead time between subsequence pulses and the readout structure has not changed. However, peak noise remains the same. Noise increases as the acquired resolution increases.

After all these measurements were taken, we decided not to investigate the 5 mm isotropic sequence any further.

All acoustic measurement data quoted from this point on were obtained with the microphone at the edge of the room. At this new position, leq dBa, peak dBa, and peak linear are 103, 104.8 and 117.8 dB for the 3.5 mm isotropic sequence.

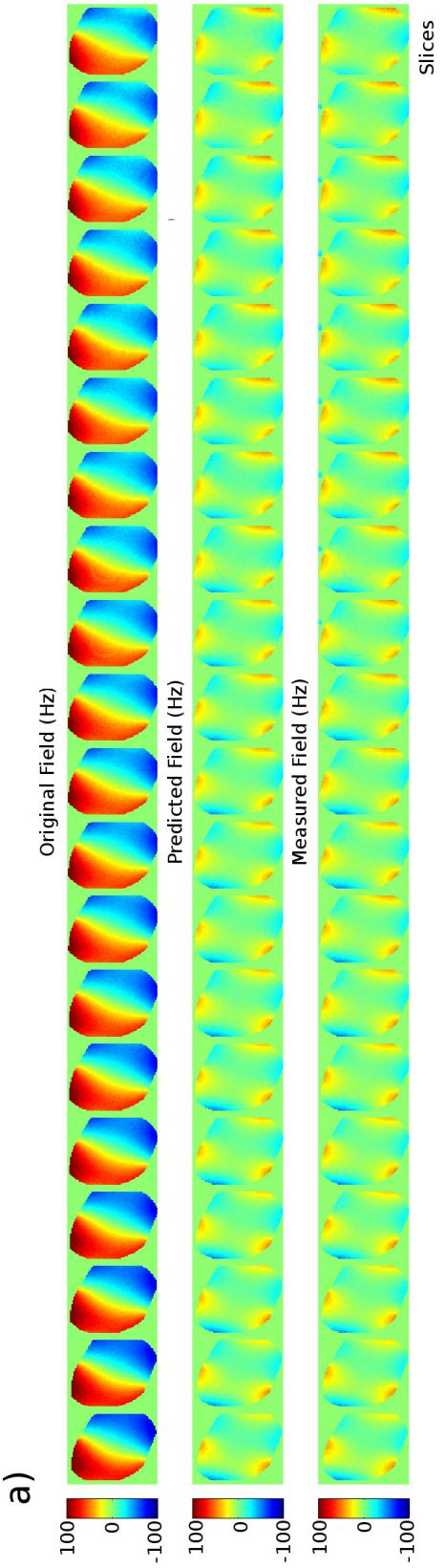

FIGURE 4.7: (a) The first row reports the original inhomogeneous B_0 field as measured in a bottle phantom. Second and third rows report the predicted and measured B_0 field after image based shimming. Images were acquired as coronal and patient position was feet first. The field of view was rotated around the AP, FH and RL axes of angles 10, 40, 19.47° and the table net displacement z_0 from laser calibration was -50 *mm*. (b) Frequency distributions of original (Left), predicted (Center) and measured (Right) B_0 fields - standard deviations are also highlighted in dash-blue.

T_R (ms)	Res. (x, y, z) (mm^3)	leq dBa (dB)	peak dBa (dB)	peak linear (dB)
500	$5 \cdot 5 \cdot 5$ $3.5 \cdot 3.5 \cdot 3.5$	115.6 123.7	118.3 124.6	131.9 136.4
700	$5 \cdot 5 \cdot 5$ $3.5 \cdot 3.5 \cdot 3.5$	113.4 122	117.7 124	131.9 135.6
1000	$5 \cdot 5 \cdot 5$ $3.5 \cdot 3.5 \cdot 3.5$	111.6 120	117.1 124.1	131.8 136.3

TABLE 4.1: Noise measurements taken from the standard EVI sequences at different resolutions for increasing repetitions times.

As expected, there is an attenuation of about 20 dB between the bore and the edge of the room.

Several combinations of slew/strength were tested and, for the 3.5 mm sequence, two quiet solutions existed. The first (sequence **A** of Table 4.2) had a slew rate of 60 $\frac{mT}{m \cdot s}$ and gradient strength of 30 $\frac{mT}{m}$, resulting in a noise of 92.9, 93.2 and 109 dB. If compared to the previous case, there is an attenuation of almost 12 dB. The second solution (sequence **B** of Table 4.2) was even quieter, and it was found with slew and strength of 25 $\frac{mT}{m \cdot s}$ and 20 $\frac{mT}{m}$. These measurements provided 88.1, 88.5 and 107.2 dB for leq dBa, peak dBa, and peak linear.

We also compare these measures with the noise produced by the 2D-EPI sequence that had been used to acquired fetal resting state fMRI data in chapter 2. This sequence has always been regarded as quiet. Measurements taken at edge of the room provided a value for leq dBa of 86.4 dB.

By doing this, the acoustic noise reduces at the expense of the minimum achievable readout time. This is in fact 437 ms for sequence **A**, and 664 ms for sequence **B**. Ideally, with EVI, we would need to sample k-space as fast as possible, so this is not ideal. However, now that a quieter solution is available, the number of k_z planes can be decreased to shorten the readout length. Diminishing or augmenting the number of second phase encodes does not change the acoustic noise because the readout structure remains identical.

	sequence **A**	sequence **B**	sequence **C**	sequence **D**
Peak dBa (dB), edge of the room	93.2	88.5	93.2	88.5
PF factor	1	1	0.7	0.7
Readout length (ms)	437	664	310	470
Echo time T_E (ms)	205	341	100	146

TABLE 4.2: EVI sequences **A**, **B**, **C** and **D**.

Furthermore, a Partial Fourier center-out approach along the second phase encoding direction can reduce the minimum echo time substantially. This ultimately lead to the definition of two other sequences (**C** and **D** in Table 4.2), which will be described in detail in the next section.

4.3.5 Multi echo acquisition

We used the results from this multiecho acquisition to design the EVI sequences **C** and **D**. Figure 4.8 reports transverse, coronal and sagittal views of the first 14 echoes.

By looking at this data, we can deduce:

1. The signal lasts for about 150 ms. In designing the sequences **C** and **D**, we therefore decided to use a Partial Fourier factor of 0.7 resulting in a total of 14 acquired k_z planes. By doing so, the readout duration decreased from 437 ms to 310 ms from sequences **A** to **C** (T_E from 205 ms to 100 ms), and from 664 ms to 470 ms from **B** to **D** (T_E from 341 ms to 146 ms). Table 4.2 summarizes this.

2. The pencil beam excites signal coming from the mother that falls back inside the encoded field of view. This is clearly visible in the first two echoes of Figure 4.8 (red arrows). The reason for this can be attributed to the performance of the PB, which degrades in the presence of off resonance effects. The image based shimming procedure achieves good shimming within the

fetal head. However, the price to pay is elsewhere, where the field behaves in uncontrolled way. Therefore it seems likely, although unproven, that the $\mathbf{B}_0$ inhomogeneity is a cause of the unwanted excitation. Fortunately, these spurious components attenuate quite rapidly after excitation and, already at 55 ms, the signal contribution comes mainly from the fetus and the maternal bladder. Having identified this problem, it was addressed pragmatically by excluding from the reconstruction all data from echoes acquired at less than 55 ms.

4.3.6 Echo Volume Imaging on the fetus, second and third attempts

The fetal EVI dataset acquired with a flip angle of 15° is presented in Figure 4.9. In the Figure, the second and the third rows show fully encoded datasets (sequences **A** and **B**) whereas the fourth row reports the data obtained by using Partial Fourier encoding (sequence **C**). All datasets underwent the same reconstruction process and were windowed the same way so they represent signal strength.

The maternal bladder is resolved in all cases as its T_2^* is very long. The brain is also partly visible in all other datasets, with a stronger signal at shorter echoes.

The result from the bladder experiment is shown in Figure 4.10, where we plot the mean value across the pencil beam as a function of the flip angle. The blue curve represents fully encoded data (sequence **A**), whereas the second row reports the Partial Fourier acquisition (sequence **C**).

By looking at the Figure, there seems to be a similar trend with a peak at around 45°. Beyond this value, the signal drops and this may be due to the excitation pulse degrading at high flip angles [Nehrke et al., 1999].

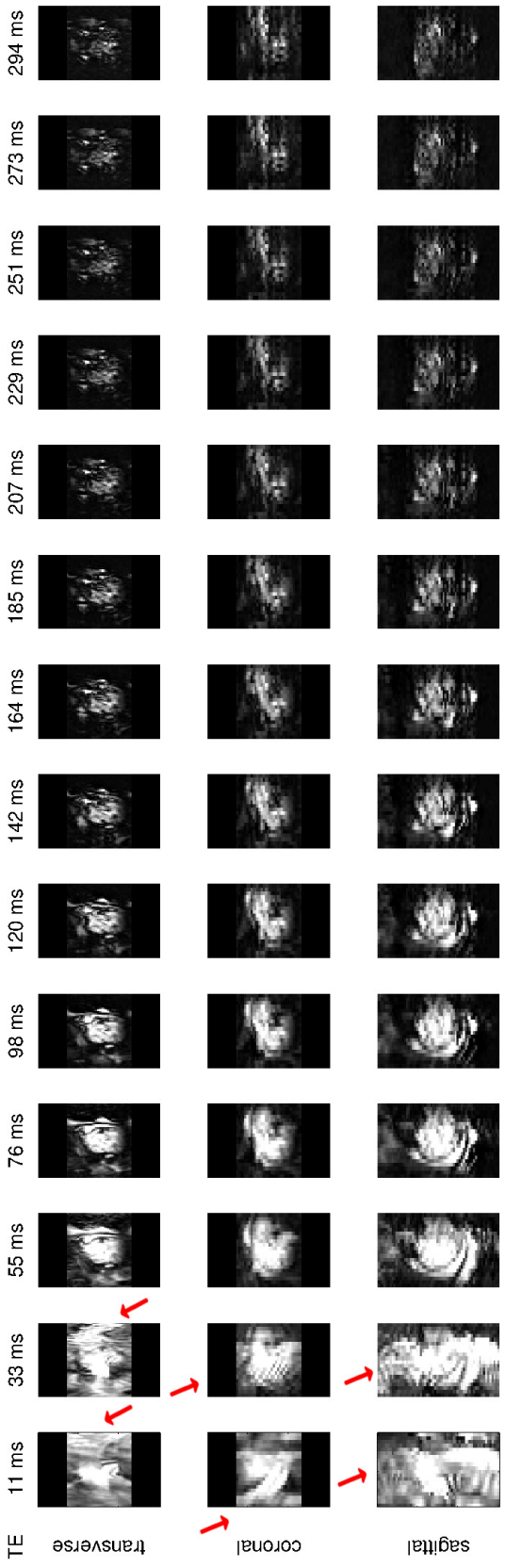

FIGURE 4.8: Transverse, coronal and sagittal views of the 3D multi echo EPI fetal dataset excited using a pencil beam with a diameter of 70 *mm* and flip angle of 45°. Areas in which the excitation fails are indicated by red arrows.

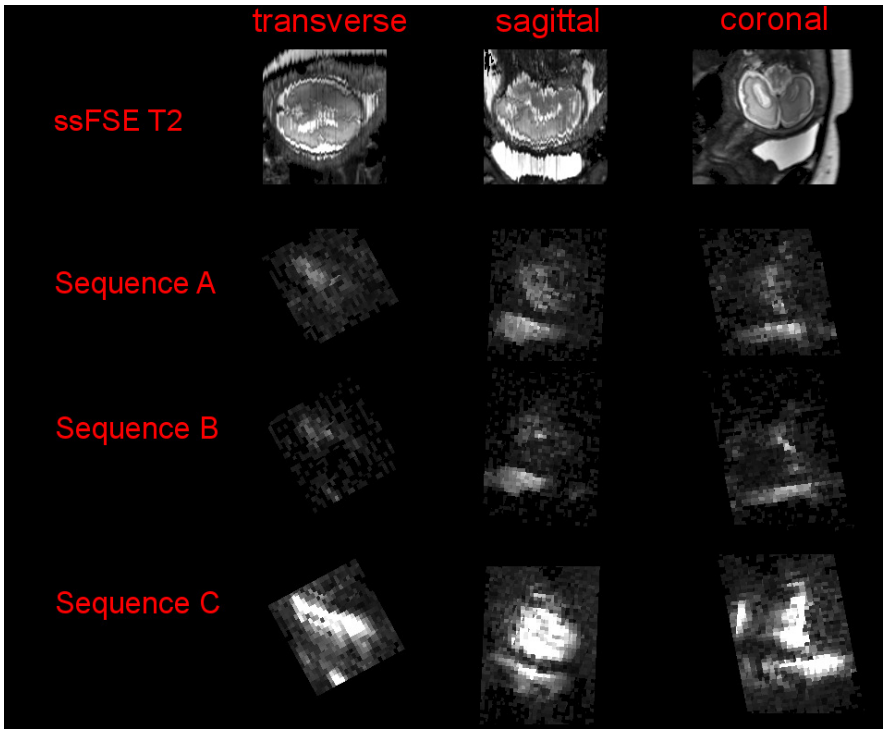

FIGURE 4.9: Fetal EVI data acquired with the quiet EVI sequences. First row is a ssFSE T_2 reference - second and third the fully encoded dataset (sequences **A** and **B** of Table 4.2) - fourth row the Partial Fourier acquisition (sequence **C**). In this case, sequence **D** did not provide useful data.

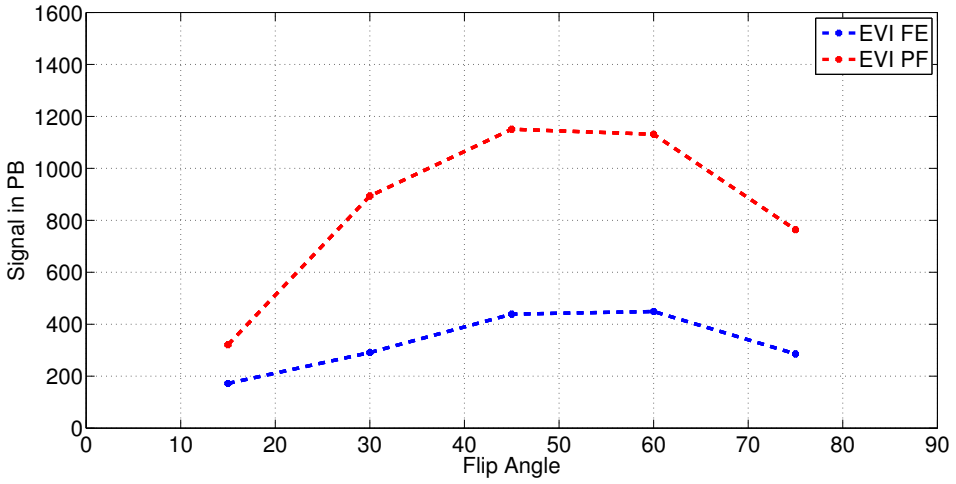

FIGURE 4.10: Bladder signal strength for different flip angles obtained by using fully encoded (sequence **A**, blue) and partial Fourier (sequence **C**, red) EVI acquisitions.

Data from the third and last fetal EVI acquisition is shown in Figure 4.11, where there is a similar trend as in Figure 4.9. However, in this data there is a better resemblance between the anatomical T_2 image and the EVI data, particularly and mostly in the two Partial Fourier acquisitions.

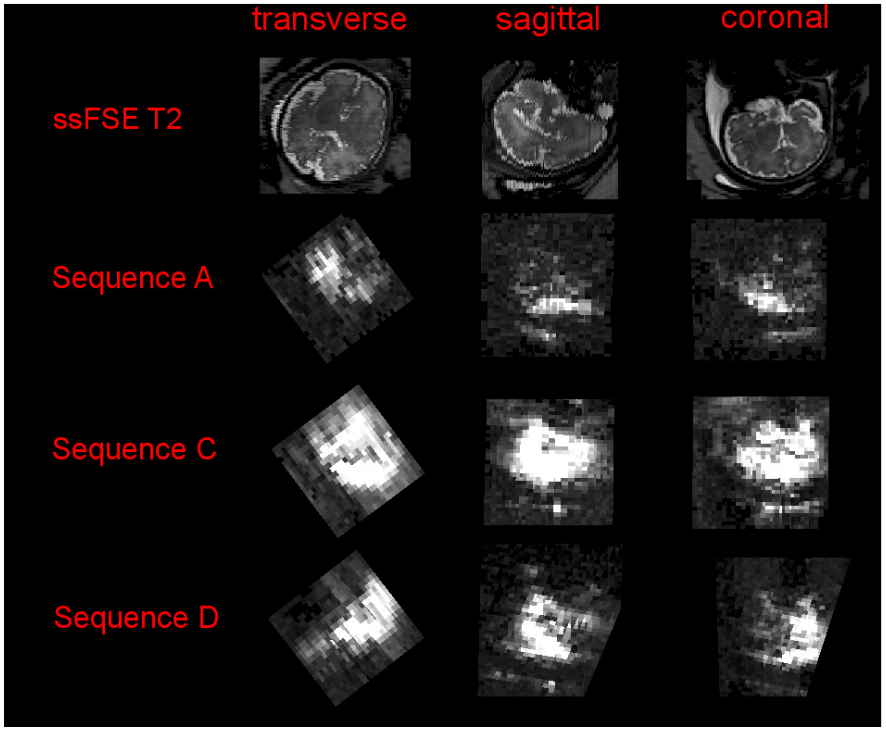

FIGURE 4.11: Fetal EVI data acquired with a flip angle of 45°. First row is a ssFSE T_2 anatomical reference - second a fully encoded dataset (sequence **A** of Table 4.2) - third and fourth rows the Partial Fourier acquisitions (sequences **C** and **D**). In this case, sequence **B** did not provide useful data.

4.4 Conclusions

In this chapter, the possibility of using EVI to image the fetal brain was investigated. EVI offers the potential for high speed and high SNR imaging that would be less prone to signal fluctuations due to spin history effects caused by fetal motion [Ferrazzi et al., 2014], so could provide a powerful tool for fetal fMRI. A key problem with other applications of EVI is the need for very long readouts which can result in signal loss due to T_2^* decay and massive distortion due to

operating with an extremely low bandwidth compared to the susceptibility induced $\mathbf{B}_0$ field variations, particularly at air-tissue interfaces. Fetal EVI is likely to be less undermined by both these effects because the T_2^* of the fetal brain is long [Vasylechko et al., 2014], and there are no local air tissue interfaces except in occasional cases where gas pockets in the maternal gut happen to be close to the fetal head.

However, even with this favourable context, the large field of view required to encode the maternal anatomy presents a challenge in terms of the amount of k-space data required. This was addressed by combining EVI with pencil beam excitation to limit the extent of the phase encoded field of view. The combined method was tested using the adult ventricles as model anatomy that has both long T_2^* and is far from air-tissue interfaces. As shown in Figure 4.5, these tests were encouraging. However, the EVI readout was found to be extremely noisy and it was concluded that, as implemented, it was not acceptable for routine use on fetal subjects. This was addressed by adjusting parameters such as the slew rate of the gradient waveform, which did enable quieter operation, but at the expense of a longer readouts.

The strategy of using a pencil beam excitation to limit the field of view was only partially successful, with clear contamination of early echo signals from out-of-beam signals (Figure 4.8). There remain uncertainties to explore to fully diagnose the causes of the problem. The present hypothesis that off resonance effects in maternal tissue caused by localized $\mathbf{B}_0$ shimming on the fetal brain would need further investigation. An alternative solution to this could be the use of saturation slabs, although this would have a negative impact on the efficiency of the sequence, undermining one of its expected advantages, as well as increasing the Specific Absorption Rate (SAR).

Despite these challenges, the work has been able to demonstrate that EVI is feasible and many technical issues such as setting up image based $\mathbf{B}_0$ shimming with accommodation of changes in patient bed positions and optimizing the flip

angle were solved. Also, the strategy of using variants of EPI (mutli-echo and 3D) that are available as standard scanner options proved effective in enabling the experiments to succeed even though the reconstruction of the final EVI data had to wait until after the examination was over so could not provide feedback to immediately correct problems. The images presented in Figure 4.9 and Figure 4.11 clearly show that fetal EVI is feasible and the next steps will need to address the acoustic noise issues to try to find a way to achieve an acceptable operating point without such a severe loss of efficiency. In this context, alternative gradients trajectories could be studied - for example, the use of a sinusoidal readout in conjunction with constant phase encoding gradients has been proven to be beneficial in terms of acoustic noise reduction [Peelle et al., 2010]. The use of a spiral strategy may also be explored.

To conclude, the EVI sequence needs to be further optimized. Once this has been achieved, we plan to acquire resting state fMRI data on a group of fetuses, so as to test robustness to motion, and compare the recovered brain networks to those estimated using 2D multi slice EPI acquisitions.

Chapter 5

Conclusions and future work

The main focus of this thesis is to develop methods to perform resting state fMRI in the fetus.

There is an increased interest of the research community towards this field and the first clinical applications are appearing - Huo et al. [2015] has recently shown, for example, how BOLD fetal fMRI data can be used to monitor the fetal and placental responses to maternal hyperoxygenation in subjects suffering from intrauterine growth restriction (IUGR).

The BOLD signal strength in resting state data is, however, restricted to be 3-4% of the bulk signal. This renders fetal resting state fMRI a very challenging research topic. Furthermore, signal misinterpretation is an endemic risk caused by key confounding factors such as motion and consequent spin history effects.

Therefore, performing fMRI *in utero* requires methods capable of coping with the the high level of motion performed by both the fetus and the mother. In this thesis, we demonstrate how it is possible to tackle the challenge posed by motion both from the acquisition and postprocessing sides.

The second Chapter of this thesis employs full slice by slice motion correction methods to mitigate the effects of fetal motion. Other confounding factors such as

signal distortion, spin history effects and bias field inhomogeneities are addressed. We ultimately show how canonical resting state networks can be extracted via careful application of these methods. Furthermore, the approach is designed so that it minimizes the data rejection rate.

There are several aspects of this work that are amenable to further investigation. Certainly, the most appealing direction for future work is the integration of these methods with simultaneous multi slice (SMS) imaging [Larkman et al., 2001]. Fetal fMRI studies could benefit from a SMS scheme in two different ways: 1) by accelerating the data acquisition to improve efficiency and better sampling of the the moving fetal brain, and 2) by stabilising the results of the image registration needed for motion correction and data analysis. In an initial series of tests that we have conducted for the developing Human Connectome Project (dHCP, http://www.developingconnectome.org/), we have used SMS 4 and acquired fetal fMRI data with a repetition time of 965 ms. As multiple slices are excited at the same time, the registration framework of section 2.2.1.4 was constrained to register blocks of 4 slices instead of just 1. For comparison, slices were also registered individually as if the data had been acquired using a conventional single band EPI sequence. The two analyses produced similar trends, but registration of the SMS data resulted in much less variability in the motion estimates, particularly for those parameters describing out of plane rotations and translations. Thus SMS has the potential of stabilizing and improving motion correction, which is the key part of what has been presented here.

This thesis has also explored methods to improve fetal fMRI by altering image acquisition. These strategies were tailored to the specific properties of the fetus (namely the longer T_2^*) and its location deep inside the maternal womb.

Chapter 3 discusses echo shifting and its application to the field of neonatal fMRI. Specifically, we demonstrate how echo shifting allows access to a greater BOLD to noise contrast while maintaining efficient sampling properties. Despite the T_2^*

being longer in immature brains, the issue of signal dropout at air-tissue interfaces at longer T_E remains. This is an aspect that warrants further exploration. These preliminary results suggests that echo shifting is a viable approach. The methodology could be particularly suitable for fetal fMRI studies, where signal dropout is less significant as air/tissue boundaries are generally absent in the womb [Ferrazzi et al., 2014]. The sequence would also need to be integrated with fat suppression of the maternal tissue, which is a simple addition to what has been demonstrated here. Echo shifting is completely compatible with multi-band methods [Boyacioglu et al., 2015, Feinberg and Setsompop, 2013, Larkman et al., 2001] and this combination could potentially provide higher sampling rates at long echo times.

The idea of using an EVI readout to encode the whole fetal head in a single shot is explored in Chapter 4. EVI is the fastest sequence among all EPI-like acquisitions, including SMS. Therefore, EVI is insensitive to motion and spin history effects. The sampling rate achieved with an EVI readout could potentially overcome the maternal respiration and fetal cardiac pulsation. The fetal heart beats 120 to 160 times per minute, therefore considerably faster than the normal adult at rest. This means that a T_R within 190 to 250 ms is needed to avoid aliasing. It is clear that SMS cannot achieve this.

EVI as implemented in this work was found to be capable of imaging the whole fetal brain in a single shot. However, the sequence was too loud to be run routinely run in utero and therefore lower slew rates and gradient amplitudes had to be used, resulting in lower acquisition bandwidth and high sensitivity to distortions and signal loss. As it stands, EVI cannot yet be adopted to study the fetal brain. However, different options such as the use of alternative gradient acquisition trajectories for acoustic noise reduction, or even an the adoption of an intermediate solution between a pure single shot and multishot sequences could be explored and this is part of our future work.

Taken as a whole, this thesis contains a multitude of solutions which together enable fetal fMRI to become a systematic way to assess brain development *in utero*. This thesis addresses core issues encountered when dealing with fetal fMRI data, and it constitutes the basis for which routine and reliable medical examinations could be carried out in the near future.

Selected Conference and Journal Publications

- Giulio Ferrazzi, Maria Kuklisova Murgasova, Tomoki Arichi, Christina Malamateniou, Matthew J Fox, Antonios Makropoulos, Joanna Allsop, Mary Rutherford, Shaihan Malik, Paul Aljabar and Joseph V. Hajnal. Resting state fMRI in the moving fetus: A robust framework for motion, bias field and spin history correction. *NeuroImage*, 101(1):555 568, 2014.

- Giulio Ferrazzi* and Rita G. Nunes*, Tomoki Arichi, Andreia O. Gaspar, Giovanni Barone, Alessandro Allievi, Maryam Abaei, Emer Hughes, Anthony N. Price, and Joseph V. Hajnal. An exploration of task based fMRI in neonates using echo-shifting to allow acquisition at longer T_E without loss of temporal efficiency. Submitted to *NeuroImage*, 2015.

- Rita G. Nunes* and Giulio Ferrazzi*, Anthony Price, Matthew Fox, Christina Malamateniou, Mary Rutherford and Joseph Hajnal. Combined Echo Volumar Imaging (EVI) and Localized Excitation for Motion Insensitive Fetal fMRI. *In Proc ISMRM*, 2015, Toronto (Canada).

NeuroImage 101 (2014) 555–568

Contents lists available at ScienceDirect

NeuroImage

journal homepage: www.elsevier.com/locate/ynimg

Resting State fMRI in the moving fetus: A robust framework for motion, bias field and spin history correction

Giulio Ferrazzi [a,*], Maria Kuklisova Murgasova [a], Tomoki Arichi [a,b], Christina Malamateniou [a], Matthew J. Fox [a], Antonios Makropoulos [a], Joanna Allsop [a], Mary Rutherford [a], Shaihan Malik [a], Paul Aljabar [a], Joseph V. Hajnal [a]

[a] Centre for the Developing Brain, Division of Imaging Sciences & Biomedical Engineering, King's College London, St Thomas' Hospital, Westminster Bridge Rd, London SE1 7EH, UK
[b] Department of Biomedical Engineering, Imperial College London, South Kensington Campus, London SW7 2AZ, UK

ARTICLE INFO

Article history:
Accepted 28 June 2014
Available online 6 July 2014

Keywords:
Fetal fMRI
Slice to volume registration
Resting State Networks
Scattered interpolation
Bias field correction
Spin history correction

ABSTRACT

There is growing interest in exploring fetal functional brain development, particularly with Resting State fMRI. However, during a typical fMRI acquisition, the womb moves due to maternal respiration and the fetus may perform large-scale and unpredictable movements. Conventional fMRI processing pipelines, which assume that brain movements are infrequent or at least small, are not suitable. Previous published studies have tackled this problem by adopting conventional methods and discarding as much as 40% or more of the acquired data.
In this work, we developed and tested a processing framework for fetal Resting State fMRI, capable of correcting gross motion. The method comprises bias field and spin history corrections in the scanner frame of reference, combined with slice to volume registration and scattered data interpolation to place all data into a consistent anatomical space. The aim is to recover an ordered set of samples suitable for further analysis using standard tools such as Group Independent Component Analysis (Group ICA).
We have tested the approach using simulations and *in vivo* data acquired at 1.5 T. After full motion correction, Group ICA performed on a population of 8 fetuses extracted 20 networks, 6 of which were identified as matching those previously observed in preterm babies.

Introduction

Resting State Networks (RSNs) are consistently mapped in different human populations with functional MRI (fMRI) and are the topic of extensive Neuroscience research (Van Den Heuvel and Hulshoff Pol, 2010). RSNs are characterized by low frequency temporal fluctuations of the blood-oxygen-level-dependent (BOLD) signal which are correlated between distinct anatomical regions when a subject is imaged at rest, or at least with no prescribed activity or stimulus (Biswal et al., 1995; Buckner et al., 2008). Spatial mapping of RSNs in adults suggests that involved areas are functionally relevant, and include regions involved in motor, visual, auditory, executive and memory functioning (Damoiseaux et al., 2006). RSNs have also been described in infants, and include many of those regions seen in the mature brain (Damaraju et al., 2010; Fransson et al., 2007, 2009, 2011; Gao et al., 2009).

The emergence of RSNs during the preterm period was explored by Smyser et al. (2010) and Doria et al. (2010), who were able to map a full repertoire of networks encompassing the visual, auditory, somatosensory, motor, and executive control areas. These infant studies have identified a maturational trend during this period (equivalent to the third trimester of gestation) consisting of a progression from lateralized networks to bilateral patterns at full term equivalent post-menstrual age (PMA).

The studies on preterm babies suggest that it is of great interest to look at the development of RSNs directly *in utero*. However, this is a challenge, as during the several minutes taken to acquire a typical fMRI dataset, the fetal brain undergoes large-scale motion caused by changes in fetal position within the womb and also as a result of maternal respiration.

Fetuses move sporadically and in an unpredictable fashion (Malamateniou et al., 2013). These movements take place in both the in-plane and the out-of-plane directions. Motion, particularly head rotations and nodding, can be rapid. The quality and duration of periods of motion vary with gestational age, such that, as the fetuses get larger later in pregnancy, they may have longer quiet periods and body motion is more constrained (Hayat et al., 2011).

Some preliminary studies have explored fetal RSNs using conventional processing pipelines. Schöpf et al. (2012) acquired fMRI data from 87 healthy fetuses and used single subject Probabilistic ICA (Beckmann and Smith, 2004) to identify RSNs. However, because of large motion levels, 71 datasets couldn't be processed. Thomason et al. (2013) analyzed a set of 25 healthy subjects in the second and third trimesters of gestation using Group ICA (Calhoun et al., 2009) and correlation analysis. In this study, individual time frames were rejected, with

* Corresponding author.
E-mail address: giulio.ferrazzi@kcl.ac.uk (G. Ferrazzi).

http://dx.doi.org/10.1016/j.neuroimage.2014.06.074
1053-8119/

An exploration of task based fMRI in neonates using echo-shifting to allow acquisition at longer T_E without loss of temporal efficiency

Giulio Ferrazzi[a,1,*], Rita G. Nunes[a,b,1], Tomoki Arichi[a,c], Andreia O. Gaspar[a,b], Giovanni Barone[a,d], Alessandro Allievi[c], Maryam Abaei[a], Emer Hughes[a], Anthony N. Price[a], Joseph V. Hajnal[a]

[a] *Centre for the Developing Brain, Division of Imaging Sciences & Biomedical Engineering, King's College London, St Thomas' Hospital, Westminster Bridge Rd London SE1 7EH, UK. Telephone: + 44 (0) 20 7188 9145.*
[b] *Instituto de Biofisica e Engenharia Biomedica, Universidade de Lisboa, Faculdade de Ciencias da Universidade de Lisboa, Campo Grande, Lisbon 1749-016, Portugal*
[c] *Department of Biomedical Engineering, Imperial College London, South Kensington Campus London SW7 2AZ, UK*
[d] *Catholic University of Sacred Heart. Largo A. Gemelli 8, Rome 00168, Italy*

Abstract

Optimal BOLD to noise contrast in neonatal and fetal fMRI has been hard to achieve because of the much longer T_2^* values in developing brain tissue in comparison to those in the mature adult brain. The conventional approach of optimizing fMRI sequences would suggest matching the echo time (T_E) and the T_2^* of the neonatal and fetal brain. However, the use of a long echo time would typically increase the minimum repetition time (T_R) resulting in inefficient sampling.

Here we apply the concept of echo shifting to task based neonatal fMRI in order to achieve an improved BOLD to noise contrast and efficient data sampling at the same time. Echo shifted EPI (es-EPI) is a modification of a standard 2D-EPI sequence which enables echo times longer than the time between consecutive excitations ($T_E > T_S = \frac{T_R}{N_S}$, where N_S is the number of acquired slices and T_S the inter-slice repetition time). The proposed method

*Corresponding author
Email address: giulio.ferrazzi@kcl.ac.uk (Giulio Ferrazzi)
[1] Contributed equally to the paper

5342

Combined Echo Volumar Imaging (EVI) and Localized Excitation for Motion Insensitive Fetal fMRI

Rita G. Nunes[1,2], Giulio Ferrazzi[1], Anthony Price[1], Matthew Fox[1], Christina Malamateniou[1], Mary Rutherford[1], and Joseph Hajnal[1,3]

[1]*Centre for the Developing Brain, King's College London, London, United Kingdom,* [2]*Instituto de Biofisica e Engenharia Biomedica, Universidade de Lisboa, Lisbon, Portugal,* [3]*Division of Imaging and Sciences and Biomedical Engineerin, King's College London, London, United Kingdom*

TARGET AUDIENCE This research will benefit those researchers interested in fetal functional brain studies and sequence optimization.

PURPOSE Echo Volume Imaging (EVI) is an extension of the well-known Echo Planar Imaging (EPI) sequence that allows the acquisition of a whole fMRI volume following a single RF excitation; this leads to a repetition time TR in the order of a few hundreds of milliseconds depending on the field of view (FOV) and image resolution. The main benefits are increased temporal resolution and robustness to motion [1]. The downside is that EVI is extremely sensitive to B_0 field inhomogeneities and T2* signal decay limits the achievable image resolution; these factors have so far limited the usage of EVI in functional MR imaging.

Fetal fMRI is an emerging field of research [2-4]. Initial studies used standard multi-slice 2D EPI and were therefore very sensitive to fetal motion requiring careful application of motion correction algorithms [4]. Combining selective excitation of the fetal brain, avoids the need to spatially encoding the maternal tissues, and using an EVI readout would greatly reduce the TR and therefore motion sensitivity. Moreover, the maternal tissue offers an optimal environment for EVI usage since B_0 field inhomogeneities are much less pronounced than in adult fMRI experiments because of the lack of air-tissue boundaries within the fetal head and the womb. Furthermore, T2* values were recently measured across the fetal brain and shown to be much longer than in the adult brain [5] paving the way for EVI applications.

In this work we have developed an EVI sequence featuring localised excitation [6], and test it on three adult volunteers and also performed a primarily acquisition test of the fetal brain *in utero*.

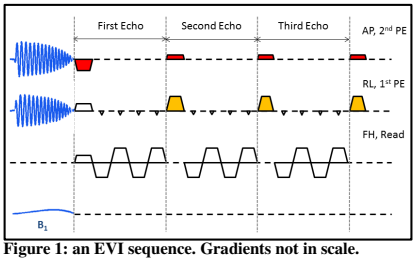

Figure 1: an EVI sequence. Gradients not in scale.

METHODS The data used in this study came from 3 healthy adults (males, age range: 24 to 33 years) and 1 fetus (gestational age of 30+4 weeks) who had been assessed as normal. Informed consent was obtained for all examinations. Scans were performed on a Philips (Best, the Netherlands) Achieva 3T scanner with 32 channel receiver coils – a head coil to image the ventricles in adult brain and a cardiac torso coil for fetal imaging. The ventricle region was chosen to ensure a good shimming and long T2*. To achieve EVI, an existing multi-echo EPI sequence was modified. This sequence is schematically represented in Figure 1; Pencil beam (PB) excitation gradients and B1 are shown in blue. These excite a cylindrical column aligned with the foot-head (FH) axis. A multi-echo EPI gradient pattern with readout along this axis and primary phase encoding (PE) along the right-left (RL) was augmented by extra PE gradients on the anterior-posterior (AP) axis (shown in red) to achieve EVI encoding. The number of PE lines was kept even to improve consistency between adjacent k-space planes [7], avoiding ghosting along the second phase encode direction. To achieve maximal encoding rate, ramp sampling was used on the EVI readout with 0.377 ms required per data line. Prior to testing on a fetus, the acoustic noise produced by the sequence was measured using a calibrated MR compatible microphone, but the sound level exceeded established local guidelines. A coarser resolution was therefore adopted allowing lower gradient amplitudes for the fetal test leading to a readout window per k-space line of 0.355 ms. For all localised acquisitions, the FOV was 200×100×100 mm^3, with an excited PB diameter of 70 mm and 15° flip angle. The FOV was encoded at a resolution of 3.5×3.5×3.5 mm^3 for the adult scans (matrix size 56×28×29, total readout time 348 ms) and 5×5×5 mm^3 for the fetus (matrix size 40×18×20, total readout time 154 ms). For comparison, multi-shot 3D EPI images (29 shots with TR = 500 ms for the adult cases and 20 shots for the fetus) with matching FOV and resolution to the EVI images were also acquired with a TE of 80 ms. Furthermore, to provide a visual anatomical reference to the adult cases, high resolution 3D multi-shot EPI images were acquired with a FOV of 240×200×240 mm^3, resolution of 2×2×2 mm^3 and TE of 80 ms. To minimize geometric distortions in all acquisitions, image-based shimming [8] was performed over the adult or fetal brains and the shim values kept the same throughout the exams. Each acquisition was accompanied by a B_0 field map that was acquired using a 3D dual gradient echo sequence with ΔTE = 2.3 ms and resolution of 5×5×5 mm^3.

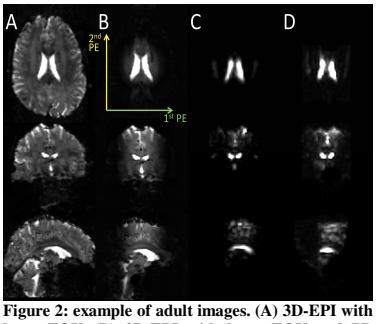

Figure 2: example of adult images. (A) 3D-EPI with large FOV. (B) 3D-EPI with large FOV and PB excitation. (C) 3D-EPI with small FOV and localized excitation. (D) EVI with PB excitation. Phase encode directions indicated in green (1st) and yellow (2nd).

3D-EPI and EVI data were reconstructed offline. Ghost correction along the first phase encode (RL) was achieved using a self-reference method as proposed in [9] and corrected for geometric distortions [10]: along the RL direction for the 3D-EPI data and considering only the slower PE direction for EVI.

RESULTS Acquisitions were successful in all three adult volunteers and in the fetal brain, although the quality of the achieved shim was poorer in the latter case; for example, for one of the adults, the average residual field after image based shimming was of 22±30 Hz within the brain (mean and standard deviation), whereas in the fetal case these values were 61±46 Hz. A possible explanation for this is that in the fetal case a very small region encompassing the head was used to shim which may have led to a sub-optimal solution elsewhere within the PB. Furthermore, since the fetus was moving substantially between sequences, it could have moved outside the shimmed area. Figure 2 shows the images from the same adult subject along the three orthogonal planes for high resolution 3D-EPI images with standard excitation (A) and with PB excitation (B), 3D-EPI image with 200×100×100 mm^3 FOV and 3.5 mm isotropic resolution (C), and matching EVI (D). Distortion correction was performed on all of these acquisitions enabling geometrical matching of the EVI to the 3D-EPI acquisitions. The fetal images (three orthogonal planes) are displayed in Figure 3 and include: a single-shot multi-slice Fast Spin Echo T2-weighted anatomical image as reference (A), the standard 3D-EPI image with localized excitation (B), the equivalent EVI image prior to (C) and after applying geometric distortion correction (D). Although the resolution of the images is coarser than the adult equivalent, it is still possible to identify the mother's bladder (white arrow) and the fetal brain (red arrow).

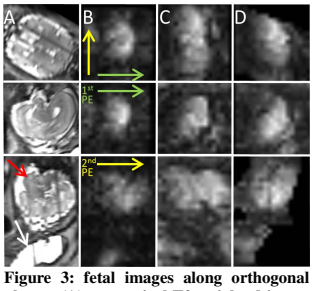

Figure 3: fetal images along orthogonal planes: (A) anatomical T2-weighted image showing the fetal brain (red arrow) and the mother's bladder (white). (B) 3D-EPI with PB excitation. (C) EVI. (D) EVI after distortion correction along the slow phase encode direction. Phase encode directions shown in green (fast) and yellow (slow).

CONCLUSIONS By using EVI combined with localized excitation it was possible to scan the whole fetal brain within approximately 150 ms attaining a 5.0 mm isotropic resolution. The next step is to further optimize the sequence to reduce acoustic noise with less sacrifice in readout rate. Once this has been achieved, we plan to acquire resting state fMRI data on a group of fetuses, so as to test robustness to motion, and compare the recovered brain networks to those estimated using multi-slice 2D-EPI acquisitions.

REFERENCES **1.** Yang Y et al. JMRI 1997;7(2),371-375. **2.** Schopf V et al., International Journal of Developmental Neuroscience 2012;30(1),11–17. **3.** Thomason ME et al., Science translational medicine 2013;5(173),1–10 **4.** Ferrazzi G et al., NeuroImage 2014;101(1),555–568. **5.** Vasylechko S et al., MRM 2014;doi:10.1002/mrm.25299. **6.** Nehrke K et al., MRI 1999; 17(8):1173-81. **7.** Van der Zwaag W et al., MRM 2006;56:1320-1327; **8.** Fillmer A et al., MRM 2014;doi:10.1002/mrm.25248; **9.** Buonocore M et al., MRM 1997;38(1):89-100. **10.** Jezzard P et al., MRM 1998; 34(1):65-73.

ACKNOWLEDGEMENT We would like to thank MRC strategic funds, GSTT BRC and ERC funded dHCP project.

Other Conference Proceedings

- Giulio Ferrazzi, Maria Kuklisova Murgasova, Christina Malamateniou, Paul Aljabar and Joseph V. Hajnal. Resting state fMRI in the moving fetus: a robust framework for motion correction. *In Proc ESMRMB*, 2013, Tolouse (France).

- Giulio Ferrazzi, Maria Kuklisova Murgasova, Tomoki Arichi, Christina Malamateniou, Matthew J Fox, Antonios Makropoulos, Joanna Allsop, Mary Rutherford, Shaihan Malik, Paul Aljabar and Joseph V. Hajnal. Resting State fMRI in the moving fetus: a robust framework for motion and spin history correction. *In Proc ISMRM*, 2014, Milan (Italy).

- Giulio Ferrazzi, Maria Kuklisova Murgasova, Tomoki Arichi, Christina Malamateniou, Matthew J Fox, Antonios Makropoulos, Joanna Allsop, Mary Rutherford, Shaihan Malik, Paul Aljabar and Joseph V. Hajnal. Resting state fMRI in the moving fetus: A robust framework for motion, bias field and spin history correction. *In Proc OHBM*, 2014, Hamburg (Germany).

- Maryam Abaei, Eugene Duff, Tomoki Arichi, Jonathan O'Muircheartaigh, Emer Hughes, Giulio Ferrazzi, Stephen Smith, Serena Counsell, David Edwards, Daniel Rueckert, Joseph V. Hajnal. Investigation of optimal echo time for resting-state fMRI acquisition in newborn infants. *In Proc ISMRM*, 2015, Toronto (Canada).

- Giulio Ferrazzi* and Rita G. Nunes*, Tomoki Arichi, Maryam Abaei, Emer Hughes, Anthony N. Price, and Joseph V. Hajnal. An exploration of task

based fMRI in neonates using echo-shifting to allow acquisition at longer T_E without loss of temporal efficiency. *In Proc ISMRM*, 2015, Toronto (Canada).

- Giulio Ferrazzi*, Rita G. Nunes*, Andreia Gaspar, Tomoki Arichi, Emer Hughes, Anthony Price, and Joseph Hajnal. An exploration of task-based fMRI in neonates using echo-shifting. *In Proc ESMRN*, 2015, Porto (Portugal).

- Rita G. Nunes*, Giulio Ferrazzi*, Andreia Gaspar, Anthony Price, Matthew Fox, Christina Malamateniou, Mary Rutherford, and Joseph Hajnal. Motion insensitive fetal fMRI combining localized excitation with Echo Volume Imaging *In Proc ESMRN*, 2015, Porto (Portugal).

- Bernhard Kainz, Christina Malamateniou, Giulio Ferrazzi, Maria Murgasova, Jan Egger, Kevin Keraudren, Mary Rutherford, Joseph V. Hajnal, Daniel Rueckert. Adaptive scan strategies for fetal MRI imaging using Slice to Volume techniques. *In Proc ISBI*, 2015, New York (US).

- Anthony Price, Giulio Ferrazzi, Jana Hutter, Andreia Gaspar, Matthew Fox, Joanna Allsop, Mary Rutherford, Joseph V. Hajnal. An investigation of Multi-Band imaging for rs-fMRI in the fetus. *In Proc ISMRM* Workshop on Simultaneous Multi-Slice Imaging, 2015, Pacific Grove (US).

- Giulio Ferrazzi, Anthony Price, Jana Hutter, Andreia Gaspar, Matthew Fox, Joanna Allsop, Mary Rutherford, Joseph V. Hajnal. An investigation of Multi-Band imaging for rs-fMRI in the fetus. *In Proc ESMRMB*, 2015, Edinburg (UK).

Bibliography

AG Allievi, A Melendez-Calderon, T Arichi, AD Edwards, and E Burdet. An fMRI compatible wrist robotic interface to study brain development in neonates. *Annals of biomedical engineering*, 41(6):1181–1192, 2013.

Tomoki Arichi, Gianlorenzo Fagiolo, Marta Varela, Alejandro Melendez-Calderon, Alessandro Allievi, Nazakat Merchant, Nora Tusor, Serena J Counsell, Etienne Burdet, Christian F Beckmann, et al. Development of BOLD signal hemodynamic responses in the human brain. *Neuroimage*, 63(2):663–673, 2012.

Peter A Bandettini, Eric C Wong, R Scott Hinks, Ronald S Tikofsky, and James S Hyde. Time course EPI of human brain function during task activation. *Magnetic Resonance in Medicine*, 25(2):390–397, 1992.

Peter A Bandettini, Eric C Wong, A Jesmanowicz, R Scott Hinks, and James S Hyde. Spin-echo and gradient-echo EPI of human brain activation using BOLD contrast: a comparative study at 1.5 T. *NMR in Biomedicine*, 7(1-2):12–20, 1994.

Christian F Beckmann and Stephen M Smith. Probabilistic independent component analysis for functional magnetic resonance imaging. *Medical Imaging, IEEE Transactions on*, 23(2):137–152, 2004.

Roshni Bhagalia and Boklye Kim. Spin saturation artifact correction using slice-to-volume registration motion estimates for fMRI time series. *Medical physics*, 35(2):424–434, 2008.

Rasmus M Birn, Jason B Diamond, Monica A Smith, and Peter A Bandettini. Separating respiratory-variation-related fluctuations from neuronal-activity-related fluctuations in fMRI. *Neuroimage*, 31(4):1536–1548, 2006.

Felix Bloch. Nuclear induction. *Physical review*, 70(7-8):460, 1946.

Rasim Boyacioglu, Jenni Schulz, and David Norris. Multiband echo shifted epi. In *Proc ISMRM MultiBand workshop (Pacific Grove, US)*, 2015.

Randy L Buckner, Jessica R Andrews-Hanna, and Daniel L Schacter. The brain's default network. *Annals of the New York Academy of Sciences*, 1124(1):1–38, 2008.

Ed Bullmore and Olaf Sporns. Complex brain networks: graph theoretical analysis of structural and functional systems. *Nature Reviews Neuroscience*, 10(3): 186–198, 2009.

ET Bullmore, MJ Brammer, S Rabe-Hesketh, VA Curtis, RG Morris, SCR Williams, T Sharma, and PK McGuire. Methods for diagnosis and treatment of stimulus-correlated motion in generic brain activation studies using fMRI. *Human brain mapping*, 7(1):38–48, 1999.

Michael H Buonocore and Lisheng Gao. Ghost artifact reduction for echo planar imaging using image phase correction. *Magnetic resonance in medicine*, 38(1): 89–100, 1997.

Richard B Buxton. *Introduction to functional magnetic resonance imaging: principles and techniques*. Cambridge university press, 2009.

Vince D Calhoun, Jingyu Liu, and Tülay Adalı. A review of group ICA for fMRI data and ICA for joint inference of imaging, genetic, and ERP data. *Neuroimage*, 45(1):S163–S172, 2009.

Jean-Fran Cardoso. Infomax and maximum likelihood for blind source separation. *IEEE Signal processing letters*, 4(4):112–114, 1997.

Wei-Tang Chang, Aapo Nummenmaa, Thomas Witzel, Jyrki Ahveninen, Samantha Huang, Kevin Wen-Kai Tsai, Ying-Hua Chu, Jonathan R Polimeni, John W Belliveau, and Fa-Hsuan Lin. Whole-head rapid fMRI acquisition using echo-shifted magnetic resonance inverse imaging. *Neuroimage*, 78:325–338, 2013.

Yiu-Cho Chung and Jeffrey L Duerk. Signal formation in echo-shifted sequences. *Magnetic resonance in medicine*, 42(5):864–875, 1999.

Eswar Damaraju, Arvind Caprihan, JR Lowe, Elena A Allen, Vince D Calhoun, and JP Phillips. Functional connectivity in the developing brain: A longitudinal study from 4 to 9 months of age. *NeuroImage*, 84:169–180, 2014.

JS Damoiseaux, SARB Rombouts, F Barkhof, P Scheltens, CJ Stam, Stephen M Smith, and CF Beckmann. Consistent resting-state networks across healthy subjects. *Proceedings of the National Academy of Sciences*, 103(37):13848–13853, 2006.

Mark De Berg, Otfried Cheong, Marc van Kreveld, and Mark Overmars. *Computational geometry*. Springer, 2008.

Christophe Delalande, Jacco A de Zwart, Herve Trillaud, Nicolas Grenier, and Chrit TW Moonen. An echo-shifted gradient-echo MRI method for efficient diffusion weighting. *Magnetic resonance in medicine*, 41(5):1000–1008, 1999.

Amit Delaunay, Boris Arora, Eric M. Scholar. "Role of tyrosine kinase inhibitors in cancer therapy." Journal of Pharmacology, and Experimental Therapeutics 315.3 (2005): 971-979.N. Sur la sphère vide. *Bulletin of Academy of Sciences of the USSR*, 7(6):793–800, 1934.

A.P. Dempster, N.M. Laird, and D.B. Rubin. Maximum likelihood from incomplete data via the EM-algorithm. *Journal of the Royal Statistical Society*, 39 (1):1–38, 1977.

Valentina Doria, Christian F Beckmann, Tomoki Arichi, Nazakat Merchant, Michela Groppo, Federico E Turkheimer, Serena J Counsell, Maria Murgasova,

Paul Aljabar, Rita G Nunes, et al. Emergence of resting state networks in the preterm human brain. *Proceedings of the National Academy of Sciences*, 107 (46):20015–20020, 2010.

R.O. Duda, P.E. Hart, and D.G. Stork. *Pattern Classification.* John Wiley & Sons Inc, second edition, 2001.

Gary E Duncan, Walter E Stumpf, and Christof Pilgrim. Cerebral metabolic mapping at the cellular level with dry-mount autoradiography of [3H]2-deoxyglucose. *Brain research*, 401(1):43–49, 1987.

David A Feinberg and Kawin Setsompop. Ultra-fast MRI of the human brain with simultaneous multi-slice imaging. *Journal of Magnetic Resonance*, 229 (0):90–100, 2013.

Giulio Ferrazzi, Maria Kuklisova Murgasova, Tomoki Arichi, Christina Malamateniou, Matthew J Fox, Antonios Makropoulos, Joanna Allsop, Mary Rutherford, Shaihan Malik, Paul Aljabar, et al. Resting state fMRI in the moving fetus: A robust framework for motion, bias field and spin history correction. *NeuroImage*, 101(1):555–568, 2014.

Peter Fransson, Beatrice Skiöld, Sandra Horsch, Anders Nordell, Mats Blennow, Hugo Lagercrantz, and Ulrika Åden. Resting-state networks in the infant brain. *Proceedings of the National Academy of Sciences*, 104(39):15531–15536, 2007.

Peter Fransson, Beatrice Skiöld, Mathias Engström, Boubou Hallberg, Mikael Mosskin, Ulrika Åden, Hugo Lagercrantz, and Mats Blennow. Spontaneous brain activity in the newborn brain during natural sleep - an fMRI study in infants born at full term. *Pediatric Research*, 66(3):301–305, 2009.

Karl Friston, John Ashburner, Christopher D Frith, J-B Poline, John D Heather, Richard SJ Frackowiak, et al. Spatial registration and normalization of images. *Human brain mapping*, 3(3):165–189, 1995.

Karl J Friston, Steven Williams, Robert Howard, Richard SJ Frackowiak, and Robert Turner. Movement-related effects in fMRI time-series. *Magnetic resonance in medicine*, 35(3):346–355, 1996.

Jon Fulford and Penny A Gowland. The emerging role of functional MRI for evaluating fetal brain activity. In *Seminars in perinatology*, volume 33, pages 281–288. Elsevier, 2009.

Jonathan Fulford, Shantala H Vadeyar, Senani H Dodampahala, Rachel J Moore, Paul Young, Philip N Baker, David K James, and Penny A Gowland. Fetal brain activity in response to a visual stimulus. *Human brain mapping*, 20(4): 239–245, 2003.

Kenneth J Gerhardt and Robert M Abrams. Fetal hearing: characterization of the stimulus and response. In *Seminars in perinatology*, volume 20, pages 11–20. Elsevier, 1996.

Ali Gholipour, Judy A Estroff, and Simon K Warfield. Robust super-resolution volume reconstruction from slice acquisitions: application to fetal brain MRI. *Medical Imaging, IEEE Transactions on*, 29(10):1739–1758, 2010.

Andrew Gibson, Andrew M Peters, and Richard Bowtell. Echo-shifted multislice EPI for high-speed fMRI. *Magnetic resonance imaging*, 24(4):433–442, 2006.

Gary H Glover. Deconvolution of impulse response in event-related BOLD fMRI. *Neuroimage*, 9(4):416–429, 1999.

Gary H Glover, Tie-Qiang Li, and David Ress. Image-based method for retrospective correction of physiological motion effects in fMRI: RETROICOR. *Magnetic Resonance in Medicine*, 44(1):162–167, 2000.

P Glover, J Hykin, P Gowland, J Wright, I Johnson, and P Mansfield. An assessment of the intrauterine sound intensity level during obstetric echo-planar magnetic resonance imaging. *The British journal of radiology*, 68(814):1090–1094, 1995.

Robert L Goldenberg, Jennifer F Culhane, Jay D Iams, and Roberto Romero. Epidemiology and causes of preterm birth. *The lancet*, 371(9606):75–84, 2008.

Gene H Golub and Christian Reinsch. Singular value decomposition and least squares solutions. *Numerische Mathematik*, 14(5):403–420, 1970.

William J Gordon and James A Wixom. Shepard's method of "metric interpolation" to bivariate and multivariate interpolation. *Mathematics of Computation*, 32(141):253–264, 1978.

Penny Gowland and Jonathan Fulford. Initial experiences of performing fetal fMRI. *Experimental neurology*, 190(1):22–27, 2004.

Michael D Greicius, Gaurav Srivastava, Allan L Reiss, and Vinod Menon. Default-mode network activity distinguishes Alzheimer's disease from healthy aging: evidence from functional MRI. *Proceedings of the National Academy of Sciences of the United States of America*, 101(13):4637–4642, 2004.

Michael D Greicius, Kaustubh Supekar, Vinod Menon, and Robert F Dougherty. Resting-state functional connectivity reflects structural connectivity in the default mode network. *Cerebral cortex*, 19(1):72–78, 2009.

Rolf Gruetter. Automatic, localized in vivo adjustment of all first-and second-order shim coils. *Magnetic Resonance in Medicine*, 29(6):804–811, 1993.

Rolf Gruetter and Chris Boesch. Fast, noniterative shimming of spatially localized signals. in vivo analysis of the magnetic field along axes. *Journal of Magnetic Resonance (1969)*, 96(2):323–334, 1992.

E Mark Haacke, Robert W Brown, Michael R Thompson, and Ramesh Venkatesan. *Magnetic resonance imaging: physical principles and sequence design*, volume 1. Wiley-Liss New York:, 1999.

Erwin L Hahn. Spin echoes. *Physical review*, 80(4):580, 1950.

Joseph V Hajnal, David J Bryant, Larry Kasuboski, Pradip M Pattany, Beatrice De Coene, Paul D Lewis, Jacqueline M Pennock, Angela Oatridge, Ian R Young, and Graeme M Bydder. Use of fluid attenuated inversion recovery (FLAIR) pulse sequences in MRI of the brain. *Journal of computer assisted tomography*, 16(6):841–844, 1992.

Joseph V Hajnal, Ralph Myers, Angela Oatridge, Jane E Schwieso, Ian R Young, and Graeme M Bydder. Artifacts due to stimulus correlated motion in functional imaging of the brain. *Magnetic resonance in medicine*, 31(3):283–291, 1994.

S Halligan, JC Healy, and CI Bartram. Magnetic resonance imaging of fistula-in-ano: STIR or SPIR? *The British journal of radiology*, 71(842):141–145, 1998.

TTA Hayat, A Nihat, M Martinez-Biarge, A McGuinness, JM Allsop, JV Hajnal, and MA Rutherford. Optimization and initial experience of a multisection balanced steady-state free precession cine sequence for the assessment of fetal behavior in utero. *American Journal of Neuroradiology*, 32(2):331–338, 2011.

Jie Huo, Esra Turk, Tobias Hahn, et al. Human placental and fetal response to maternal hyperoxygenation in IUGR pregnancy as measured by BOLD MRI. In *Proc ISMRM*, 2015.

Bonnie J Huppert, Kathy R Brandt, Kirk D Ramin, and Bernard F King. Single-Shot Fast Spin-Echo MR Imaging of the Fetus: A Pictorial Essay 1. *Radiographics*, 19(suppl_1):S215–S227, 1999.

J Hykin, R Moore, K Duncan, S Clare, P Baker, I Johnson, R Bowtell, P Mansfield, and P Gowland. Fetal brain activity demonstrated by functional magnetic resonance imaging. *the Lancet*, 354(9179):645–646, 1999.

Aapo Hyvarinen. Fast and robust fixed-point algorithms for independent component analysis. *Neural Networks, IEEE Transactions on*, 10(3):626–634, 1999.

Aapo Hyvärinen, Juha Karhunen, and Erkki Oja. *Independent component analysis*, volume 46. John Wiley & Sons, 2004.

David H Ingvar. Patterns of brain activity revealed by measurements of regional cerebral blood flow. *Brain work*, 408:397–422, 1975.

David H Ingvar. "Hyperfrontal" distribution of the cerebral grey matter flow in resting wakefulness; on the functional anatomy of the conscious state. *Acta Neurologica Scandinavica*, 60(1):12–25, 1979.

David H Ingvar. "Memory of the future": an essay on the temporal organization of conscious awareness. *Human neurobiology*, 4(3):127–136, 1984.

András Jakab, Ernst Schwartz, Gregor Kasprian, Gerlinde M Gruber, Daniela Prayer, Veronika Schöpf, and Georg Langs. Fetal functional imaging portrays heterogeneous development of emerging human brain networks. *Frontiers in human neuroscience*, 8:1–17, 2014.

Renaud Jardri, Delphine Pins, Véronique Houfflin-Debarge, Caroline Chaffiotte, Nathalie Rocourt, Jean-Pierre Pruvo, Marc Steinling, Pierre Delion, and Pierre Thomas. Fetal cortical activation to sound at 33 weeks of gestation: a functional MRI study. *Neuroimage*, 42(1):10–18, 2008.

Peter Jezzard and Robert S Balaban. Correction for geometric distortion in echo planar images from B0 field variations. *Magnetic resonance in medicine*, 34(1): 65–73, 1995.

Peter Jezzard, Paul M Matthews, Stephen M Smith, et al. *Functional MRI: an introduction to methods*, volume 61. Oxford University Press Oxford, 2001.

Shuzhou Jiang, Hui Xue, Alan Glover, Mary Rutherford, Daniel Rueckert, and Joseph V Hajnal. MRI of moving subjects using multislice snapshot images with volume reconstruction (SVR): application to fetal, neonatal, and adult brain studies. *IEEE Transactions on Medical Imaging*, 26(7):967–980, 2007.

Ian Jolliffe. *Principal component analysis*. Wiley Online Library, 2002.

Jaber Juntu, Jan Sijbers, Dirk Van Dyck, and Jan Gielen. Bias field correction for mri images. In *Computer Recognition Systems*, volume 30, pages 543–551. Springer, 2005.

Boklye Kim, Jennifer L Boes, Peyton H Bland, Thomas L Chenevert, and Charles R Meyer. Motion correction in fMRI via registration of individual slices into an anatomical volume. *Magnetic resonance in medicine*, 41(5):964–972, 1999.

Kio Kim, Piotr A Habas, Francois Rousseau, Orit A Glenn, A James Barkovich, and Colin Studholme. Intersection based motion correction of multislice MRI for 3-D in utero fetal brain image formation. *Medical Imaging, IEEE Transactions on*, 29(1):146–158, 2010.

Kio Kim, Piotr A Habas, Vidya Rajagopalan, Julia A Scott, James M Corbett-Detig, Francois Rousseau, A James Barkovich, Orit A Glenn, and Colin Studholme. Bias field inconsistency correction of motion-scattered multislice MRI for improved 3D image reconstruction. *Medical Imaging, IEEE Transactions on*, 30(9):1704–1712, 2011.

Kevin M Koch, Douglas L Rothman, and Robin A de Graaf. Optimization of static magnetic field homogeneity in the human and animal brain in vivo. *Progress in nuclear magnetic resonance spectroscopy*, 54(2):69–96, 2009.

Maria Kuklisova-Murgasova, Gerardine Quaghebeur, Mary A Rutherford, Joseph V Hajnal, and Julia A Schnabel. Reconstruction of fetal brain MRI with intensity matching and complete outlier removal. *Medical image analysis*, 16(8):1550–1564, 2012.

Maria Kuklisova-Murgasova, Amalia Cifor, Raffaele Napolitano, Aris Papageorghiou, Gerardine Quaghebeur, Mary A Rutherford, Joseph V Hajnal, J Alison Noble, and Julia A Schnabel. Registration of 3D fetal neurosonography and MRI. *Medical Image Analysis*, 17(8):1137–1150, 2013.

Kenneth K Kwong, John W Belliveau, David A Chesler, Inna E Goldberg, Robert M Weisskoff, Brigitte P Poncelet, David N Kennedy, Bernice E Hoppel, Mark S Cohen, and Robert Turner. Dynamic magnetic resonance imaging of human brain activity during primary sensory stimulation. *Proceedings of the National Academy of Sciences*, 89(12):5675–5679, 1992.

David J Larkman, Joseph V Hajnal, Amy H Herlihy, Glyn A Coutts, Ian R Young, and Gösta Ehnholm. Use of multicoil arrays for separation of signal from multiple slices simultaneously excited. *Journal of Magnetic Resonance Imaging*, 13(2):313–317, 2001.

Seungyong Lee, George Wolberg, and Sung Yong Shin. Scattered data interpolation with multilevel B-splines. *Visualization and Computer Graphics, IEEE Transactions on*, 3(3):228–244, 1997.

Rui Liao, Jeffrey L Krolik, and Martin J McKeown. An information-theoretic criterion for intrasubject alignment of FMRI time series: motion corrected independent component analysis. *Medical Imaging, IEEE Transactions on*, 24 (1):29–44, 2005.

Richard S Likes. Moving gradient zeugmatography, December 22 1981. US Patent 4,307,343.

Guoying Liu, Geoffrey Sobering, Jeff Duyn, and Chrit TW Moonen. A. functional mri technique combining principles of echo-shifting with a train of observations (PRESTO). *Magnetic resonance in medicine*, 30(6):764–768, 1993.

Julian Maclaren, Michael Herbst, Oliver Speck, and Maxim Zaitsev. Prospective motion correction in brain imaging: a review. *Magnetic Resonance in Medicine*, 69(3):621–636, 2013.

PJ Magistretti and L Pellerin. The contribution of astrocytes to the 18F-2-deoxyglucose signal in PET activation studies. *Molecular psychiatry*, 1(6): 445–452, 1996.

C Malamateniou, SJ Malik, SJ Counsell, JM Allsop, AK McGuinness, T Hayat, K Broadhouse, RG Nunes, AM Ederies, JV Hajnal, et al. Motion-compensation techniques in neonatal and fetal MR imaging. *American Journal of Neuroradiology*, 34(6):1124–1136, 2013.

P Mansfield. Real-time echo-planar imaging by NMR. *British medical bulletin*, 40(2):187–190, 1984.

Peter Mansfield. Multi-planar image formation using NMR spin echoes. *Journal of Physics C: Solid State Physics*, 10(3):L55, 1977.

Jintong Mao, Hong Yan, WW Brey, WD Bidgood, JJ Steinbach, and A Mancuso. Fat tissue and fat suppression. *Magnetic resonance imaging*, 11(3):385–393, 1993.

Paul M Margosian, Gordon DeMeester, and Haiying Liu. Partial fourier acquisition in MRI. *eMagRes*, 2007.

Martin J McKeown, Yong-jie Hu, and Z Jane Wang. ICA denoising for event-related fMRI studies. In *Engineering in Medicine and Biology Society, 2005. IEEE-EMBS 2005.*, pages 157–161. IEEE, 2006.

Chrit TW Moonen, Guoying Liu, Peter Van Gelderen, and Geoffrey Sobering. A fast gradient-recalled MRI technique with increased sensitivity to dynamic susceptibility effects. *Magnetic resonance in medicine*, 26(1):184–189, 1992.

Chrit TW Moonen, Fernando A Barrios, Jeffrey R Zigun, Joe Gillen, Guoying Liu, Geoffrey Sobering, Roy Sexton, John Woo, Joseph Frank, and Daniel R Weinberger. Functional brain MR imaging based on bolus tracking with a fast T 2-sensitized gradient-echo method. *Magnetic resonance imaging*, 12(3): 379–385, 1994.

RJ Moore, S Vadeyar, J Fulford, DJ Tyler, C Gribben, PN Baker, D James, and PA Gowland. Antenatal determination of fetal brain activity in response to an

acoustic stimulus using functional magnetic resonance imaging. *Human brain mapping*, 12(2):94–99, 2001.

Kay Nehrke, Peter Börnert, Jan Groen, Jouke Smink, and Johannes C Böck. On the performance and accuracy of 2D navigator pulses. *Magnetic resonance imaging*, 17(8):1173–1181, 1999.

Seiji Ogawa, TM Lee, AR Kay, and DW Tank. Brain magnetic resonance imaging with contrast dependent on blood oxygenation. *Proceedings of the National Academy of Sciences*, 87(24):9868–9872, 1990.

Seiji Ogawa, David W Tank, Ravi Menon, Jutta M Ellermann, Seong G Kim, Helmut Merkle, and Kamil Ugurbil. Intrinsic signal changes accompanying sensory stimulation: functional brain mapping with magnetic resonance imaging. *Proceedings of the National Academy of Sciences*, 89(13):5951–5955, 1992.

Linus Pauling and Charles D Coryell. The magnetic properties and structure of hemoglobin, oxyhemoglobin and carbonmonoxyhemoglobin. *Proceedings of the National Academy of Sciences of the United States of America*, 22(4):210, 1936.

John Pauly, Dwight Nishimura, and Albert Macovski. A k-space analysis of small-tip-angle excitation. *Journal of Magnetic Resonance*, 213(2):544–557, 2011.

Jonathan E Peelle, Rowena J Eason, Sebastian Schmitter, Christian Schwarzbauer, and Matthew H Davis. Evaluating an acoustically quiet EPI sequence for use in fMRI studies of speech and auditory processing. *Neuroimage*, 52(4):1410–1419, 2010.

Alexander Poellinger, Robert Thomas, Peter Lio, Anne Lee, Nikos Makris, Bruce R Rosen, and Kenneth K Kwong. Activation and habituation in olfaction—an fMRI study. *Neuroimage*, 13(4):547–560, 2001.

Jonathan D Power, Kelly A Barnes, Abraham Z Snyder, Bradley L Schlaggar, and Steven E Petersen. Spurious but systematic correlations in functional

connectivity MRI networks arise from subject motion. *Neuroimage*, 59(3): 2142–2154, 2012.

Daniela Prayer, Gregor Kasprian, Elisabeth Krampl, Barbara Ulm, Linde Witzani, Lucas Prayer, and Peter C Brugger. MRI of normal fetal brain development. *European journal of radiology*, 57(2):199–216, 2006.

Klaas P Pruessmann, Markus Weiger, Markus B Scheidegger, Peter Boesiger, et al. SENSE: sensitivity encoding for fast MRI. *Magnetic resonance in medicine*, 42(5):952–962, 1999.

Cecile Rabrait, Philippe Ciuciu, Alejandro Ribes, Cyril Poupon, Patrick Le Roux, Ghislaine Dehaine-Lambertz, D Le Bihan, and F Lethimonnier. High temporal resolution functional MRI using parallel echo volumar imaging. *Journal of Magnetic Resonance Imaging*, 27(4):744–753, 2008.

Michael J Reeves, Marian Brandreth, Elspeth H Whitby, Anthony R Hart, Martyn NJ Paley, Paul D Griffiths, and John C Stevens. Neonatal Cochlear Function: Measurement after Exposure to Acoustic Noise during in Utero MR Imaging. *Radiology*, 257(3):802–809, 2010.

Douglas S Richards, Barbare Frentzen, Kenneth J Gerhardt, Mary E McCann, and Robert M Abrams. Sound levels in the human uterus. *Obstetrics & Gynecology*, 80(2):186–190, 1992.

MJ Rivkin, D Wolraich, H Als, G McAnulty, S Butler, N Conneman, C Fischer, S Vajapeyam, RL Robertson, and RV Mulkern. Prolonged T2* values in newborn versus adult brain: implications for fMRI studies of newborns. *Magnetic resonance in medicine*, 51(6):1287–1291, 2004.

Matthew D Robson, Jennifer L Dorosz, and John C Gore. Measurements of the temporal fMRI response of the human auditory cortex to trains of tones. *Neuroimage*, 7(3):185–198, 1998.

Francois Rousseau, Orit A Glenn, Bistra Iordanova, Claudia Rodriguez-Carranza, Daniel B Vigneron, James A Barkovich, and Colin Studholme. Registration-based approach for reconstruction of high-resolution in utero fetal MR brain images. *Academic radiology*, 13(9):1072–1081, 2006.

Erika Schneider and Gary Glover. Rapid in vivo proton shimming. *Magnetic Resonance in Medicine*, 18(2):335–347, 1991.

V Schöpf, G Kasprian, PC Brugger, and D Prayer. Watching the fetal brain at "rest". *International Journal of Developmental Neuroscience*, 30(1):11–17, 2012.

A Serag, V Kyriakopoulou, M A Rutherford, A D Edwards, and J V Hajnal. A multi-channel 4D probabilistic atlas of the developing brain: Application to fetuses and neonates. *Annals of the BMVA*, 2012(3):1–14, 2012.

Sharmishtaa Seshamani, Mads Fogtmann, Xiaoyin Cheng, M Thomason, Chris Gatenby, and Colin Studholme. Cascaded slice to volume registration for moving fetal FMRI. In *Biomedical Imaging (ISBI), 2013 IEEE 10th International Symposium on*, pages 796–799. IEEE, 2013.

Sharmishtaa Seshamani, Xi Cheng, Mads Fogtmann, Moriah E Thomason, and Colin Studholme. A method for handling intensity inhomogenieties in fMRI sequences of moving anatomy of the early developing brain. *Medical image analysis*, 18(2):285–300, 2014.

Sharmishtaa Seshamani, Anna I Blazejewska, Christopher Gatenby, Susan Mckown, Jason Caucutt, Manjiri Dighe, and Colin Studholme. Comparing consistency of R2* and T2*-weighted BOLD analysis of resting state fetal fMRI. In *SPIE Medical Imaging*, pages 94170N–94170N. International Society for Optics and Photonics, 2015.

Donald Shepard. A two-dimensional interpolation function for irregularly-spaced data. In *Proceedings of the 1968 23rd ACM national conference*, pages 517–524. ACM, 1968.

Nicola R Sibson, Ajay Dhankhar, Graeme F Mason, Douglas L Rothman, Kevin L Behar, and Robert G Shulman. Stoichiometric coupling of brain glucose metabolism and glutamatergic neuronal activity. *Proceedings of the National Academy of Sciences*, 95(1):316–321, 1998.

JC Siero, VO Boer, JM Hoogduin, PR Luijten, and DW Klomp. Cost function guided 3rd order B0 shimming for MR spectroscopic imaging at 7T. In *Proceedings of International Society for Magnetic Resonance in Medicine*, volume 17, page 132, 2009.

John G Sled, Alex P Zijdenbos, and Alan C Evans. A nonparametric method for automatic correction of intensity nonuniformity in MRI data. *Medical Imaging, IEEE Transactions on*, 17(1):87–97, 1998.

Stephen M Smith, Mark Jenkinson, Mark W Woolrich, Christian F Beckmann, Timothy EJ Behrens, Heidi Johansen-Berg, Peter R Bannister, Marilena De Luca, Ivana Drobnjak, David E Flitney, et al. Advances in functional and structural MR image analysis and implementation as FSL. *Neuroimage*, 23:S208–S219, 2004.

Christopher D Smyser, Terrie E Inder, Joshua S Shimony, Jason E Hill, Andrew J Degnan, Abraham Z Snyder, and Jeffrey J Neil. Longitudinal analysis of neural network development in preterm infants. *Cerebral Cortex*, 20(12):2852–2862, 2010.

Allen W Song, Eric C Wong, and James S Hyde. Echo-volume imaging. *Magnetic resonance in medicine*, 32(5):668–671, 1994.

Greg J Stanisz, Ewa E Odrobina, Joseph Pun, Michael Escaravage, Simon J Graham, Michael J Bronskill, and R Mark Henkelman. T1, T2 relaxation and magnetization transfer in tissue at 3T. *Magnetic Resonance in Medicine*, 54 (3):507–512, 2005.

Martin Styner, Christian Brechbuhler, G Szckely, and Guido Gerig. Parametric estimate of intensity inhomogeneities applied to MRI. *Medical Imaging, IEEE Transactions on*, 19(3):153–165, 2000.

Moriah E Thomason, Maya T Dassanayake, Stephen Shen, Yashwanth Katkuri, Mitchell Alexis, Amy L Anderson, Lami Yeo, Swati Mody, Edgar Hernandez-Andrade, Sonia S Hassan, et al. Cross-hemispheric functional connectivity in the human fetal brain. *Science translational medicine*, 5(173):1–10, 2013.

C Triantafyllou, RD Hoge, G Krueger, CJ Wiggins, A Potthast, GC Wiggins, and LL Wald. Comparison of physiological noise at 1.5 T, 3 T and 7 T and optimization of fMRI acquisition parameters. *Neuroimage*, 26(1):243–250, 2005.

Martijn P Van Den Heuvel and Hilleke E Hulshoff Pol. Exploring the brain network: a review on resting-state fMRI functional connectivity. *European Neuropsychopharmacology*, 20(8):519–534, 2010.

Martijn P Van Den Heuvel and Hilleke E Hulshoff Pol. Exploring the brain network: a review on resting-state fMRI functional connectivity. *European Neuropsychopharmacology*, 20(8):519–534, 2010.

W van der Zwaag, T Kober, JP Marques, G Glover, R Gruetter, and G Krueger. Comparison of single-shot 2D EPI and segmented 3D EVI acquisition for fMRI at 7T. In *Proc ISMRM*, page 1550, 2009.

Wietske Van der Zwaag, Susan Francis, and Richard Bowtell. Improved echo volumar imaging (EVI) for functional MRI. *Magnetic resonance in medicine*, 56(6):1320–1327, 2006.

Serge Vasylechko, Christina Malamateniou, Rita G Nunes, Matthew Fox, Joanna Allsop, Mary Rutherford, Daniel Rueckert, and Joseph V Hajnal. T2* relaxometry of fetal brain at 1.5 Tesla using a motion tolerant method. *Magnetic Resonance in Medicine*, 2014.

Uros Vovk, Franjo Pernus, and Bostjan Likar. A review of methods for correction of intensity inhomogeneity in MRI. *Medical Imaging, IEEE Transactions on*, 26(3):405–421, 2007.

Williams M Wells III, W Eric L Grimson, Ron Kikinis, and Ferenc A Jolesz. Adaptive segmentation of MRI data. *IEEE Transactions on Medical Imaging*, 15(4):429–442, 1996.

Lori-Anne Williams, Neil Gelman, Paul A Picot, David S Lee, James R Ewing, Victor K Han, and R Terry Thompson. Neonatal brain: Regional variability of in vivo MR imaging relaxation rates at 3.0 T - initial experience. *Radiology*, 235(2):595–603, 2005.

James L Wilson, Mark Jenkinson, and Peter Jezzard. Optimization of static field homogeneity in human brain using diamagnetic passive shims. *Magnetic resonance in medicine*, 48(5):906–914, 2002.

Suzanne T Witt, Angela R Laird, and M Elizabeth Meyerand. Functional neuroimaging correlates of finger-tapping task variations: an ALE meta-analysis. *Neuroimage*, 42(1):343–356, 2008.

Sadie E Yancey, David J Rotenberg, Fred Tam, Mark Chiew, Shawn Ranieri, L Biswas, Kevan JT Anderson, S Nicole Baker, Graham A Wright, and Simon J Graham. Spin-history artifact during functional MRI: Potential for adaptive correction. *Medical physics*, 38(8):4634–4646, 2011.

Yihong Yang, Venkata S Mattay, Daniel R Weinberger, Joseph A Frank, and Jeff H Duyn. Localized echo-volume imaging methods for functional MRI. *Journal of Magnetic Resonance Imaging*, 7(2):371–375, 1997.